

1 Dear Editor,  
2 Here you will find the document including a point-by-point response to the reviewers, with a list of all  
3 relevant changes (in red in the text) made in the manuscript, and a marked-up manuscript version.  
4 With my best regards,  
5 Dr. M. Mallet

6  
7 -----

8  
9 Journal: ACP  
10 Title: Overview of the Chemistry-Aerosol Mediterranean Experiment/Aerosol Direct Radiative Forcing on the  
11 Mediterranean Climate (ChArMEx/ADRIMED) summer 2013 campaign.  
12 Author(s): M. Mallet et al.  
13 MS No.: acp-2015-454  
14 MS Type: Research article  
15 Iteration: Revised Submission  
16 Special Issue: CHemistry and AeRosols Mediterranean EXperiments (ChArMEx)  
17 (ACP/AMT Inter-Journal SI)

18  
19 Anonymous Referee #3

20  
21 The article gives an overview of an extensive field campaign including ground based in-situ and remote  
22 sensing measurements as well as airborne observations. The described ChArMEx/ADRIMED campaign  
23 incorporates existing ground based stations and adds valuable additional measurements at several super  
24 sites and secondary sites. Furthermore even satellite observations are considered and several different  
25 models are compared using the vast amount of observations. I agree with the reviewer 1 & 2 the paper is  
26 not strong in presenting new scientific findings. Nevertheless, this article paves the way for further  
27 investigations on the same data set and sets a basis for future publications. The aims of the campaign are  
28 clearly outlined in the introduction and all observations are well presented. Additionally, some results are  
29 summarized and emphasized in the Conclusions with the hint to future publications. To my understanding  
30 proving existing knowledge, like the reasonable agreement of observed and modelled AOD and the negative  
31 radioactive forcing (found by others before) is often neglected in literature, but it is an important finding.  
32 Especially the changes and answers followed by questions of reviewer 2 & 1 improve the quality of the  
33 paper a lot. I would like to emphasise the importance of such an overview paper of a big campaign and  
34 recommend the paper to be published after including a few more changes:

35  
36 ***We would like to thank the reviewer for these remarks and comments on the article.***

37  
38 Major comments:

39  
40 Page 19671 Conclusion:

41 In your introduction you have outlined the aims of the campaign very well. But from the conclusion only the  
42 first two aspects are addressed. The first aspect is obviously fulfilled. For the second Page 19672 line 20 and  
43 line 23: Remind the reader on previous published values and compare briefly. How does this improve the  
44 understanding of the Mediterranean DRF? And the third aspect is almost left out. In fact could you  
45 summarize how the modifications of the radiative budget due to aerosols affect the sea-surface evaporation  
46 fluxes, relative humidity profiles, cloud-cover, and precipitation ? And more largely the Mediterranean  
47 hydrological cycle. Or at least try to incorporate some of these aspects.

48  
49 ***Compared to the first version of the article, a lot of modifications have been already included in the  
50 conclusion (following the previous remarks of reviewers 1 and 2) especially to underline the main results  
51 and originality of this project. Such modifications include the aspects mentioned by the reviewer. In that  
52 sense, we have integrated and discussed AOD, size distribution and optical properties observations in a  
53 more larger context; as the comparisons with studies referenced over dust source regions (during the  
54 FENNEC, SAMUM1 and AMMA projects) as well as measurements obtained in the Atlantic Ocean at Cape-***

55 **Verde region (SAMUM-2) and at Puerto-Rico (PRIDE).**

56  
57 **Following the reviewer remark, we have now also included a sentence indicating that this new direct**  
58 **radiative forcing (DRF) estimates deduced from this projet is consistent with the values previously**  
59 **referenced over the Mediterranean region and listed in the introduction. The third aspect that concerns**  
60 **the modifications of the sea-surface evaporation fluxes, relative humidity and precipitation is now**  
61 **included in the conclusion, based on an Ocean-Atmosphere regional model simulation. The new**  
62 **paragraph in the conclusion is the following:**

63 **“A first simulation (conducted for the 2003 to 2009 period) that takes into account the ocean-atmosphere**  
64 **coupling has demonstrated that the significant aerosol radiative forcing is responsible for a decrease in**  
65 **sea surface temperature (on average -0.5 °C for the Mediterranean). In addition, the latent heat loss is**  
66 **shown to be weaker in the presence of aerosols, resulting in a decrease in specific humidity in the lower**  
67 **troposphere, and a reduction in cloud cover and precipitation.”**

68  
69 Figure 1, 5, 6: Could you show the average of AERONET stations over the same time period ? I noticed some  
70 stations already exist since at least 2003. It would be a useful addition to mention in text as well, if at all  
71 possible. Similar for Figure 28: How does the satellite compare? Of course it is averaged over a bigger area,  
72 but would be still interesting, e.g. to exclude/identify local effects. You could also suggest/outlook for future  
73 investigations.

74 **This in an interesting remark and AOD values derived from AERONET database have been now added in**  
75 **the new figures 1, 5 and 6 for different AERONET stations. A sentence has been also added in the**  
76 **corresponding captions. In addition, the MODIS AOD values have been included in the Figure 31 (figure 28**  
77 **of the first version of the article) for comparisons with the different models (RCSM, RegCM, CHIMERE and**  
78 **COSMO-MUSCAT) and AERONET/PHOTONS data at two (Ersa and Lampedusa) AERONET surface stations.**

79  
80 Minor comments:

81  
82 Page 19627 line 6: Give a short introduction reminder on how many sites, e.g., During the campaign XX  
83 super sites and XX secondary sites were set up, which are decribed in the following.'

84 **This point is now added in the text in the part 2.**

85  
86 Page 19634 line 8: Are they really deployed just fort the campaign? Or did you use existing AERONET sites  
87 (checking on the AERONET page, it looks like many of the stations have been there longer). Please revise. As  
88 well give a brief summary, how many sites you have used, just a short sentence is enough.

89 **This is effectively right and we have now detailed this point to distinguish the AERONET stations which**  
90 **have been specifically deployed for the ChArMeX/ADRIMED campaign with those already existing over**  
91 **the Mediterranean basin. In that sense, we have added this sentence in the new version: “Sun-**  
92 **photometer stations used during the SOP-1a campaign over the Western basin are listed in the Table 2.**  
93 **The new instruments, deployed specifically during the ChArMEx/ADRIMED project, are the Ersa, Cap d’En**  
94 **Font, Cagliari and Majorque stations.”.**

95  
96 Page19646 line 27: The order of words in the sentence is somewhat confusing, please revise.

97 **This is now changed in the new version.**

98  
99 Page 19653 line 15: ,almost scattering' seems not to be the right term, maybe none absorbing of mainly  
100 scattering ?

101 **This is effectively true and now modify in the text.**

102  
103 Page 19656 line 24: be consistent with the figure: Angström Exponent (AE)

104 **This is now corrected.**

105  
106 Page 19663 line 8: be consistent Table capital (check document). Article, the' not needed.

107 **This is now changed in the new version.**

109 Page 19667 line 21: ...the ..model...simulates (s is missing)  
110 ***This is now corrected.***  
111  
112 Page 19668 line 16: The order of words in the sentence is not correct, please revise.  
113 ***This is now done in the new version.***  
114  
115 Table 1 caption: ....gas concentrations.....  
116 ***This is now changed.***  
117  
118 Table 2: It would be helpful to add information about the photometer type used, e.g. how many wavelength  
119 filters, with or without polar filter.  
120 ***The number of wavelengths is now added in Table 2 in a new column. The information on the polarization***  
121 ***for each instrument is not always available.***  
122  
123 Table4: ...sounding balloon (no ,s') flights...  
124 ***This is now done.***  
125  
126 Table 6: ....in the Table (be consistent, with capital T)  
127 ***This is now modified.***  
128  
129 Table 7: It is not clear to me, why you only choose 4 stations. State a reason or show all stations. (Actually I  
130 think this table is removed in the new version, since shown in the figure)  
131 ***This Table is effectively removed in the new version and we have now introduced more explanations on***  
132 ***the choice of the 4 AERONET/PHOTONS stations in the text. This choice has been motivated by the fact***  
133 ***that these sites correspond to (i) three of the different surface stations (Ersa, Lampedusa and Cap d'En***  
134 ***Font) affected by different aerosol regimes and (ii) the two aircrafts locations (Cagliari). This point is now***  
135 ***indicated in the text in the part 5.2.2.***  
136  
137 Figure 2: The two aircrafts....  
138 ***This is now modified in the new version.***  
139  
140 Figure 3: I think it should be ....flight trajectories...  
141 ***This is now changed in the new version.***  
142  
143  
144  
145  
146  
147  
148  
149  
150  
151  
152  
153  
154  
155  
156  
157  
158  
159  
160

161 Review of the revised paper to ACP “Overview of the Chemistry-Aerosol Mediterranean  
162 Experiment/Aerosol Direct Radiative Forcing on the Mediterranean Climate (ChArMEx/ADRMED)  
163 summer 2013 campaign” by Mallet et al.

164

165 In general, I am happy with the author’s replies to my comments. However, there are some  
166 technical points that need further attention. Thus, I suggest the publication of the paper in ACP.  
167 Below there are my comments to some of the authors’ replies.

168

169 ***Again, we would like to thank the reviewer 2 for the different interesting remarks and comments on the***  
170 ***article.***

171

172 Referee#2

173

174 Minor comments

175

176 4. Page 19626, Line 2: “... an innovative database ...” I agree that the database is rich, but what is  
177 the innovation about it?

178 Referee’s reply: The author’s reply is fine just they should replace the word “huge” in the sentence  
179 ‘... for creating a huge 3-D database of physical ...’ by something more moderate, e.g. rich,  
180 important. I do not think that we should stop taking aerosol observations in the Mediterranean  
181 after ADRIMED.

182 ***We agree with this. Indeed, this project provides new insights on aerosol properties, radiative***  
183 ***effects and climate impact but a lot of aspects have not been documented. We have now***  
184 ***replaced the word “huge” by the term “rich” as proposed, in the last version.***

185

186 7. Page 19634, Lines 11-25: What’s the point of the EARLINET/ACTRIS network section as the 4  
187 stations operated only for 1-2 days during the campaign and none of their data is presented in the  
188 manuscript. I suggest either to eliminate or to reduce significantly.

189 If the reviewer agrees, we prefer keeping this part in the article as a study is ongoing to compare  
190 aircraft observations with lidar retrievals. However, we agree that the part was too long and in that  
191 sense, we have now reduced it in the new version.

192 Referee’s reply: I was very astonished to realize that the authors have not reduced almost at all the  
193 text in the new version. To my view they can do better than that.

194 ***Effectively, we tried to reduce as most as possible this small paragraph by keeping the most***  
195 ***important information’s. We agree we can do more and we have now again reduced this part in***  
196 ***the new version.***

197

198 9. Page 19639, Line 26: Add references for the satellite retrievals.

199 All the references; Tanré et al. (1997), Tanré et al. (2011), Khan et al. (2010) and Thieleux et al.  
200 (2005) have now been cited for the MODIS, PARASOL, MISR and SEVIRI sensors, respectively.

201 Referee’s reply: Replace “Khan” by “Kahn” in the text.

202 ***Thank you for this remark; this is now changed in the text.***

203

204 21. Page 19652, Lines 8-10: The following AERONET stations Oujda, Cagliari, Cap d’En  
205 Font,Ouarzazate, Frioul and Majorque while appear in Figs. 18 and 25, there are missing from  
206 Tab.2.

207 This is effectively true and we have now completed the Table 2.

208 Referee’s reply: Replace “Oujda” by “Ouijda” in Table 2.

209 ***This is now done in the new version.***

210 23. Page 19656, Lines 15-18: Certainly the wavelength dependence is lower than below the 2 km,  
211 but it is not very small, as someone can see just above and below the peak at about 3 km. Why this  
212 happens?

213 The reviewer correctly remarks that there is a relatively large variability in the backscattering  
214 coefficient wavelength dependence at the altitudes where desert dust is expected. This is apparent  
215 in figure 22 b), with layers characterized by high values of backscattering coefficient displaying a  
216 small wavelength dependence, and intermediate layers with a moderate dependence. This  
217 suggests a variability in the aerosol size distribution and/or refractive index/shape. We do not have  
218 additional information that allows us to interpret this variability. In any case, all the particles below  
219 approximately 2 km display a significantly larger wavelength dependence, suggesting markedly  
220 different optical properties. A similar vertical variability of the wavelength dependence is  
221 observed, for instance, in figure 20 for the scattering coefficient profile measured over Lampedusa  
222 on 22 June; as discussed in section 5.2.3, particles of different origin and optical properties may be  
223 identified at the various altitudes.

224 Referee's reply: Delete the word "very" from the sentence '...above 2 km shows very small  
225 wavelength dependence, ...'. This is in line with your reply.

226 ***This is now changed in the new version.***

227

228 24. Page 19657, Lines 6-8: Is the LNG cross section in Fig. 23 correct? It seems from the text and  
229 the AOD figure below that the latitude axis is inverted.

230 There was effectively a mistake and the Figure 23 corresponds to the flight from Sardinia to the  
231 Gulf of Genoa. This is now changed in the text.

232 Referee's reply: As I wrote the inconsistency is not only between the figure and the text, but also  
233 between the LNG cross section and the optical depth figure. For example looking at the LNG cross  
234 section at 41oN the extinction coefficient is  $\sim 0.015 \text{ km}^{-1} \times 6 \text{ km} = 0.09$ , while at 44oN the  
235 extinction coefficient seems to be  $\sim 0.06 \text{ km}^{-1} \times 6 \text{ km} = 0.36$ . While from the optical depth figure  
236 below at these latitudes, the values are  $\sim 0.45$  and  $\sim 0.1$  at 41oN and 44oN, respectively. Thus,  
237 either in the LNG cross section or in the optical depth figure, the latitude axis is inverted.

238 ***Thank you for this remark. This is effectively a mistake and the latitude was inverted in the upper***  
239 ***figure. We have now modified it in the new version. The two figures are now consistent.***

240

241 29. Homogenize the boundaries of the maps in Figs. 1, 5, 6, 7, 9, 10, 11, 12, 27 and 29. The same  
242 for Figs. 2, 3 and 4.

243 This is unfortunately quite difficult to homogenize all the figures as they have been prepared by  
244 using different products (models, satellites) with different horizontal resolutions and domains (for  
245 instance TRMM is limited to 50°N). For every figure, we have tried to represent as most as possible  
246 a similar domain, integrating the entire Mediterranean basin. If this is acceptable, we propose to  
247 keep the different figures in the present configuration.

248 Referee's reply: I do not consider this answer as valid, for example how many times in the paper  
249 there is reference to latitudes above 50oN? However, as this comment is not related to the  
250 scientific quality of the paper, if the authors feel happy with their figures, they can keep them as  
251 they are.

252 ***If this is acceptable, we propose to keep the different figures in the present form as they provide***  
253 ***the most important information's related to the text.***

254

255 Technical comments

256 1. Page 19621, Line 20: Crete is a Greek island, please modify accordingly.

257 This is now modified in the introduction.

258 Referee's reply: Change the 'the Crete Greece island' to the 'Greek island of Crete'.

259 ***This is now made in the new version.***

260

261 5. Page 19624, Line 15, Page 19661, Line 6: Nabat et al. (2015), which of the three ?

262 This is now indicated: Nabat et al. (2015a).

263 Referee's reply: Not in the first occurrence.

264 ***The reference is now corrected.***

265

266 Additional comments

267

268 Please find below some additional comments related to revised version. The numbers are for the  
269 revised paper.

270

271 1) Check the number of Figures and Tables when they are cited in the text, as after the  
272 introduction of new figures/tables not all of them are referring to the respective figure/table.

273 ***We have checked that the numbers of Figures and Tables are now good in the new version.***

274

275 2) Lines 929 (Abstract) and 2342 (Conclusions): Delete the word "climatic", as this is referred to  
276 only 7 years (2003-2009).

277 ***We have now removed this term in the abstract and conclusion in the new version.***

278

279 3) Line 2049: Delete "s" from 'estimates'.

280 ***This is now done.***

281

282 4) Line 2064: In the specify D in the text?

283 ***This is effectively right and we have now included the calculations of D in the text.***

284

285

286

287

288

289

290

291

292

293

294

295

296

297

298

299

300

301

302

303

304

305

306 Overview of the Chemistry-Aerosol Mediterranean Experiment/Aerosol Direct Radiative  
307 Forcing on the Mediterranean Climate (ChArMEx/ADRI-MED) summer 2013 campaign.

308

309 *Mallet M.<sup>1</sup>, F. Dulac<sup>2</sup>, P. Formenti<sup>3</sup>, P. Nabat<sup>4</sup>, J. Sciare<sup>2,5</sup>, G. Roberts<sup>4</sup>, J. Pelon<sup>6</sup>, G. Ancellet<sup>6</sup>, D. Tanré<sup>7</sup>, F.*  
310 *Parol<sup>7</sup>, C. Denjean<sup>4</sup>, G. Brogniez<sup>7</sup>, A. di Sarra<sup>8</sup>, L. Alados<sup>9</sup>, J. Arndt<sup>10</sup>, F. Aurio<sup>7</sup>, L. Blarel<sup>7</sup>, T. Bourriane<sup>5</sup>, P.*  
311 *Chazette<sup>2</sup>, S. Chevaillier<sup>3</sup>, M. Claeys<sup>5</sup>, B. D'Anna<sup>11</sup>, Y. Derimian<sup>7</sup>, K. Desboeufs<sup>3</sup>, T. Di Iorio<sup>8</sup>, J.-F. Doussin<sup>3</sup>, P.*  
312 *Durand<sup>1</sup>, A. Féron<sup>3</sup>, E. Freney<sup>13</sup>, C. Gaimoz<sup>3</sup>, P. Goloub<sup>7</sup>, J. L. Gómez-Amo<sup>8</sup>, M. J. Granados-Muñoz<sup>9</sup>, N. Grand<sup>3</sup>,*  
313 *E. Hamonou<sup>2</sup>, I. Jankowiak<sup>7</sup>, M. Jeannot<sup>14</sup>, J.-F. Léon<sup>1</sup>, M. Maillé<sup>3</sup>, S. Mailler<sup>15</sup>, D. Meloni<sup>8</sup>, L. Menut<sup>15</sup>, G.*  
314 *Momboisse<sup>5</sup>, J. Nicolas<sup>11</sup>, T. Podvin<sup>7</sup>, V. Pont<sup>1</sup>, G. Rea<sup>15</sup>, J.-B. Renard<sup>14</sup>, L. Roblou<sup>1</sup>, K. Schepanski<sup>16</sup>, A.*  
315 *Schwarzenboeck<sup>13</sup>, K. Sellegri<sup>13</sup>, M. Sicard<sup>17</sup>, F. Solmon<sup>18</sup>, S. Somot<sup>5</sup>, B. Torres<sup>7</sup>, J. Totems<sup>1</sup>, S. Triquet<sup>3</sup>, N.*  
316 *Verdier<sup>19</sup>, C. Verwaerde<sup>7</sup>, J. Wenger<sup>10</sup> and P. Zapf<sup>3</sup>.*

317

318 1 Laboratoire d'Aérodynamique, Observatoire Midi-Pyrénées, 14 Avenue Edouard Belin, 31400 Toulouse, France

319 2 LSCE-CEA/IPSL, CEA Saclay 701, 91191 Gif-sur-Yvette, France

320 3 Laboratoire Inter-Universitaire des Systèmes Atmosphériques (LISA), UMR CNRS 7583, Université Paris Est  
321 Créteil et Université Paris Diderot, Institut Pierre Simon Laplace, Créteil, France

322 4 Météo-France, CNRM-GAME, Centre national de recherches météorologiques, UMR3589, Toulouse,  
323 France

324 5 The Cyprus Institute, Energy Environment and Water Research Center, Nicosia, Cyprus

325 6 LATMOS-ISPL, UPMC Univ. Paris 06; Université Versailles St-Quentin; CNRS/INSU, Paris, France

326 7 LOA, Université Lille 1, Villeneuve d'Ascq, France

327 8 ENEA, Laboratory for Earth Observations and Analyses, Via Anguillarese 301, 00123 Roma, Italy

328 9 Department of Applied Physics, University of Granada, 18071, Granada, Spain

329 10 Department of Chemistry and Environmental Research Institute, University College Cork, Ireland

330 11 Institute de recherches sur la catalyse et l'environnement de Lyon (IRCE Lyon), University of Lyon, 69100  
331 Villeurbanne, France

332 12 Leibniz Institute for Tropospheric Research (TROPOS), Permoserstraße 15, 04318, Leipzig, Germany

333 13 Laboratoire de Météorologie Physique CNRS UMR6016, Observatoire de Physique du Globe de Clermont-  
334 Ferrand, Université Blaise Pascal, 63171 Aubière, France

335 14 LPC2E-CNRS/Université d'Orléans, 3A avenue de la recherche scientifique, 45071 Orléans, France

336 15 LMD, IPSL, CNRS, Ecole Polytechnique, École Normale Supérieure, Université Paris 6, UMR8539 91128  
337 Palaiseau CEDEX, France

338 16 Leibniz Institute for Tropospheric - Research - Permoserstr. 15, 04318 Leipzig, Germany

339 17 RSLab/CTE-CRAE-IEEC, Universitat Politècnica de Catalunya, Barcelona, Spain

340 18 The Abdus Salam International Center for Theoretical Physics, Strada Costiera 11, 34100 Trieste, Italy

341 19 Centre National d'Études Spatiales (CNES), DCT/BL/NB, 18 avenue Edouard Belin, 31401 Toulouse CEDEX  
342 9, France

343

344

345

346

347

348

349

350

351

352

353

354

355

356

357

358

359 **Abstract**

360  
361 The Chemistry-Aerosol Mediterranean Experiment (ChArMEx; <http://charmex.lsce.ipsl.fr>) is a collaborative  
362 research program federating international activities to investigate Mediterranean regional chemistry-climate  
363 interactions. A special observing period (SOP-1a) including intensive airborne measurements was performed  
364 in the framework of the Aerosol Direct Radiative Forcing on the Mediterranean Climate (ADRIMED) project  
365 during the Mediterranean dry season over the western and central Mediterranean basins, with a focus on  
366 aerosol-radiation measurements and their modeling. The SOP-1a took place from 11 June to 05 July 2013.  
367 Airborne measurements were made by both the ATR-42 and F-20 French research aircraft operated from  
368 Sardinia (Italy) and instrumented for in situ and remote-sensing measurements, respectively, and by  
369 sounding and drifting balloons, launched in Minorca. The experimental set-up also involved several ground-  
370 based measurement sites on islands including two ground-based reference stations in Corsica and  
371 Lampedusa and secondary monitoring sites in Minorca and Sicily. Additional measurements including lidar  
372 profiling were also performed on alert during aircraft operations at EARLINET/ACTRIS stations at Granada  
373 and Barcelona in Spain, and in southern Italy. Remote sensing aerosol products from satellites (MSG/SEVIRI,  
374 MODIS) and from the AERONET/PHOTONS network were also used. Dedicated meso-scale and regional  
375 modelling experiments were performed in relation to this observational effort. We provide here an  
376 overview of the different surface and aircraft observations deployed during the ChArMEx/ADRIMED period  
377 and of associated modeling studies together with an analysis of the synoptic conditions that determined the  
378 aerosol emission and transport. Meteorological conditions observed during this campaign (moderate  
379 temperatures and southern flows) were not favorable to produce high level of atmospheric pollutants nor  
380 intense biomass burning events in the region. However, numerous mineral dust plumes were observed  
381 during the campaign with main sources located in Morocco, Algeria and Tunisia, leading to aerosol optical  
382 depth (AOD) values ranging between 0.2 to 0.6 (at 440 nm) over the western and central Mediterranean  
383 basins. One important point of this experiment concerns the direct observations of aerosol extinction on-  
384 board the ATR-42, using CAPS system, showing local maxima reaching up to  $150 \text{ Mm}^{-1}$  within the dust  
385 plume. Non negligible aerosol extinction (about  $50 \text{ Mm}^{-1}$ ) was also been observed within the Marine  
386 Boundary Layer (MBL). By combining the ATR-42 extinction coefficient observations with absorption and



387 scattering measurements, we performed a complete optical closure revealing excellent agreement with  
388 estimated optical properties. This additional information on extinction properties has allowed calculating  
389 the dust single scattering albedo (SSA) with a high level of confidence over the Western Mediterranean. Our  
390 results show a moderate variability from 0.90 to 1.00 (at 530 nm) for all flights studied that is contrary to  
391 the available literature on this optical parameter. Our results underline also a relatively low difference in SSA  
392 with values derived near dust sources. In parallel, active remote-sensing observations from the surface and  
393 onboard the F-20 aircraft suggest a complex vertical structure of particles and distinct aerosol layers with  
394 sea-spray and pollution located within the MBL, and mineral dust and/or aged north American smoke  
395 particles located above (up to 6-7 km in altitude). Aircraft and balloon-borne observations allow to  
396 investigate the vertical structure of aerosol size distribution showing particles characterized by large size  
397 ( $>10\ \mu\text{m}$  in diameter) within dust plumes. In most of cases, a coarse mode characterized by an effective  
398 diameter ranging between 5 and  $10\ \mu\text{m}$ , has been detected above the MBL. In terms of shortwave (SW)  
399 direct forcing, in-situ surface and aircraft observations have been merged and used as inputs in 1-D radiative  
400 transfer codes for calculating the direct radiative forcing (DRF). Results show significant surface SW  
401 instantaneous forcing (up to  $-90\ \text{W m}^{-2}$  at noon). Aircraft observations provide also original estimates of the  
402 vertical structure of SW and LW radiative heating revealing significant instantaneous values of about  $5^\circ\text{K}$  per  
403 day (in the solar spectrum (for a solar angle of  $30^\circ$ ) within the dust layer. Associated 3-D modeling studies  
404 from regional climate (RCM) and chemistry transport (CTM) models indicate a relatively good agreement for  
405 simulated AOD compared with observations from the AERONET/PHOTONS network and satellite data,  
406 especially for long-range dust transport. Calculations of the 3-D SW (clear-sky) surface DRF indicate an  
407 average of about  $-10$  to  $-20\ \text{W m}^{-2}$  (for the whole period) over the Mediterranean Sea together with maxima  
408 ( $-50\ \text{W m}^{-2}$ ) over northern Africa. The top of the atmosphere (TOA) DRF is shown to be highly variable within  
409 the domain, due to moderate absorbing properties of dust and changes in the surface albedo. Indeed, 3-D  
410 simulations indicate negative forcing over the Mediterranean Sea and Europe and positive forcing over  
411 northern Africa. Finally, a multi-year simulation, performed for the 2003 to 2009 period and including an  
412 ocean-atmosphere (O-A) coupling, underlines the impact of the aerosol direct radiative forcing on the sea  
413 surface temperature, O-A fluxes and the hydrological cycle over the Mediterranean.

## 414 **1. Introduction**

415 The Mediterranean region has been identified as one of the most prominent “Hot-Spots” in future climate  
416 change projections (Giorgi and Lionello, 2008). It is characterized by its vulnerability to changes in the water  
417 cycle (e.g. Chenoweth et al., 2011; García-Ruiz et al., 2011). General Circulation Model (GCM) and Regional  
418 Climate Model (RCM) simulations show a substantial precipitation decrease and a warming of the region,  
419 especially in the long warm and dry Mediterranean season. At the end of 21<sup>st</sup> century, the average of the  
420 model outputs predicts a significant loss of freshwater (+40% for the period 2070-2090 compared to 1950-  
421 1999; Sanchez-Gomez et al, 2009) over the Mediterranean region. More recently, Mariotti et al. (2015) have  
422 used the newly available Coupled Model Intercomparison Project-Phase 5 (CMIP5) experiments and show a  
423 significant increase of the projected surface air temperature (by ~+ 2-3 °C) for the 2071-2098 period  
424 compared to 1980-2005. These results need to be put in the context of an increasing anthropogenic  
425 pressure on the Mediterranean region, with an expected doubling of the population in countries around the  
426 Mediterranean basin in the next decades, with a contrast between a small decrease in European countries  
427 and a strong increase in African and Middle-East countries (Brauch, 2003). However, as highlighted by  
428 Mariotti et al. (2008), despite the high degree of model consistency, the results concerning the future  
429 climate projections for the Mediterranean Sea water budget from the global coupled models are still  
430 uncertain due to their horizontal spatial resolutions that are not capable of resolving the local to regional  
431 Mediterranean specific processes (air-sea exchanges, coastline, topography, north-south gradient of  
432 albedo). Indeed, the Mediterranean climate is affected by local processes induced by the complex  
433 physiography of the region and the presence of a large body of water (the Mediterranean Sea). For example,  
434 the Alpine chain is a strong factor in modifying traveling synoptic and mesoscale systems and the  
435 Mediterranean Sea is an important source of moisture and precipitation in the region (Gimeno et al., 2010;  
436 Schicker et al., 2010) and of energy for storms (Lionello et al., 2006). The complex topography, coastline and  
437 vegetation cover of the region are well known to modulate the regional climate signal at small spatial scales  
438 (e.g. Millan et al., 1997; Gangoiti et al., 2001; Lionello et al., 2006).

439 So far, most global and regional climate simulations have investigated the impact of global warming on the  
440 Mediterranean climate without detailed considerations of the possible radiative influence and climatic

441 feedback from the different Mediterranean aerosols (anthropogenic, marine, biomass burning, secondary  
442 biogenic and mineral dust particles). The Mediterranean region is rich in a variety of particles (natural and  
443 anthropogenic) from both continental and marine sources (Lelieveld et al., 2002). In figure 1, we illustrate  
444 the significant differences in aerosol loading between the eastern, central, and western sub-basins and  
445 between the North and the South of the Mediterranean shown by long-term aerosol satellite products. The  
446 aerosol optical depth (AOD), which represents the integration of the extinction by particles along the whole  
447 atmospheric column displays annual mean values (Figure 1) from 0.2 to 0.5 (in the visible wavelengths),  
448 depending on the aerosol types observed over the Euro-Mediterranean region (Nabat et al., 2013).

449 Numerous studies have documented the AOD for polluted-anthropogenic Mediterranean aerosols at local  
450 scale over southeastern France (Mallet et al., 2006; Roger et al., 2006), Spain (Horvath et al., 2002, Alados-  
451 Arboledas et al., 2003, 2008), Western Mediterranean (Lyamani et al., 2015), Greece (Chazette and Liousse,  
452 2001; Gerasopoulos et al., 2003), the **Greek island of Crete** (Fotiadi et al., 2006), and Italy (Tafuro et al.,  
453 2007, Ciardini et al., 2012). Under polluted conditions, they report low to moderate AOD values ranging  
454 between 0.1 to 0.5 (at visible wavelengths). In parallel, multi-year TOMS and MODIS observations over the  
455 eastern Mediterranean (Hatzianastassiou et al., 2009) or the Po Valley (Royer et al., 2010) indicate the  
456 occurrence of high AOD values (up to more than 0.8 at 500 nm) over large urban areas surrounding  
457 megacities.

458 Numerous studies (Markowicz et al. (2002), Ravetta et al. (2007), Liu et al. (2009), Kaskaoutis et al. (2011),  
459 Barnaba et al. (2011), Amiridis et al. (2012), Baldassarre et al. (2015)) have been also dedicated to biomass  
460 burning aerosols over the Mediterranean, which are mainly observed in July and August (driest months of  
461 the year) when the development of forest fires is favoured (Pace et al., 2005). Long-term observations of  
462 absorbing aerosols have clearly shown the major role of long range transport of biomass (agriculture waste)  
463 burning in the eastern Mediterranean (Sciare et al., 2008). AOD data available for smoke particles show  
464 “intermediate” values between those observed for dust and anthropogenic particles. For example, AOD  
465 ranging between 0.3 and 0.8 (Pace et al., 2005) have been observed at Lampedusa from 5 to 22 August  
466 2003, in relation with intense fires developed in southern Europe and transported over the Mediterranean  
467 basin during a regional heat wave. In addition, the STAAARTE-MED experiment (August 1998 in the Eastern

468 Mediterranean) has also documented a mean AOD of 0.39 (at 550 nm) for aged smoke plume from  
469 Canadian fires (Formenti et al., 2002). This kind of long-range transport has been also observed over the  
470 Western Mediterranean (Ortiz-Amezcuca et al., 2014).

471 Concerning natural aerosols, different cases of Saharan mineral dust have been regularly documented with  
472 local optical measurements on the island of Lampedusa by Meloni et al. (2003, 2004), who indicate  
473 moderate AOD (at 415.6 nm) of about 0.23-0.26 and one significantly larger event with AOD values of 0.51.  
474 Meloni et al. (2008) also report AOD (at 500 nm) measurements ranging between 0.29 and 1.18 for the  
475 1999 to 2006 period. For some extreme cases, dust AOD peaks may be even larger reaching values up to 2  
476 as observed by di Sarra et al. (2011). In parallel to Lampedusa observations, Kubilay et al. (2003) have also  
477 documented three dust intrusion events at Erdemli (Turkish coast), occurring in spring from central Sahara,  
478 in summer from eastern Sahara, and in autumn from the Middle East/Arabian peninsula. In each case, the  
479 presence of dust particles significantly increased the AOD, up to 1.8. Over the western Mediterranean,  
480 different studies also reveal the impact of Saharan dust that occasionally can lead to extreme events with  
481 AOD (at 500 nm) above 1 (Guerrero-Rascado et al., 2009).

482 For sea-spray particles, which are the second main natural species observed over the Mediterranean, Nabat  
483 et al. (2013) report a relatively low monthly mean AOD derived from satellites and modeling data, with  
484 values lower than 0.05 (in the visible wavelengths). By using recent improvements in the sea-spray emission  
485 scheme, Spada et al. (2013) show an averaged sea-spray AOD around 0.04 for the month of January (5 year  
486 period, 2002-2006) which is the favourable period for generating primary sea-spray due to strong sea-  
487 surface winds. Finally, and in the case of extreme wind episodes occurring over the western basin, Salameh  
488 et al. (2007) show that the amount of aerosol loading, solely due to the Mistral, Tramontane and Ligurian  
489 outflows, is as large as 3–4 times the background aerosol amount. They indicate that the contribution of  
490 sea-spray particles to the total aerosol loading and optical depth ranges from 1 to 10%. Salameh et al.  
491 (2007) report AOD around 0.15-0.20 (at 865 nm) within the sea-spray aerosol plume during such strong  
492 wind events. In addition, Mulcahy et al. (2008) reported a high correlation between AOD and wind-speed  
493 with AOD values of 0.3-0.4 at moderately-high wind speed.

494 In addition to AOD, the knowledge of SSA is essential to estimate the aerosol direct and semi-direct

495 radiative forcing. Concerning mineral dust particles observed over the Mediterranean, it should be noted  
496 that significant variations in SSA are reported, with values near 1 for purely scattering aerosols, and quite  
497 remarkable low values (0.74, 0.77 or 0.81) at Lampedusa (Pace et al., 2006; Meloni et al., 2003). At the high  
498 altitude Alpine Jungfrauoch station, SSA values are generally higher than 0.9 in case of African dust but  
499 occasional SSA as low as 0.75-0.80 are reported by Collaud-Coen et al. (2004). Intermediate values (0.85-  
500 0.92) have been also reported over the Mediterranean basin (Kubilay et al., 2003; Meloni et al., 2004; Saha  
501 et al., 2008). These estimates clearly indicate that significantly different SSA values are obtained following  
502 the dust particle origins and/or possible mixing of mineral dust with other species. For example, Kubilay et  
503 al. (2003) underlined the importance of mixing, showing SSA values clearly lower (0.85-0.90) in case of  
504 mineral dust transport coincident with urban-industrial aerosols, as compared to pure dust (0.96-0.97).

505 In addition, SSA observed in case of urban/industrial regimes has been also well documented over the  
506 Mediterranean Sea and coastal regions. In most cases, moderate or low SSA (0.78-0.94) is observed due to  
507 emissions containing absorbing black carbon aerosols. Over southeastern France, optical computations  
508 performed by Saha et al. (2008) and Mallet et al. (2004) indicate SSA values of 0.83 and 0.85 (at 550 nm)  
509 near the cities of Marseille and Toulon, respectively. Aircraft observations performed over the  
510 Marseille/Etang de Berre area during the ESCOMPTE campaign show values ranging between 0.88 and 0.93  
511 (at 550 nm) in the PBL (Mallet et al., 2005). These SSA values are close to those observed in South Spain  
512 (0.86-0.90) by Horvarth et al. (2002). Over southeastern Italy, Tafuro et al. (2007) reported a value of 0.94  
513 during summer time corresponding to anthropogenic particles. Finally, polluted particles transported over  
514 the Mediterranean basin have also relatively low values as reported by Markowick et al. (2002) over Crete  
515 Island (0.87) and by Di Iorio et al. (2003) (0.79-0.83) over the Lampedusa Island for two cases (25 and 27  
516 May 1999) of “aged” anthropogenic aerosols originating from Europe.

517 As opposed to dust and polluted aerosols, few studies have derived the biomass burning SSA over the  
518 Mediterranean Sea. One estimate has been obtained during STAAARTE-MED by Formenti et al. (2002) who  
519 reported a mean dry SSA of 0.89 (at 500 nm) for aged smoke from North America. Meloni et al. (2006)  
520 report estimations at Lampedusa with values of  $0.82 \pm 0.04$  (at 415 nm) for smoke aerosols over the  
521 Mediterranean region. The observed differences between SSA values could be due to the fact that the

522 smoke events described by Meloni et al. (2006) are more “local” and not (or somewhat less) mixed with  
523 other secondary species, as compared to biomass burning particles documented by Formenti et al. (2002),  
524 which were issued from very distant Canadian fires. Finally, at Palencia (Spain), Cachorro et al. (2008)  
525 reported a column-integrated SSA of 0.88 (at 440 nm) for a biomass burning event occurring in July 28,  
526 2004. It should be remained that most estimations of SSA over the Mediterranean have been obtained from  
527 surface in-situ or remote-sensing techniques. In that sense, the ChArMEx/ADRIMED project provides  
528 innovative observations of 3-D aerosol SSA, allowing investigating changes in its optical property during the  
529 transport of aerosols over the Mediterranean.

530 Concerning the aerosol vertical profiles and apart from a few airborne in-situ measurements (Formenti et  
531 al., 2002), most of the available information in the Mediterranean region comes from lidar observations,  
532 which provide highly resolved vertical profiles of aerosol backscattering at one or more wavelengths and,  
533 depending on the complexity of the instrumental setup, particles depolarization and extinction. Several  
534 sites are equipped with aerosol lidar systems and carry out regular observations in a coordinated way within  
535 the European aerosol research lidar network EARLINET (European Aerosol Research Lidar Network;  
536 Pappalardo et al., 2014; Wang et al., 2014). Numerous studies have been specifically dedicated to the  
537 vertical distribution of Saharan dust during extended time periods and/or selected events from various  
538 Mediterranean regions, mainly from ground-based systems: (i) the eastern basin in Thessaloniki (Hamonou  
539 et al., 1999; Balis et al., 2004), Crete (Balis et al., 2006), the Aegean sea (Dulac et al., 2003), and Athens plus  
540 Thessaloniki (Papayannis et al., 2005; Balis et al., 2006); (ii) the central basin in Lampedusa (Di Iorio et al.,  
541 2003; Meloni et al., 2004), Lecce (Tafuro et al., 2006), and at Etna (Tafuro et al., 2006); and (iii) across the  
542 western basin with the first spaceborne lidar (Berthier et al., 2006) and at Observatoire de Haute Provence  
543 (Hamonou et al., 1999), and Barcelona (Pérez et al., 2006; Sicard et al., 2011). Finally, using data from 20  
544 EARLINET lidar stations, Papayannis et al. (2008) indicate that African dust transport over the Mediterranean  
545 basin is layered. Their analysis confirms early observations by Hamonou et al. (1999) that not only different  
546 dust layers are superimposed at different altitudes, but that these layers have different source regions. The  
547 dust layers were generally detected between 1.8 and 9 km altitude.

548 Not only desert dust, however, can be transported above the marine atmospheric boundary layer. Balis et

549 al. (2004) report non-dust aerosols within elevated layers over Thessaloniki, and Formenti et al. (2002)  
550 report a forest fire haze layer from Canada observed from airborne measurements between approximately  
551 1 and 3.5 km above the northeastern Mediterranean in August 1998. Pérez et al. (2004) describe the  
552 complex interaction among orography, sea-breeze and pollution that cause the recirculation of pollutants  
553 and produce a strong layering with pollution aerosol layers above the boundary layer in the region of  
554 Barcelona. In addition, aerosol plumes are emitted sporadically in the Mediterranean free troposphere by  
555 Etna volcano. Such plumes have been observed to travel at altitudes between 4 and 5 km (Pappalardo et al.,  
556 2004) or above (Sellitto et al., 2015) at relatively short distance from Etna. To summarize, the lidar  
557 observations clearly show that only part of the aerosol transport occurs in the MBL demonstrating the need  
558 of using aircraft observations within the aerosol plume to determine the aerosol microphysical-chemical  
559 and optical properties of particles transported in altitude and so not detectable at the surface. Indeed,  
560 although lidar observations provide obviously crucial information on the aerosol vertical profiles, most of  
561 lidar systems cannot derive information on the aerosol size distribution, optical properties and chemical  
562 composition along the vertical. Such observations can only be obtained using in-situ aircraft vertical profiles  
563 as proposed in this ChArMEx/ADRIMED experiment. As an example, this project provides interesting and  
564 unique observations of 3-D aerosol size distribution during the transport over the Mediterranean basin,  
565 allowing to investigate changes in size distribution between mixed and pure mineral dust.

566 In terms of radiative effects, such atmospheric aerosol characteristics (loadings, absorbing properties,  
567 vertical layering) are known (Nabat et al., 2012; Papadimas et al., 2012; Zanis et al., 2012) to significantly  
568 change the radiative budget of the Mediterranean region by (1) decreasing the sea-surface incoming  
569 shortwave radiations, (2) increasing/decreasing outgoing shortwave fluxes depending on the surface albedo  
570 and (3) possibly heating turbid atmospheric layers when particles absorb solar light. This is the so-called  
571 aerosol "Direct Radiative Forcing (DRF)". As for the AOD, many of the aerosol DRF calculations are now  
572 referenced over the Mediterranean clearly showing that the DRF is significantly larger at daily time scales  
573 than the one exerted by the additional anthropogenic greenhouse gases.

574 Concerning polluted aerosols, shortwave DRF have been estimated by many authors (Horvath et al., 2002;  
575 Markowicz et al., 2002; Meloni et al., 2003; Roger et al., 2006; Mallet et al., 2006; Saha et al., 2008; di Sarra

576 et al., 2008; Di Biagio et al., 2009, 2010). Studies show significant decreases of surface solar fluxes of about  
577  $20\text{-}30\text{ W m}^{-2}$  (daily mean) for different locations as Almeria (South Mediterranean coast of Spain), Finokalia  
578 (Crete Island), Lampedusa, Marseilles and Toulon (southeastern France). In parallel, the combination of  
579 surface and satellite remote-sensing observations performed at Lampedusa have been used to perform  
580 calculations of the DRF, both in the shortwave (SW; Di Biagio et al., 2010) and longwave (LW; di Sarra et al.,  
581 2011; Meloni et al., 2015) spectral regions for different cases of Saharan dust intrusions. These studies  
582 emphasize that the radiative effect of desert dust in the LW spectral range is significant, and offsets a large  
583 fraction of the SW forcing (di Sarra et al., 2011; Meloni et al., 2015). More recently, Sicard et al. (2014a,  
584 2014b) have also produced estimations of the dust LW radiative effect, based on remote-sensing  
585 observations in Barcelona and 1-D radiative transfer calculations.

586 Concerning the smoke DRF, some calculations have been conducted over the Mediterranean region by  
587 Markowicz et al. (2002), di Sarra et al. (2008), Kaskaoutis et al. (2011) or Formenti et al. (2002). One  
588 estimate, proposed by Formenti et al. (2002) for an aged Canadian biomass-burning plume, reveals a  
589 significant SW surface dimming of about  $\sim 60\text{ W m}^{-2}$ . In addition, the DRF induced by smoke aerosols at  
590 Lampedusa between 3 and 23 August 2003, during the exceptionally hot and dry season, was derived by  
591 Pace et al. (2005) for the 300-800 nm spectral range. The smoke atmospheric forcing was estimated to be  
592 between  $+22$  and  $+26\text{ W m}^{-2}$ , with a corresponding SW heating rate possibly exceeding  $2\text{ K d}^{-1}$  at the smoke  
593 plume altitude.

594 At the regional scale, Papadimas et al. (2012) have proposed a recent estimation of the aerosol DRF using  
595 MODIS data from 2000 to 2007 for both all-sky and clear-sky conditions. They derived a multi-year regional  
596 mean surface of  $-19\text{ W m}^{-2}$ , associated with a TOA DRF of  $-4.5\text{ W m}^{-2}$ . Regional modelling studies have been  
597 also recently proposed by Nabat et al. (2012, 2015a) using the coupled-chemistry RegCM and the CNRM-  
598 Regional Climate System Model (RCSM) models for multi-year simulations. These works reported a mean  
599 regional surface (TOA) forcing of about  $-12\text{ W m}^{-2}$  ( $-2.4\text{ W m}^{-2}$ ) and  $-16\text{ W m}^{-2}$  ( $-5.7\text{ W m}^{-2}$ ) for the RegCM and  
600 CNRM-RCSM models, respectively. RegCM has been also used to investigate direct and semi-direct radiative  
601 effects of mineral dust over the Sahara and Europe in a test case of July 2003 (Santese et al., 2010). In this  
602 work, Santese et al. (2010) computed a daily-mean SW DRF of  $-24\text{ W m}^{-2}$  (resp.  $-3.4\text{ W m}^{-2}$ ) on 17 July and -



603  $25 \text{ W m}^{-2}$  ( $-3.5 \text{ W m}^{-2}$ ) on 24 July at the surface (TOA) on average over the simulation domain. Zanis et al.  
604 (2012) also proposed a regional estimate of the DRF of anthropogenic particles over the 1996-2007 period  
605 using RegCM and showed a significant forcing of up to  $-23 \text{ W m}^{-2}$  at TOA over Eastern Europe. In addition,  
606 Pere et al. (2011) have used the CTM-CHIMERE model coupled to the WRF model, for estimating the DRF of  
607 anthropogenic particles during the heat wave of summer 2003 and showed significant effects with  
608 implications on the planetary boundary layer height (decrease up to 30% in the presence of anthropogenic  
609 aerosols) and local air-quality. In addition to their important effects on the surface and TOA DRF, most of  
610 the Mediterranean aerosols are also able to absorb more or less effectively the solar radiations leading to a  
611 significant atmospheric forcing and associated SW heating rate. Local studies previously mentioned (Roger  
612 et al., 2006; Saha et al., 2008; Pace et al., 2005; Pere et al., 2011; Meloni et al., 2015) clearly report  
613 significant SW heating rate due to absorbing particles with values reaching up to 2-3 K per day, depending  
614 on the aerosol types. Finally, aerosols also have a significant effect on photolysis rates that may affect  
615 tropospheric chemistry and ozone production over the basin (Casasanta et al., 2011, Mailler et al., 2015).

616 In regards to such surface, TOA and atmospheric forcings, there is a need to investigate how the change in  
617 the radiative budget due to natural/anthropogenic aerosols influence the surface temperature (both over  
618 land and sea), relative humidity profiles, exchanges (latent heat fluxes) between ocean and atmosphere,  
619 cloud-cover (semi-direct effect of absorbing particles), precipitation and finally the whole Mediterranean  
620 hydrological cycle. The induced perturbations in the sea surface-atmosphere fluxes is expected to be  
621 important despite the relatively small size of the Mediterranean Sea, since this basin plays an important role  
622 at much larger scale by providing moisture for precipitation to its surroundings land region extending to  
623 northern Europe and northern Africa (Gimeno et al., 2010 and Schicker et al., 2010). Indeed and as shown  
624 by Ramanathan et al. (2001) for the Indian region or Foltz and McPhaden (2008) and Yue et al. (2011) for  
625 the Atlantic Ocean, a modification of the sea-surface evaporative fluxes, due to the dimming radiative effect  
626 of aerosols at the sea surface could significantly influence the lower troposphere moisture content and the  
627 associated precipitation distribution around the Mediterranean. In parallel, the absorbing particles over the  
628 Mediterranean (Mallet et al., 2013) could exert a semi-direct effect that could modify the vertical profiles of  
629 relative humidity and cloud cover, which has to be quantified. To our knowledge, there is no regional

630 climate simulation over the Mediterranean basin at this time that includes an Ocean-Atmosphere (O-A)  
631 coupled system model for investigating this specific question.

632 In that context of the referenced modelling and observations researchs over the Mediterranean basin, the  
633 main objectives of the ChArMEx/ADRIMED project were the following:

- 634 - to conduct an experimental campaign, based on surface and aircraft observations, for creating a rich 3-D  
635 database of physical, chemical and optical properties of the main Mediterranean aerosols, including (i)  
636 original in-situ aircraft observations of extinction coefficients, size distribution, black carbon concentrations  
637 as well as (SW and LW) radiative fluxes and associated heating rates, (ii) balloons observations of aerosol  
638 size distribution and (iii) surface measurements including original characterization of chemical properties
- 639 - to investigate how the aerosol size distribution and optical (especially SSA) properties evolve along the  
640 vertical, between the MBL and elevated layers, and during the transport over the Mediterranean
- 641 - to use experimental surface and aircraft observations to estimate the 1D-local DRF and forcing efficiency  
642 of different aerosols at the surface, TOA and within the atmospheric layer
- 643 - to investigate how the modifications of the radiative budget due to aerosols affect the sea-surface  
644 evaporation fluxes, relative humidity profiles, cloud-cover, precipitation and more largely the  
645 Mediterranean hydrological cycle

646 The present article describes the experimental setup of the campaign and the meteorological context and  
647 illustrates important results detailed in a series of companion papers. The rest of this article is divided into  
648 six different parts. In the first and second part (sections 2 & 3), we describe the in-situ and remote-sensing  
649 instrumentation deployed at the two super sites (Ersa and Lampedusa) and secondary sites (Minorca, Capo  
650 Granitola and the Barcelona and Granada EARLINET/ACTRIS stations), the additional AERONET/PHOTONS  
651 (AErosol RObotic NETwork / PHOTométrie pour le Traitement Opérationnel de Normalisation Satellitaire,  
652 <http://aeronet.gsfc.nasa.gov/>; Holben et al., 1998) and EARLINET/ACTRIS (European Aerosol Research Lidar  
653 Network / Aerosols, Clouds, and Trace gases Research InfraStructure Network, <http://www.actris.net/>;  
654 Pappalardo et al., 2014) network stations that we used, and the airborne observations obtained onboard  
655 the two French research aircraft (ATR-42 and F-20) and with sounding and drifting balloons. The section 4 is  
656 dedicated to present the main meteorological conditions, cloud cover and precipitation, which controlled

657 the aerosol emission and transport during the period of observations. The section 5 presents some  
658 examples of results concerning the in-situ and remote-sensing observations, in terms of aerosol physical,  
659 chemical, optical properties, and vertical profiles, as well as 1-D DRF SW and LW calculations. In the last part  
660 (section 6), the modelling effort is presented. Different models are involved in this project, from high  
661 resolution meteorological and chemistry transport models to regional climate models. The modelling results  
662 are used to describe the anthropogenic (carbonaceous, secondary inorganic and organic species) and  
663 natural (dust and sea-spray) loading and the estimated DRF at the regional scale for the period of  
664 experiment. An example of results of longer (inter-seasonal and inter-annual) aerosol-climate simulations is  
665 presented in the section 6, based on the work of Nabat et al. (2015a).

## 666 **2. Overview of the surface observation network**

667 The regional experimental set-up deployed in the western and central Mediterranean during the campaign  
668 ChArMEx SOP-1a is shown in Figure 2. **Two super sites (Cape Corsica and Lampedusa) and 10 secondary**  
669 **sites (Figure 2) have been used in this project.**

### 670 **2.1 The Cape Corsica and Lampedusa surface super sites**

671 Two super-sites were fully equipped for documenting the aerosol chemical, physical and optical properties  
672 as well as their possible mixing and their vertical structure at local scale (Table 1). The main characteristics  
673 of these two surface stations are presented here. The first station was located in Erba on Cape Corsica  
674 (42°58'10"N, 09°22'49"E), near the North tip of Corsica Island. This station was primarily instrumented for  
675 investigating polluted air masses transported over the Mediterranean basin from the highly industrialized  
676 regions of the Po Valley (Royer et al., 2010) and/or the Marseille-Fos-Berre (Cachier et al., 2005) zone and  
677 Rhone Valley. This ground-based remote station is located at an altitude of about 530 m above mean sea  
678 level (amsl) on a ridge equipped with wind mills and benefit from a direct view to the sea over a North  
679 sector of ~270° extending from the SW to SE. The Cape Corsica peninsula is a remote site ensuring that the  
680 in-situ measurements are not contaminated by local anthropogenic pollution.

681 The Lampedusa super-site (35°31'5"N, 12°37'51"E) was established at the "Roberto Sarao" station  
682 permanently operated by ENEA in the small island of Lampedusa (~20 km<sup>2</sup>), and it was augmented during  
683 the field campaign by the observations of the Portable Gas and Aerosol Sampling UnitS (PEGASUS) mobile

684 station operated by LISA . This surface station was mainly used for documenting very aged air masses in  
685 south westerly flow from Europe, southern air masses from northern Africa (Tunisia, Algeria and Libya)  
686 possibly laden with mineral dust, as well as marine aerosols. It is situated on a cliff at about 45 m amsl on  
687 the NE tip of the island.

688 The complete instrumentation deployed during the SOP-1a experiment for both super-sites is detailed in  
689 Table 1. Briefly, it served to determine the complete aerosol physical, chemical and optical properties as  
690 well as vertical profiles, and to measure radiative fluxes (broadband SW and LW, and spectral SW).

### 691 **2.1.1 In situ measurements at super-sites**

692 Both super-sites measured the mass concentration online using Tapered Element Oscillating Microbalance  
693 (TEOM) analysers. The number size distribution of particles are also measured, including fine and coarse  
694 fractions (radius ranges and corresponding instruments are reported in Table 1). The aerosol composition  
695 was derived from chemical analyses of filters and cascade impactors (DEKATI and MOUDI) with time  
696 resolution varying from 12 to 48h (depending on the aerosol load), but also from high-time resolution  
697 online measurements by an ACSM (Aerosol Chemical Speciation Monitor) at Ersa, a C-TOF-AMS (Time of  
698 Flight Aerosol Mass Spectrometer) at Lampedusa, and two PILS (Particle Into Liquid Sampler) systems at  
699 both sites (Table 1). The original observations of aerosol chemical properties obtained from PM10-PILS  
700 instrument at Ersa are detailed in Claeys et al. (2015). Concerning aerosol optical properties, scattering and  
701 absorption coefficients (at wavelengths listed in table 1) have been estimated for both super-sites using a 3-  
702  $\lambda$  nephelometer and a 7- $\lambda$  aethalometer, respectively. At Ersa station, the extinction coefficient (at 870 nm)  
703 was also estimated using a Photoacoustic Extinctionmeter (PAX) instrument, while it has been estimated at 2-  
704  $\lambda$  (450 and 630 nm) at Lampedusa using 2 Cavity Attenuated Phase Shift Spectroscopy (CAPS) systems.

705 Additional in-situ measurements were performed at the Ersa station. The mixing state of fine particles (at  
706 the two selected diameters of 50 and 110 nm in dry conditions) has also been estimated from their  
707 hygroscopic behaviour using a VHTDMA (volatilization and humidification tandem differential mobility  
708 analyser) system (Johnson et al., 2004). In parallel, a TSI (model 3800) aerosol time of flight mass  
709 Spectrometer (ATOFMS) (Gard et al., 1997) was used to measure the size-resolved chemical composition of  
710 single particles in the vacuum aerodynamic diameter ( $d_{va}$ ) size range 100–3000 nm.

### 711 **2.1.2 Remote sensing and radiation measurements at super-sites**

712 A Leosphere Raman lidar model RMAN510 was setup at low altitude (~11 m above sea level) in the small  
713 village of Macinaggio (42°57'44"N, 9°26'35"E) located on the eastern coast of Cape Corsica. The lidar was  
714 operated at about 6 km East from the Ersa station and less than 700 m from the shoreline. The RMAN510  
715 uses a laser emitting at 355 nm. It measures the total and polarized backscatter at 355 nm and the Raman  
716 nitrogen signal at 387 nm at night-time. A second ALS300 510 lidar system has been deployed in Lampedusa  
717 (Formenti et al., in prep.) as well as a more powerful University of Rome-ENEA homemade lidar measuring  
718 backscatter at 532 and 1064 nm (Di Iorio et al., in prep.). The main characteristics of lidar systems are  
719 provided and detailed in Table 1.

720 At each station, a multi-wavelength sun-photometer from the AERONET/PHOTONS network was operated,  
721 allowing the operational retrieval of column integrated AOD at 340, 380, 440, 500, 675, 870, 1020 nm (and  
722 also at 1650 nm at Ersa) and aerosols optical and microphysical properties such as the single scattering  
723 albedo, refractive index and particle size volume distribution (Dubovik and King, 2000; Dubovik et al., 2000,  
724 2002, 2006). The Ersa sun-photometer is positioned since June 2008 near the navy semaphore on the  
725 northwestern tip of Cape Corsica (43°00'13"N, 09°21'33"E, alt. ~75 m amsl) at about 4.2 km NNW of the  
726 Ersa surface station.

727 Both super-sites were complemented by a pyrgeometer and a pyranometer for monitoring longwave and  
728 shortwave downward fluxes measurements, respectively. Additional radiation measurements were  
729 performed at Lampedusa (Table 1). Spectral measurements of global, diffuse, and direct radiation were  
730 carried out with other instruments deployed by ENEA and the Physikalisch-Meteorologisches  
731 Observatorium Davos, World Radiation Center, (PMOD/WRC, Switzerland). Multi-filter rotating  
732 shadowband radiometer observations were carried out jointly with AERONET sun-photometer (di Sarra et  
733 al., 2015) and allowed the derivation of the AOD at several wavelengths. By combining these two  
734 measurements, a long-term series of AOD, started in 2001, was obtained. Measurements of the spectral  
735 actinic flux, allowing the determination of the photolysis rates (Mailler et al., 2015), were carried out with a  
736 diode array spectrometer. Measurements of broadband irradiance included a CG3 pyrgeometer sensitive to  
737 radiation in the atmospheric infrared window. Finally, the total ozone and spectral UV irradiance were

738 obtained with a Brewer spectrophotometer. Several radiosondes were also launched from Lampedusa  
739 during the SOP-1a, and vertical profiles of temperature and humidity were continuously measured by a  
740 microwave radiometer.

## 741 **2.2 The secondary sites**

### 742 **2.2.1 Montesorro station**

743 The Cape Corsica station was complemented by an additional remote-sensing setup at the peri-urban air  
744 quality station of Montesorro, southward of Bastia at about 45 m amsl (Leon et al., 2015), including a  
745 Leosphere model EZ lidar operating at 355 nm (42°40'17"N, 09°26'05"E) and a Cimel AERONET/PHOTONS  
746 sun-photometer (42°40'19"N, 09°26'06"E). In addition, some air-quality parameters were monitored by  
747 Qualitair Corse, including PM<sub>2.5</sub> and PM<sub>10</sub>. This station is less than 1 km far from the shore on the  
748 northeastern coast of Corsica, about 32 km South of Macinaggio.

### 749 **2.2.2 Barcelona station**

750 The Barcelona station (41.39°N, 2.11°E, 115 m amsl) was equipped with the following fixed instruments  
751 including an AERONET sun-photometer, an automated Sigma Space-NASA Micro Pulse Lidar (MPL) and a  
752 Universitat Politècnica de Catalunya (UPC) home-made multi-wavelength lidar (Kumar et al., 2011). The MPL  
753 lidar works at 532 nm and has a depolarization channel, while the UPC lidar works at 355, 532 and 1064 nm,  
754 and also includes two N<sub>2</sub>- (at 387 and 607 nm) and one H<sub>2</sub>O-Raman (at 407 nm) channels. The MPL system  
755 worked continuously. The UPC system was operated on alert in coordination with the two research aircraft  
756 plans involved in the SOP-1a campaign. The UPC system is part of the EARLINET network.

### 757 **2.2.3 Minorca station**

758 An additional station was setup during the campaign, located at Cap d'en Font, on the southeastern coast of  
759 the Balearic island of Minorca (Spain, 39°53'12"N and 4°15'31" E, ~10 m amsl), which is relatively central in  
760 the western Mediterranean basin. The Mobile Aerosol Station (MAS) of the LSCE (Laboratoire des Sciences  
761 du Climat et de l'Environnement) laboratory was equipped with the new Raman lidar WALI (Chazette et al.,  
762 2014a, 2014b), an AERONET/PHOTONS sun-photometer, and a set of in-situ instruments. A 5-wavelength  
763 Solar Light Microtops-II manual sun-photometer was also used. The WALI instrument, its calibration and the  
764 associated errors are documented in Chazette et al. (2014a). During all the experiment, the acquisition was

765 performed continuously with a vertical resolution of 15 m. AOD at the lidar wavelength of 355 nm has been  
766 extrapolated from that measured by sun-photometer at 380 nm and 440 nm using the Angström exponent  
767 (Chazette et al., 2015).

768 The in-situ instruments installed on-board the MAS included a 3-wavelength TSI nephelometer, a Magee  
769 Scientific Model AE31 7-wavelength aethalometer, a TEOM microbalance, and a Vaisala meteorological  
770 probe type PTU300. The nephelometer was sampling through a PM<sub>10</sub> inlet to measure the aerosol scattering  
771 coefficient at 3 wavelengths (450, 550 and 700 nm) with an integrating time step of 5-min. The  
772 aethalometer was sampling through a PM<sub>2.5</sub> inlet to measure aerosol absorption (at 7 wavelengths) and  
773 derive a 5-min average black carbon concentration. The TEOM measured dry PM<sub>10</sub> concentration every 30  
774 min. In addition two optical particle counters (OPCs) were installed outdoors next to the sun-photometer on  
775 a mobile platform. A MetOne HHPC-6 and a LOAC (Renard et al., 2015a, 2015b) respectively measured  
776 aerosol particle number concentration in 6 channels above 0.3µm in diameter and in 19 channels above 0.2  
777 µm. The LOAC instrument accuracy is discussed in detail by Renard et al. (2015a, 2015b).

#### 778 **2.2.4 Granada station**

779 The station of the Atmospheric Physics Group (GFAT) is located in the Andalusian Institute for Earth System  
780 Research (IISTA-CEAMA), in Granada, Spain (37.16°N, 3.61°W, 680 m amsl). The station is at a relatively  
781 short distance, about 200 km away, from the African continent and approximately 50 km away from the  
782 western Mediterranean Sea. During the SOP-1a campaign, lidar measurements were performed  
783 simultaneously with a multiwavelength Raman lidar and a scanning Raman lidar both from Raymetrics S.A.  
784 The multi-wavelength Raman system is part of the EARLINET network. In addition, a ceilometer was  
785 operated. Column integrated characterization of the atmospheric aerosol was performed following  
786 AERONET protocols with two Cimel sun-photometers deployed at two different heights: Granada (680  
787 m asl) and Cerro Poyos (37°6'32"N, 03°29'14"W, 1790 m asl) stations. In addition, in-situ instrumentation  
788 was continuously operated providing measurements of aerosol light-absorption coefficient at multiple  
789 wavelengths (multi-angle absorption photometer (MAAP) from Thermo ESM Andersen Instruments and  
790 Aethalometer model AE31), size distribution and particle number concentration for diameters larger than  
791 0.5 µm (TSI aerodynamic particle sizer APS model 3321) and light-scattering and backscattering coefficient

792 at dry and at relative humidity of 85% by means of a TSI tandem nephelometer humidograph system.  
793 Furthermore, the chemical composition in the PM<sub>1</sub> and PM<sub>10</sub> size fractions was determined during 16 and  
794 17 June by collecting aerosol samples using two high-volume samplers (Alados-Arboledas et al., in prep.).

### 795 **2.2.5 Capo Granitola station**

796 Several instruments were also deployed at Capo Granitola (37°34'N, 12°40'E), a site along the Southern  
797 coast of Sicily. The site, within a combined effort of ENEA, Univ. of Florence, and Univ. of Valencia, was  
798 equipped with a PM<sub>10</sub> sampler, a MultiFilter Rotating Shadowband Radiometer (MFRSR) to derive spectral  
799 AOD, and radiometers and spectrometers for the measurement of global, direct, and diffuse radiation  
800 throughout the SW and LW spectral ranges.

## 801 **2.3 Surface remote-sensing network**

802 Two surface remote-sensing networks were operated during the ChArMEx SOP-1a experiment, namely the  
803 AERONET/PHOTONS and EARLINET/ACTRIS (Pappalardo et al., 2014) networks. These networks were highly  
804 useful as they allow estimating the column-integrated aerosol loading as well as the vertical structure of  
805 particles.

### 806 **2.3.1 The AERONET/PHOTONS Sun-Photometer Network**

807 AERONET (Aerosol Robotic Network; <http://aeronet.gsfc.nasa.gov/>) is a federated network of ground-based  
808 sun-photometers and the associated data inversion and archive system, that routinely performs direct sun  
809 observations about every 15 min during daytime, and both almucantar and principal plane sky radiance  
810 measurements, at selected solar angles (Holben et al., 1998). Along with AOD observations, the AERONET  
811 aerosol retrieval algorithm (Dubovik and King, 2000) delivers the complete set of column-effective aerosol  
812 microphysical parameters, including volume size distribution, refractive index at several wavelengths and  
813 fraction of spherical particles (Dubovik et al., 2006). In addition, using these microphysical parameters, the  
814 algorithm provides other column-effective aerosol optical properties such as wavelength dependent SSA,  
815 phase function, and asymmetry parameter, as well as integral parameters of bi-modal particle size  
816 distributions (concentration, mode radii and variances) (Dubovik et al., 2002). The accuracy of AERONET  
817 retrievals is evaluated and discussed by Dubovik et al. (2000, 2002). In addition to microphysical and optical  
818 aerosol properties, we also have used direct radiative forcing calculations operationally provided at any



819 AERONET location as an operational product of the network. The method of derivation is described in detail  
820 by Garcia et al. (2012). Briefly, the broadband fluxes were calculated using the radiative transfer model  
821 GAME (Dubuisson et al., 2004; Roger et al., 2006) that has been integrated into operational AERONET  
822 inversion code. Sun-photometer stations used during the SOP-1a campaign over the Western basin are  
823 listed in the Table 2. The new instruments deployed specifically during the ChArMEx/ADRIMED project are  
824 the Ersa, Cap d'En Font, Cagliari and Majorque stations.

### 825 2.3.2 The EARLINET/ACTRIS network

826 Between 22 and 24 of June, four ACTRIS/EARLINET lidar stations (in addition to the EARLINET sites of  
827 Barcelona and Granada), were operated (Sicard et al., 2015a; Barragan et al., in prep.):

- 828 • Naples: backscatter (355 and 532 nm) and depolarization ratio (532 nm) profiles (22 June),
- 829 • Serra La Nave (Sicily): backscatter (355 nm) and depolarization ratio (355 nm) profiles (22 June),
- 830 • Potenza: extinction profiles (355 and 532 nm), backscatter (1064 nm) and depolarization ratio (532  
831 nm) profiles (22 and 23 June),
- 832 • Lecce: extinction (355 and 532 nm), backscatter (1064 nm), water vapour and depolarization ratio  
833 (355 nm) profiles (22 and 24 June),

## 834 3. Overview of the aircraft and balloon operations

### 835 3.1 Overview of the ATR-42 and F-20 flights

836 Figure 3 summarizes ATR-42 and F-20 flights trajectories performed during the experiment and their main  
837 characteristics. Most of the western Mediterranean basin has been investigated during the campaign by  
838 both aircrafts, excluding areas under the control of African aviation authorities where authorizations for  
839 scientific operations are very difficult to obtain. The first period of the campaign (16 to 20 June) was mainly  
840 dedicated to ATR-42 flights over Spain and Minorca islands (16-17 June, flights 29-32) and Southern France-  
841 Corsica Island (19-20 June, flights 33-34). During the second period (21-28<sup>th</sup> of June) of the SOP-1a, ATR-42  
842 flights have been mostly conducted over the Sardinia-Sicily-Lampedusa region in the central Mediterranean  
843 (flights 35-40). In July, two ATR-42 flights (41 and 42) were conducted over Lampedusa on 02-03 July and  
844 two others (43 and 44) on 04 July over the Gulf of Genoa. It should be noted that most ATR-42 flights  
845 included some transects at fixed altitudes (generally ~30 min of duration) associated with vertical profiles

846 over surface super-sites and secondary stations. Details about each flight track are available on the  
847 ChArMEx Operation Centre website (ChOC; <http://choc.seedoo.fr>). On Figure 3, F-20 flights trajectories are  
848 also indicated with the day corresponding to each flight. Except for the 16 and 17 June when F-20 is not  
849 flying, most of flights have been made jointly between the two aircraft. The longer flight range of the F-20  
850 allowed us to document the Tyrrhenian Sea (not covered by the ATR-42) and to perform vertical profiles of  
851 aerosols over Southern Italy in association with EARLINET/ACTRIS lidar observations. It should be finally  
852 noted the additional F-20 flight between Sardinia and Spain on 27 June specifically dedicated to sample a  
853 forest fire plume transported long-range from North America.

### 854 **3.2 In-situ and remote sensing observations on board the ATR-42**

855 The instrumentation deployed onboard the ATR-42, described in detail in Denjean et al. (2015) and Nicolas  
856 et al. (in prep.) is summarized in Table 3. It is analogous to the one used for the two super-sites and was  
857 devoted to the characterization of microphysical, chemical and optical properties of aerosols that have been  
858 advected above the MBL and so not detectable at the surface. As indicated in Table 3, the number size  
859 distribution of aerosols, including fine and coarse fractions, as well as the total concentration of particles  
860 have been evaluated using SMPS, GRIMM, FSSP and UHSAS systems. The corresponding size ranges for all  
861 instruments are indicated in Table 3. A  $3\text{-}\lambda$  nephelometer and  $1\text{-}\lambda$  Cavity Attenuated Phase Shift (CAPS  
862 PMex) particle light extinction monitor system (Petzold et al., 2013) have been used conjointly for  
863 estimating scattering and extinction properties of particles. The CAPS-PMex system, used for the first time  
864 onboard the ATR-42, provides an additional constrain on the aerosol optical properties, useful to determine  
865 the absorbing properties. Indeed, the aerosol absorbing characterization remains largely challenging using  
866 filter techniques (Moosmüller et al., 2009). These optical inter-comparisons have been performed for  
867 different aerosol plumes and are presented in Denjean et al. (2015).

868 In addition, passive remote-sensing observations have been conducted during the SOP-1a experiment using  
869 the PLASMA (Photomètre Léger Aéroporté pour la Surveillance des Masses d'Air) system, which is an  
870 airborne sun-tracking photometer with two main characteristics: lightness and a wide spectral coverage (15  
871 channels between  $0.34\text{--}2.25\ \mu\text{m}$ ; see Karol et al., 2013). The instrument contains also a microprocessor  
872 which derives the Sun position depending on time, latitude, longitude (provided by a GPS system) and the

873 rotation of the airborne (provided by a gyroscope). Spectral AOD is derived from these direct sun  
874 measurements and the calibration coefficients. During the campaign, several AOD comparisons were done  
875 between PLASMA and AERONET/PHOTONS sun-photometers (Cagliari, Lampedusa, Granada) showing  
876 differences within 0.01 at all wavelengths. Moreover, as a consequence of performing AOD measurements  
877 at different heights, the aerosol extinction vertical profiles have been also obtained during every  
878 landing/taking off and during pre-scheduled vertical profiles (Torres et al., this special issue). Finally, upward  
879 and downward radiative fluxes (SW & LW) have been measured onboard the ATR-42 by means of CMP22  
880 and CGR4 radiometers calibrated before the campaign.

### 881 **3.3 Remote-sensing observations on board the F-20**

#### 882 **3.3.1 LNG observations**

883 The LEANDRE Nouvelle Generation (LNG) was used in its backscatter configuration during the ChArMEx-  
884 ADRIMED field operation onboard the SAFIRE F-20 aircraft. In the present campaign, the LNG system  
885 involved three elastic channels at 1064, 532 and 355 nm. Depolarization was also measured in a fourth  
886 channel operating at 355 nm. The profiles of atmospheric particulate extinction and backscatter coefficients  
887 are then retrieved. Zenith pointing lidar measurements were taken before most of the flights from the  
888 ground at the Cagliari airport (39.25 N, 9.06 E) in Italy. Lidar observations allow the detection of biomass  
889 burning plumes (BBP) (see part 4.3) arriving at the Cagliari airport on 28 June as described by Ancellet et al.  
890 (submitted).

#### 891 **3.3.2 OSIRIS observations**

892 OSIRIS (Observing System Including Polarisation in the Solar Infrared Spectrum) is an instrument devoted to  
893 observation of the polarization and directionality of the solar radiation reflected by the surface-atmosphere  
894 system. OSIRIS is based on the same imaging radiometer concept as the POLDER instrument (Deschamps et  
895 al, 1994). It includes two optical systems: one for the visible and near infrared range (VIS-NIR, from 440 to  
896 940 nm) and the other for the shortwave infrared (SWIR, from 940 to 2200 nm). OSIRIS has eight spectral  
897 bands in the VIS-NIR and six in the SWIR. During the SOP-1a campaign, OSIRIS was flown aboard the French  
898 F-20 aircraft and looked at nadir. The quantities used to derive the aerosol and cloud properties from OSIRIS  
899 are the normalized total and polarized (unitless) radiances. The aerosol algorithm used for OSIRIS over

900 ocean is an optimal estimation method (OEM), similar to the one described in Waquet et al. (2013). For  
901 ocean targets, we use all the available angular and polarized information acquired in three spectral bands  
902 (490, 670 and 865 nm) to derive the aerosol parameters and some properties of the surface. A combination  
903 of two log normal size distribution functions is assumed (i.e. a fine mode and a coarse mode) as well as a  
904 mixture of spherical and non-spherical particles (Dubovik et al., 2006). The main retrieved parameters are  
905 the aerosol AOD, SSA, the fraction of spherical particles within the coarse mode and the complex refractive  
906 index.

### 907 **3.4 Balloons operations**

908 Instrumented balloons were launched by the French Space Agency (CNES) from the airfield of Sant Lluís  
909 (39°51'55"N, 04°15'15", 55 m asl) on Minorca Island, less than 6 km NE of the Cap d'en Font station  
910 described above. Two types of balloons were launched to document dust transport events: (i) ascending  
911 dilatable rubber balloons, and (ii) quasi-Lagrangian spherical pressurized drifting balloons, called BPCL  
912 (Ballon Pressurisé de Couche Limite, or boundary-layer pressurized balloons).

913 A total of 15 sounding balloons were launched during the campaign between 12 June and 02 July (Table 4)  
914 and most balloons reached more than 30 km in altitude. Except for the first test balloon on June 12, the  
915 payload of sounding balloons included a pair of meteorological sondes with temperature, humidity and GPS  
916 sensors allowing the retrieval of the position ( $\pm 10$  m), derived pressure ( $\pm 1$  hPa) and wind ( $\pm 0.15$  m s<sup>-1</sup>),  
917 respectively coupled, for certain flights (see Tables 4 and 5), to an ozone electrochemical sonde (Gheusi et  
918 al., in prep.) and a LOAC OPC (Renard et al., 2015a, 2015b). Balloon trajectories were confined within the  
919 area 39-41.2°N in latitude and 3-5°E in longitude.

920 BPCLs are designed to drift and make observations with a payload of a few kg in the lower troposphere for  
921 durations of up to several weeks (Vialard et al., 2009). Two versions were used, the standard one of 2.5 m in  
922 diameter, launched pressurized, which is limited to a maximum float altitude of about 2.5 km (Ducrocq et  
923 al., 2014), and one developed for ChArMEx of 2.6 m in diameter, launched unpressurized to reach a float  
924 altitude of more than 3 km in altitude. The payload was composed of a GPS system, PTU instruments on the  
925 upper pole of the balloon, a LOAC instrument on the lower pole of the balloon and two solar radiation  
926 sensors for upward and downward solar flux measurements. In addition a BPCL equipped with a modified

927 ozone electrochemical sonde (Gheusi et al., in prep.) instead of a LOAC was launched in parallel of a LOAC  
928 balloon on 4 occasions on 16 and 17 June (BPCL B53 and B54, respectively), and on 02 July (BPCL B55 and  
929 B57). 14 BPCL balloons were launched in total between 16 June and 02 July 2013 (Table 5). Trajectories are  
930 plotted in Figure 4 with a visualization of daytime vs. night-time conditions. The longest flight in terms of  
931 distance (1053 km) and time duration (32.6 h) was the ozone BPCL B57, which passed the Sicily strait and  
932 reached the southern limit of the authorized flight domain south-south-west of Malta. Communication  
933 failure occurred with the two balloons B53 and B70. Flights were automatically terminated by drilling the  
934 envelope at a distance of 30 km from southeastern French coasts, western Sicily coast, or North Tunisian  
935 coast. BPCL float altitudes ranged between about 1850 and 3350 m amsl (balloon B54 with an ozone sonde  
936 and B71 with a LOAC, respectively). Pairs of balloons with LOAC measurements were launched at different  
937 float altitudes to document Saharan dust transport on June 16 (2100 and ~3100 m amsl) and June 19 (2550  
938 and ~3500 m amsl).

#### 939 **4. Overview of Meteorological Conditions**

##### 940 **4.1 Synoptic Situation**

941 As mentioned below, the SOP-1a experiment was mostly characterized by moderate aerosol loading mainly  
942 controlled by the contribution of mineral dust particles. This situation is well observed through the AOD  
943 derived by MODIS (Tanré et al., 1997), MISR (Kahn et al., 2010), PARASOL (Tanré et al., 2011) or SEVERI  
944 (Thieuleux et al., 2005) sensors and averaged for the June-July 2013 period (Figure 5), which show an  
945 average AOD ranging between 0.2 and 0.4 (at 550 nm) over the western and central Mediterranean basins.  
946 During the SOP-1a, distinct meteorological conditions have led to the transport of mineral dust over the  
947 basin as shown in the Figures 5 and 6. Figure 7 shows the dust mass concentration together with the  
948 geopotential and wind at 700 hPa for the 16 June, 19 June, 22 June, 29 June and 02 July. In the following  
949 sections, we discuss the meteorological conditions (surface wind, sea level pressure, 700 hPa geopotential  
950 and wind direction) for these different days in order to understand the transport of mineral dust aerosols  
951 over the Mediterranean.

952 Wind direction and intensity vertical profiles as simulated by the ALADIN regional model (outputs every 3  
953 hours) as a function of time, for the 11 June to 06 July period and for the whole SOP-1a period at three

954 different sites: Ersa, Minorca and Lampedusa islands are shown in Figure 8. At the beginning of the SOP-1a,  
955 the northwestern Mediterranean area was under the influence of a large pressure ridge at 700 hPa,  
956 generating a westerly to south-westerly flow over Spain and southern France. Over Minorca, the near  
957 surface (1000 - 850 hPa) winds were generally from the easterly to north-easterly direction (indicated by the  
958 blue color in the Figure 8) while the wind direction estimated between 700 and 500 hPa was clearly from  
959 the south, southwest direction (brown color), which is a favourable condition for the transport of mineral  
960 dust above South-Spain and then Balearic islands (Figure 6). This point is well observed in figure 7, showing  
961 the geopotential at 700 hPa for the 16<sup>th</sup> of June. The general circulation at 700 hPa during this dust event  
962 indicates a reinforcement of the southwesterly winds in southern Spain advecting air masses with large  
963 concentrations of dust aerosols as shown by SEVIRI AOD (AOD of 0.4-0.5) for that day (Figure 6). A low  
964 pressure system moved from the British Isles towards the Gulf of Biscay and then the Iberian Peninsula  
965 between the 17<sup>th</sup> and 20<sup>th</sup> June, leading to veering winds that became southerly over the northwestern  
966 Mediterranean. Thus in Minorca, the direction of the wind changed from easterly to southerly direction  
967 between 1000 and 850 hPa. A more pronounced southerly-southwesterly flow was also observed at 700  
968 hPa in Minorca (19<sup>th</sup>-21<sup>st</sup> of June) as shown by the geopotential at 700 hPa. This circulation characterized by  
969 the presence of the low geopotential over the Gulf of Biscay induced a strong southerly flow at 700 hPa  
970 between the Balearic and Corsica islands associated with large dust optical depth concentrated in this zone  
971 as shown by SEVIRI AOD (AOD of 0.3-0.4) for 19<sup>th</sup> June (Figure 6). This period of the SOP-1a corresponds to  
972 the two ATR-42 flights 33 and 34 (Figure 3). After 20<sup>th</sup> June, this low pressure system moved eastward,  
973 generating a trough located between France and Italy, and inducing a waving westerly flow over the north-  
974 western Mediterranean. As a result, the aerosol loading over the western basin decreased between 21<sup>st</sup> and  
975 24<sup>th</sup> June, but the westerly (resp. northerly) winds observed at 700 hPa in Minorca (resp. Ersa) (Figure 8)  
976 reinforced the transport of dust aerosols over the central basin and the Lampedusa station (where winds  
977 were from the north westerly direction at 3 km height). These meteorological conditions lead to an increase  
978 of the dust optical depth over the central Mediterranean as shown by the SEVERI instrument and  
979 AERONET/PHOTONS data. Between 25<sup>th</sup> and 29<sup>th</sup> June, a northwesterly flow set up between the Gulf of  
980 Lions and Sicily. The vertical profiles of the wind direction reveal a remarkable transition on 29<sup>th</sup> June with

981 significant changes in direction from westerlies to north, north-westerlies, notably over the Minorca and  
982 Ersa stations above 850 hPa. The 700 hPa geopotential field on 29 June at 1200 UTC from the ALADIN  
983 atmospheric model analysis shows a maximum over the Atlantic Ocean whereas a deep low pressure  
984 system was located over southern Algeria. This strong geopotential gradient lead to intense northerly to  
985 north-westerly winds at 700 hPa over the western basin leading to significant AOD over Libya (AOD of 0.4-  
986 0.5) and the Alboran sea (AOD of 0.5-0.6) as shown in Figure 6. These meteorological conditions lead to low  
987 dust optical thickness over the central Mediterranean as observed by AERONET/PHOTONS data. Finally,  
988 during the last period of the SOP-1a experiment, (30 June - 05 July), weather conditions became more  
989 anticyclonic over the region while low systems were confined to northern Europe. Figure 8 shows north-  
990 westerly winds in the whole troposphere in Lampedusa and Minorca, limiting the presence of dust aerosols  
991 to the southern part of the north-western Mediterranean.

#### 992 **4.2 Surface temperature, cloud cover and precipitation**

993 In terms of surface temperature, which is one of the most important meteorological variables that control  
994 biogenic or biomass burning aerosol emissions over the Euro-Mediterranean region, the summer 2013 was  
995 mostly characterized by moderate values as shown in Figure 9. Indeed, during the SOP-1a period, surface  
996 temperatures (in °C and at 12:00 UTC) derived from NCEP reanalysis (Kalnay et al., 1996) for different days  
997 reveal moderate values especially over the western Mediterranean region (South-West France and Spain).  
998 One can observe temperatures of about 15-20°C (at 12:00 UTC) over Spain and Portugal, which are one of  
999 the main regions of the Mediterranean where large fire events occur. In addition, part of France was also  
1000 characterized by moderate surface temperature but slightly higher than over Spain especially over  
1001 northeastern regions. A strong west to east gradient is observed over Europe with strongest values over the  
1002 eastern regions (around 30°C over Greece and the Balkans) compared to the western basin. A similar  
1003 conclusion is obtained over the Mediterranean Sea with differences of about 5°C between the eastern  
1004 (around 25°C for the SOP-1a period) and the western (around 20°C) basin. Among other factors (such as  
1005 cloud fraction and shortwave radiations), such moderate surface temperatures do not create favourable  
1006 meteorological conditions to produce intense Mediterranean biomass burning events and/or significant  
1007 production of secondary organic and inorganic aerosols. Concerning smoke aerosols, GAFS-V1 emission

1008 data, analysed for the SOP-1a period, do not reveal important primary BC and OC fluxes emissions (not  
1009 shown). This is consistent with the APIFLAME biomass burning emission estimates (Turquety et al., 2014)  
1010 data as reported by Menut et al. (2015).

1011 During the SOP-1a, the cloud cover retrieved over the Euro-Mediterranean region (excluding the  
1012 Mediterranean Sea) from CRU (Climate Research Unit) data (Harris et al., 2013) (Figure 10) indicates the  
1013 largest values (between 75 and 95%) over France, Benelux and Eastern Europe regions. In parallel, southern  
1014 France, as well as western Spain and the Balkans are characterized by moderate cloud cover with values  
1015 around 50-60 % for June 2013. Over the Mediterranean coast, the cloud cover strongly decreases for most  
1016 of countries, with values lower than 40 %. Such spatial cloud cover (observed during the SOP-1a) over the  
1017 Euro-Mediterranean could limit the photochemical processes over the main anthropogenic sources (such as  
1018 the Benelux and Po Valley) and the associated production of secondary aerosols. This could explain for a  
1019 part the low to moderate contribution of fine anthropogenic particles to the total atmospheric loading  
1020 during the SOP-1a. In parallel, the mean precipitation (averaged for June 2013), obtained from the TRMM  
1021 (Tropical Rainfall Measuring Mission) instrument over land and sea (CRU observations are only available  
1022 over land, see Figure 10), are found to be very heterogeneous over the Euro-Mediterranean continental  
1023 region, with some important values over the Balkans, Alps and eastern Europe (from 100 to 250 mm for the  
1024 month of June 2013) and moderate values over Italy, Croatia, western France and Benelux (80 to 100 mm,  
1025 as shown in the Figure 11). Over the Mediterranean Sea, southern Spain and northern Africa, the  
1026 precipitation was smaller, with most of values lower than 20 mm during the SOP-1a.

1027 To summarize, this global view of the synoptic situation, cloud cover and regional precipitation patterns  
1028 indicate that the meteorological conditions during the experimental campaign were favourable to moderate  
1029 mineral dust emissions, associated with a weak contribution of anthropogenic aerosols over the western  
1030 basin. This important characteristic of the SOP-1a is well observed in Figure 12, which indicates the AOD  
1031 anomalies (calculated for the period 2000-2013) of summer 2013 compared to all AOD summer derived  
1032 from MODIS and MISR data. Indeed, negative AOD anomalies of about -0.05 are found over the western  
1033 Mediterranean basin for the summer 2013, both from MODIS and MISR observations. To conclude, it  
1034 appears that the period of observations during the SOP-1a was characterized by aerosol concentration



1035 slightly lower but in the same range of magnitude that usually observed during summer over the western  
1036 Mediterranean. The level of aerosol concentration was found to be moderate but allows investigating  
1037 several dust and sea-spray events as well as an interesting intense biomass burning plume advected from  
1038 North America.

### 1039 **4.3 An aged smoke plume advected over Europe**

1040 During the SOP-1a, several large forest fires occurred in North America (Colorado, Alaska, Canada) from  
1041 June 17<sup>th</sup> to 24<sup>th</sup>, 2013, as identified by the MODIS instrument. Absorbing aerosol index produced from  
1042 GOME-2 by KNMI (<http://www.temis.nl/aviation/aai-pmd-gome2b.php?year=2013>) shows that a large  
1043 smoke plume crossed the north Atlantic and reached Western Europe coasts on June 25. Main fire areas,  
1044 with fire radiative power higher than 50 MW (Shroeder et al., 2010), have been detected over Canada  
1045 (Ancellet et al., submitted). Average MODIS AOD during the same period (23 to 28 June 2013) indicate  
1046 values as high as 1 over the Atlantic Ocean, suggesting that a significant fraction of the aerosol produced by  
1047 the fires was transported to Western Europe during the ChArMEx/ADRIMED field campaign. To investigate if  
1048 the western Mediterranean has been impacted by these fires, a forward simulation of the Lagrangian plume  
1049 dispersion model FLEXPART (Ancellet et al., submitted) has been conducted to quantify the spatial extent of  
1050 the fire plume transport for 11 days. Fires emissions areas were identified by MODIS observations over  
1051 several locations in Canada and Colorado. The aerosol mass is emitted in the transport model from June  
1052 17<sup>th</sup> to 28<sup>th</sup> in a 3 km layer as suggested by the CALIOP lidar observations over Canada. The biomass  
1053 burning plume reaches much lower latitudes over Europe, down to the Western Mediterranean 4-10 days  
1054 after the emission in Canada. During the SOP-1a, the plume was mainly present in the altitude range of 2.5 -  
1055 4.5 km and has been sampled by many remote sensing and in-situ instruments on June 27<sup>th</sup> and 28<sup>th</sup>; at  
1056 Minorca and Cagliari surface stations, and between Sardinia and Lampedusa onboard the ATR-42 aircraft.

## 1057 **5. Overview of aerosol physical-chemical-optical properties, vertical profiles and local direct** 1058 **radiative forcing**

### 1059 **5.1 Aerosol physical and chemical properties**

#### 1060 **5.1.1 Aerosol mass and number concentration at the two super-sites**

1061 First, PM concentrations between the two different stations are reported in the Figure 13, which reports the

1062 daily time-series of PM1 and PM10 at Ersa, as well as PM10 and PM40 at Lampedusa. The results indicate a  
1063 significantly higher mass concentration at Lampedusa compared to Ersa. Indeed, the mass concentration  
1064 observed at Lampedusa is comprised between 10 and 30  $\mu\text{g m}^{-3}$ , with a mean of 21  $\mu\text{g m}^{-3}$ , which is two  
1065 times higher than the averaged PM10 ( $\sim 9 \mu\text{g m}^{-3}$ ) measured at Ersa. One can note the significant peak of  
1066 PM40 (maxima of 75  $\mu\text{g m}^{-3}$ ) at Lampedusa during the 24 to 26 June period that corresponds to a significant  
1067 production of primary marine aerosols. Finally, the PM1 concentration at Ersa is found to be almost  
1068 constant during the period of the campaign, with a mean value of 6  $\mu\text{g m}^{-3}$ . In order to take into account the  
1069 difference of altitudes between the two sites of Lampedusa and Ersa, we have applied a correction factor to  
1070 PM10 observed at Ersa (530 m) for estimating a new PM10 concentration corresponding to the altitude of  
1071 Lampedusa. In that sense, we have applied the logarithmic law reported by Piazzola et al. (2015) using a  
1072 value of 0.75 for the factor  $s$  to correct the mass concentration of sea spray aerosols only. The calculated  
1073 mean value of PM10 is about 12  $\mu\text{g m}^{-3}$  (Figure 13), closer to the mean value observed at Lampedusa (21  $\mu\text{g}$   
1074  $\text{m}^{-3}$ ). In addition, the background aerosol number concentrations (for  $D_p > 0.01 \mu\text{m}$ ) observed within the  
1075 boundary layer in Corsica averaged  $\sim 2000 \text{ cm}^{-3}$  (not shown). The lowest concentrations ( $\sim 200 \text{ cm}^{-3}$ ) resulted  
1076 from aerosol activation to cloud droplets, and scavenging from cloud droplets and rain drops, while high  
1077 concentrations as high as 10000  $\text{cm}^{-3}$  were observed during pollution events from continental European air  
1078 masses. The number concentrations showed a diurnal cycle suggesting that the site was situated within the  
1079 marine boundary layer during daytime and within the free troposphere during night-time. The analysis of  
1080 the diurnal variation of the particle number size distribution is further indicating that nucleation events also  
1081 increased the particle number concentration during daytime, about one third of the time (Sellegrì et al., in  
1082 prep.). The periods of high aerosol number concentrations detected between the 12<sup>th</sup> and 25<sup>nd</sup> of June were  
1083 also dominated by a single mode with diameters between 30 and 150 nm. The small Aitken mode ( $d_g < 50$   
1084 nm) associated with pollution events suggests a relatively fresh aerosol that has been formed during  
1085 transport from the European continent. The largest mode ( $d_g \sim 150 \text{ nm}$ ) occurred during the dust event on  
1086 18 June.

### 1087 **5.1.2 Columnar particle volume size distribution**

1088 We have used the column-integrated particle size volume distributions derived from AERONET/PHOTONS

1089 sky radiance measurements (Dubovik et al., 2000). These size distributions allow investigating the changes  
1090 in aerosol size distribution between different stations during the SOP-1a and over the western basin. Four  
1091 different stations have been studied, which include the two super-sites of Lampedusa and Ersa, as well as  
1092 the aircraft and balloon base stations; Cagliari and Cap d'En Font, respectively. Daily volume size  
1093 distributions for both sites are represented in the Figure 14, as well as the averaged (red curve) size  
1094 distribution for the whole period (1 June to 5 July) and the number of observations. In addition, the mean  
1095 values of the volume radius, concentration of fine and coarse mode and the standard deviations of the  
1096 volume size distribution are reported in the Table 6. It should be noted that the scales of the y-axis are  
1097 different for each figure. One can note the bimodal size distribution for both stations with large spread of  
1098 radius values, especially for the coarse mode. The most important concentrations are obviously observed in  
1099 Lampedusa, near the mineral dust sources, with maxima of  $\sim 0.12 \mu\text{m}^3 \mu\text{m}^{-2}$  for the coarse mode. In parallel,  
1100 the lowest concentrations are observed at the Ersa station due to the absence of intense polluted-  
1101 photochemical or smoke aerosol events over southern France and Italy during the SOP-1a. In that sense, the  
1102 mean contribution (red curve) of the coarse mode to the aerosol volume size distribution appears to be  
1103 predominant at most sites, except at the Ersa station. However, the inclusion of the corrected factor  
1104 (Piazzola et al., 2015) for taking into account the altitude of the Ersa site reduces slightly the differences in  
1105 the concentration of the coarse mode with the Lampedusa station (see Table 6). This point is well noted for  
1106 the Cap d'En Font station, where the concentration of each modes appear as equivalent, due to the absence  
1107 of pollution from the Iberian Peninsula during the period of observations. For this site, it is interesting to  
1108 note the intense peak of concentration ( $0.08 \mu\text{m}^3 \mu\text{m}^{-2}$ ) for the 27<sup>th</sup> June, which is due to the transport of an  
1109 important smoke plume over the Mediterranean (see Ancellet et al., submitted; and Chazette et al.,  
1110 submitted). Finally, the contribution of the coarse mode clearly increases for the two other, more southern  
1111 Italian sites of Cagliari and Lampedusa, which are more affected by the mineral dust compared to Ersa and  
1112 Cap d'En Font. The variability of AERONET products collected over a period of four years at Ersa and Palma  
1113 de Mallorca, near Cap d'En Font, is reported in Sicard et al. (2015b, this special issue). It is interesting to  
1114 note the variability ( $\pm 0.05$ ) in the derived size of the coarse mode at Lampedusa (see Table 6), which will be  
1115 analysed in regards to dust sources in a future study. The derived volume concentrations over these two

1116 stations highlight the moderate dust activity occurring during the SOP-1a experiment, when compared to  
1117 stations under high dust conditions. As an example of comparisons, Dubovik et al. (2002) reported a large  
1118 range of concentration for the coarse mode for dusty sites (such as Cape Verde or Solar Village), which are  
1119 characterized by larger concentrations, close to  $0.30 \mu\text{m}^3 \mu\text{m}^{-2}$ . In parallel, the Bahrain (Persian Gulf)  
1120 AERONET station is characterized by a concentration of  $0.14\text{-}0.15 \mu\text{m}^3 \mu\text{m}^{-2}$ .

### 1121 **5.1.3 Particle size distribution during transport**

1122 Figure 15 presents an example of the evolution of the aerosol particle number concentrations in the 19  
1123 particle size classes of the LOAC instrument as measured along the northward trajectory of the BPCL balloon  
1124 B74 from Minorca Island to the French coast (see Figure 4). The balloon was launched at 09:46 UTC on 16  
1125 June 2013 during a moderate desert dust event shown on top of Figure 6 (AERONET-derived AOD at 500 nm  
1126 of 0.15). It drifted at a constant altitude of  $\sim 2.1$  km at the bottom of the African dust layer observed with  
1127 the WALI lidar at Minorca (not shown; see Chazette et al., 2015), and was automatically forced to land on  
1128 the sea before reaching the coast South of Marseille, after a 12-h flight of 368 km. The dominant mineral  
1129 dust nature of the particles was confirmed by the LOAC particle typology measurements (Renard et al.,  
1130 2015b). The figure illustrates that LOAC has detected large particles of up to  $50 \mu\text{m}$  in diameter, although  
1131 the plume originated from North-Africa a few days before (Renard et al., 2015b). The concentrations of  
1132 particles remained relatively constant during the flight, suggesting either no significant sedimentation of the  
1133 largest particles during the flight or compensation by particles coming from above. The BPCL balloon B70  
1134 launched a few minutes later drifted at an upper altitude of  $\sim 3.1$  km and followed a different trajectory  
1135 towards East (Figure 4) but showed a quite similar extended particle size range with larger concentrations in  
1136 almost all channels except the extremes (not shown). The 4 other drifting balloons launched in the dust  
1137 layer during this event on June 17 and 19 (Table 5) did confirm the presence of very large particles ( $>20 \mu\text{m}$ ),  
1138 which cannot be reported by AERONET particle size distribution retrieval algorithm (Hashimoto et al., 2012).  
1139 In addition, observations of large particles ( $>15 \mu\text{m}$ ) was systematically found during all other LOAC balloon  
1140 flights drifting in African dust layers, which will need further analysis to better understand the process that  
1141 can maintain such large particles in suspension during several days.

1142 Concerning the aerosol microphysical properties, aircraft observations have allowed to investigate the

1143 vertical structure of aerosol size distribution showing particles characterized by large size ( $>10\ \mu\text{m}$  in  
1144 diameter) within dust plumes. In addition, in most of cases, a coarse mode of mineral dust particles,  
1145 characterized by an effective diameter  $D_{\text{eff},c}$  ranged between 5 and  $10\ \mu\text{m}$ , has been detected within the dust  
1146 layer located above the MBL. Such values are found to be larger than those referenced in dust source region  
1147 during FENNEC, SAMUM1 and AMMA, as well as measurements in the Atlantic Ocean at Cape-Verde region  
1148 during SAMUM-2 and at Puerto-Rico during PRIDE. The complete analysis of aerosol size distribution is  
1149 detailed in Denjean et al. (2015).

#### 1150 **5.1.4 Aerosol chemical composition**

1151 In terms of aerosol chemical properties, an example of averaged mass-size distributions for carbonaceous  
1152 (Elemental and Organic Carbon, EC and OC) species (mass size distribution of inorganic and mineral dust  
1153 aerosols are not shown) obtained at Ersa from a 12-stage cascade impactor (DEKATI system, see Table 1) is  
1154 reported in Figure 16. The aerosol chemical properties obtained from PILS instrument at Ersa are detailed in  
1155 Claeys et al. (2015). As mentioned in Table 1, the measurements were obtained by using a 2-day collection  
1156 period in order to obtain a sufficient aerosol mass on filters for chemical analyses. This system provides the  
1157 speciation of the mass size distribution, including fine and coarse fractions. Such information is very useful  
1158 to derive optical properties using Mie calculations (Mallet et al., 2011) for the main particle types (sulfates,  
1159 ammonium, nitrates, sea-spray, dust, black and organic carbon). This provides crucial information's on key  
1160 radiative properties which are classically used in regional climate models (mass extinction efficiencies, SSA  
1161 and asymmetry parameter). Furthermore, it allows one to assess the spectral dependence of radiative  
1162 properties, which cannot always be estimated from in-situ instrumentation.

1163 Concerning OC (blue curves), observations clearly report a bi-modal mass size distribution with two  
1164 different peaks for the majority of cases. The first (almost constant) peak is found in the  $0.4\text{-}0.5\ \mu\text{m}$  size  
1165 range in diameter and more occasionally a second one occurs in the coarse fraction around  $3\ \mu\text{m}$ .  
1166 Compared to the few available data over the Western Mediterranean, these mass size distributions are  
1167 found to be different from those obtained over Southern France, especially for the accumulation mode.  
1168 Indeed, during the ESCOMPTE experiment in southern France, Mallet et al. (2003) also observed a bi-modal  
1169 size distribution for OC aerosols but with a finer accumulation mode observed in the  $0.1\text{-}0.2\ \mu\text{m}$  size range.

1170 Differences between the two observations is likely due to the proximity of anthropogenic sources during the  
1171 ESCOMPTE experiment compared to the Ersa station, where the possible ageing of carbonaceous particles  
1172 could affect the size of aerosols. On the contrary, the coarse mode of OC appears in the same range of size,  
1173 around 3  $\mu\text{m}$ , for both experiments. Compared to data obtained in the eastern Mediterranean basin, the OC  
1174 mass size distributions are in good agreement with those estimated by Sciare et al. (2003) in Crete during  
1175 the MINOS campaign, with two modes around 0.4  $\mu\text{m}$  and 3  $\mu\text{m}$ . The BC (green curves in Figure 16) mass  
1176 size distribution is also characterized by a bi-modal size distribution, with two modes well correlated with  
1177 the mass size distribution of OC, except for the 16-19 June period (dust episode), where the size of EC fine  
1178 mode is higher ( $\sim 0.5\text{-}0.6 \mu\text{m}$ ) than OC aerosols, the EC coarse mode remaining similar at  $\sim 3 \mu\text{m}$ . This reveals  
1179 a possible external mixing of carbonaceous aerosols for this event.

1180 It should be also noted that the EC concentrations observed at the Ersa station are logically (due at least to  
1181 the altitude of the station and the absence of intense pollution during the SOP-1a, see section 4) lower  
1182 ( $0.39 \mu\text{g}\cdot\text{m}^{-3}$ ) than EC concentrations (PM<sub>2.1</sub>) reported by Eleftheriadis et al. (2006) from the eastern  
1183 Mediterranean during the summer season ( $0.6 \mu\text{g}\cdot\text{m}^{-3}$ ) in July 2000. The same ascertainment is obtained on  
1184 OC concentrations with higher values ( $4.2 \mu\text{g}\cdot\text{m}^{-3}$ ) reported by Eleftheriadis et al. (2006) compared to  
1185 observations at Ersa ( $1.5 \mu\text{g}\cdot\text{m}^{-3}$ ). Concerning the modes of the OC and EC particle mass size distributions,  
1186 the two identified modes detected in Ersa are consistent with those reported by Mallet et al. (2011) at the  
1187 Porquerolles coastal island (southeastern France), who also detected two (fine and coarse) different modes  
1188 of the mass size distributions for EC (0.3-0.4  $\mu\text{m}$  and 4-6  $\mu\text{m}$ ) and OC (0.3  $\mu\text{m}$  and 5-6  $\mu\text{m}$ ) aerosol particles.  
1189 In most cases, we observed at Ersa lower concentrations of EC particles for both modes compared to OC  
1190 aerosols. The mass of OC and BC observed during the SOP-1a, for both modes, are found to be equivalent  
1191 with those observed by Sciare et al. (2003) in Crete in summer 2001. They report mean values of 0.30 and  
1192  $0.15 \mu\text{g m}^{-3}$  for fine OC and BC, respectively. During the MINOS experiment, the mean concentrations for OC  
1193 and BC coarse modes were about 0.1 and  $0.02\text{-}0.03 \mu\text{g m}^{-3}$ , what is also consistent with the observations at  
1194 Ersa. Finally, the mass concentrations obtained for each mode at Ersa are logically lower than those  
1195 obtained during the ESCOMPTE experiment, located much closer to pollution sources. For example, EC and  
1196 OC fine mode concentrations were respectively between 0.8 and  $2.8 \mu\text{g m}^{-3}$  and between 3.1 and  $6.9 \mu\text{g m}^{-3}$

1197 during ESCOMPTE (Mallet et al., 2003). In addition and as discussed in the parts 4.1 and 4.2, the  
1198 meteorological conditions (surface temperature, meteorological synoptic situations) observed during the  
1199 SOP-1a campaign were not favourable to produce large concentration of polluted or smoke aerosols,  
1200 compared to the ESCOMPTE campaign, where AOD as large as 0.3-0.5 (in the visible range) has been  
1201 observed due to important concentration of anthropogenic-polluted particles. It should be noted that, in  
1202 parallel to filter analyses, higher time resolved observations from the PILS systems have been deployed at  
1203 the two stations of Lampedusa and Erba (Claeys et al., in prep.) during the SOP-1a.

1204 In parallel to filters chemical analysis, over 700,000 single particle mass spectra were generated by the A-  
1205 TOFMS instrument during the sampling period (not shown). A *K*-means algorithm ( $K = 80$ ), as described in  
1206 detail by Healy et al. (2010) and Gross et al. (2010) was used to classify aerosol mass spectra into different  
1207 particle classes. More than 40 distinct ATOFMS particle classes were identified and subsequently grouped  
1208 into 8 general categories for clarity. Elemental carbon containing particles dominated the dataset (55% of  
1209 total spectra), followed by K-rich particles (30%) and sea-spray (7%). The remaining particle categories  
1210 include organic carbon (OC)-containing (3%), trimethylamine (TMA)-containing (3%), shipping (2%), Fe-  
1211 containing (0.5%) and Ca-containing (0.3%). EC particles dominated the first third of the sampling period,  
1212 decreased noticeably for approx. 6 days and then dominated the rest of the sampling period again. In  
1213 contrast, K-rich particle (associated with biomass burning and dust) numbers were high only for the latter  
1214 half of the campaign, with a peak on 27-28 June. The profiles of these two particle categories suggest  
1215 transport from regional sources. Sea-spray particle numbers were at their highest during the period where  
1216 EC particles were at their lowest, and were generally low when EC particle numbers were high. OC-  
1217 containing particles were present during the same period K-rich numbers peaked, suggesting an association  
1218 with the transport of biomass burning particles. TMA particles were present in low numbers throughout the  
1219 sampling period, suggesting a less regional source, independent of the air masses influencing EC and sea-  
1220 spray particle occurrence. The same can be said of Fe and Ca-containing particles, likely to be local dust,  
1221 while shipping particle numbers were slightly higher during the first half of the sampling period.

1222 Finally and concerning the aerosol chemical properties, an interesting aspect of the observations deployed  
1223 during the SOP-1a concerns the rBC concentrations obtained from the SP2 instrument onboard the ATR-42.

1224 Despite its importance, studies on rBC were until now limited to surface-based measurements in the  
1225 Mediterranean region. Measurements of vertical distribution of rBC concentrations provide crucial  
1226 information for assessing the rBC radiative effects in the region. Figure 17 shows the vertical distributions of  
1227 rBC mass concentrations measured by the SP2 in the five areas (Granada, Minorca, Lampedusa, South-France  
1228 and Ersa). For the different vertical soundings, rBC mass concentrations ranged between 20 and 690 ng m<sup>-3</sup>  
1229 close to the surface. The surface rBC concentrations were generally less than 200 ng m<sup>-3</sup>, typical for  
1230 continental and regional background sites in the western Mediterranean basin (Ripoll et al., 2015). The  
1231 lowest surface concentration of rBC (~ 20 ng m<sup>-3</sup>) were found in south-France over the open sea with  
1232 almost no local contribution of anthropogenic aerosols. Maxima surface concentrations (~ 690 ng m<sup>-3</sup>)  
1233 were recorded over Granada where frequently heavy traffic emissions are occurring. These observations  
1234 were obtained between 07:15 and 07:45 UTC when the convection was not fully developed, which probably  
1235 did not favour the vertical transport of local emissions over Granada. A prominent feature in vertical profiles  
1236 is the presence of significant concentrations of rBC up to 5-6 km altitude. Therefore the regional transport  
1237 of rBC particles was not only limited to the MBL but occurred also at higher altitude. In most of the  
1238 observed cases, the rBC vertical distribution in the free troposphere reveals a strongly stratified structure  
1239 characterized by either single isolated plumes or more uniform layers. It is worth noting the presence of rBC  
1240 layers above the MBL in the open sea that could be attributed to convective transport from distant sources.  
1241 Only in few observed cases, rBC mass concentration decreased monotonically with increasing altitude, most  
1242 likely due to vertical transport of air masses from surface to higher heights.

## 1243 **5.2 Aerosol optical properties**

### 1244 **5.2.1 In-situ optical properties at the surface**

1245 Figure 17 reports the (daily mean) time-series of nephelometer observations obtained at the surface for the  
1246 Ersa and Lampedusa stations. Daily scattering coefficients (at the three nephelometer wavelengths of 450,  
1247 550 and 700 nm) are reported, as well as the scattering Angström exponent (AE) calculated between 450  
1248 and 700 nm. At 550 nm and at Ersa, the scattering coefficient presents a significant variability during the  
1249 SOP-1a with peaks of about 35-40 Mm<sup>-1</sup> during the dust event (19-20<sup>th</sup> June) transported over the Corsica  
1250 island, associated to low values (15 Mm<sup>-1</sup>) for certain periods of time, as for 21-22 June. The mean



1251 scattering coefficient (at 550 nm) is  $24 \text{ Mm}^{-1}$ . Such scattering coefficient values are comparable to  
1252 observations reported by Vaishya et al. (2012) at the Mace Head station for Atlantic marine air, with  
1253 scattering coefficient (at 550 nm) ranged between 10 and  $25 \text{ Mm}^{-1}$  during the summer period. In terms of  
1254 scattering spectral dependence, the calculated scattering AE is found to be almost constant, with  $AE \sim 1.5$ -2  
1255 and a mean value of 1.71 (indicating that scattering is mostly dominated by fine aerosols) during the SOP-  
1256 1a, except for the 23rd-24th of June. The lowest values ( $AE \sim 0.3$ -0.5) observed during this period are the  
1257 result of a large contribution of coarse sea-spray aerosols (Claeys et al., in prep.) due to moderate ( $5 \text{ m s}^{-1}$ )  
1258 westerly winds (see Figure 8) at the Ersa station, which is also observed from the filter chemical size-  
1259 resolved analyses and detected on the A-TOFMS and VHTDMA data. In parallel, we observe that the dust  
1260 event occurring in Ersa on 18-20 June is not correlated to low scattering AE, revealing a possible  
1261 contribution of fine dust particles only to scattering, result of a possible deposition of the coarse dust  
1262 fraction during transport. The AERONET-derived AE between 440 and 870 nm shows values  $<1$  in the  
1263 afternoon of 19 June and early morning of June 20 suggesting that coarse dust is present in the column. At  
1264 Lampedusa, the daily scattering coefficient (at 550 nm and from PM40 inlet) is between 20 to  $90 \text{ Mm}^{-1}$   
1265 (mean value of  $50 \text{ Mm}^{-1}$ ), which is twice higher than at Ersa (Figure 17). The scattering AE was also highly  
1266 variable, with values ranging between 0.5 and 2.5 (mean value of 1.1). The range of variability of these  
1267 values is due to the observed switch from clean air masses strongly impacted by marine emissions to  
1268 polluted air masses of various ages, including very aged/processed air masses from Northern Europe. A  
1269 single intrusion of mineral dust at the site was recorded on June 9 as a result of a cyclone-type of transport  
1270 from Tunisia (Formenti et al., in prep.).

### 1271 **5.2.2 Remote-sensing observations from the surface**

1272 The optical properties obtained from sun-photometer observations for different AERONET/PHOTONS sites  
1273 are shown in Figure 18. The AERONET/PHOTONS stations have been chosen as located in a domain  
1274 encompassing most of the SOP-1a in-situ and remote sensing observations (Figure 3) and they are  
1275 characterized by different aerosol regimes (see Table 2). The total AOD, Absorbing Aerosol Optical Depth  
1276 (AAOD), AOD for the fine (AODf) and coarse (AODc) modes of the volume size distribution, are indicated (at  
1277 440 nm) for 11 AERONET/PHOTONS stations (Table 2). As mentioned previously, the AOD time-series reveal

1278 moderate values, never reaching values as large as reported during the summer 2012 ChArMEx/TRAQA  
1279 SOP-0 experiment (Rea et al., 2015). During summer 2013, the AOD was generally comprised between 0.1  
1280 and 0.7 (at 440 nm) for most of the AERONET/PHOTONS sites. Over the western basin, the Granada,  
1281 Minorca and Barcelona sites display the largest values during the transport of dust aerosols as detected by  
1282 satellite remote-sensing observations (Figure 6) for the 16 to 20<sup>th</sup> of June. During this dust event, the  
1283 contribution of fine and coarse modes to the total extinction AOD is equivalent. Over the central basin,  
1284 Lampedusa data reveal various peaks. The largest AOD was measured on June 6 (about 0.84 at 440 nm) and  
1285 8 (about 0.63 at 440 nm). Other peaks occurred around June 22 and July 01-02, with corresponding AOD of  
1286 about 0.30-0.40 (at 440 nm), with again an equivalent contribution of each mode of the volume size  
1287 distribution to the AOD. On June 27-28, an AOD peak was also observed over most of the sites and  
1288 corresponded to the transport of an aged smoke plume from the Canadian continent. In this specific case,  
1289 AOD was comprised between 0.25 and 0.50 (at 440 nm). Contrarily to the dust events, the contribution of  
1290 the different modes to AOD was significantly different during this episode. Indeed, as shown in Figure 18,  
1291 AOD was mostly controlled by the fine mode of the volume size distribution. This specific biomass burning  
1292 case is more deeply analysed by Ancellet et al. (submitted) and Chazette et al. (submitted).

1293 We have also used the SSA dataset for making comparisons of its optical parameters between different  
1294 stations. As for the size distributions, we have analysed dataset in four stations, which are Ersa, Lampedusa,  
1295 **Cap d'En Font and Cagliari, which represents, respectively, three of the different surface stations affected by**  
1296 **different aerosol regimes and the aircrafts locations (Cagliari)**. All (daily) SSA retrievals, associated with the  
1297 mean values (at the four wavelengths), are included in the Figure 19. Due to the moderate AOD over the  
1298 period, we used Level 1.5 AERONET/PHOTONS products. In that sense, it should be reminded that  
1299 uncertainties associated to SSA retrievals are important, about  $\pm 0.07$  as reported by Dubovik et al. (2000).

1300 The results indicate an important variability of SSA and its spectral dependence over the different stations.  
1301 At 440 nm, the mean SSA is comprised between 0.91 and 0.98, with the lowest (resp. highest) value  
1302 observed in Lampedusa (resp. Ersa). Hence, aerosols appear as **mainly** scattering at Ersa and moderately  
1303 absorbing at Lampedusa. The contribution of the coarse mode to the total size distribution could explain  
1304 the lower values observed in Lampedusa at this wavelength. Indeed, the radiative effects and optical

1305 properties of dust are strongly dependent on the coarse mode size distribution as the larger particles  
1306 appreciably decrease the SSA (McConnell et al., 2010; Otto et al., 2009). More recently and during the  
1307 FENNEC experiment, Ryder et al. (2013) have calculated SSA (at 550 nm) for dust aerosols using the full  
1308 range of sizes measured, indicating that dust SSA was highly sensitive to effective diameter: size  
1309 distributions with the largest effective diameters produced the lowest SSA values. The presence of a coarse  
1310 mode could also be due to the presence of marine aerosols within the MBL in Lampedusa. Observations for  
1311 the Cap d'En Font and Cagliari stations reveal an intermediate value (0.93 at 440 nm) in Cagliari, which is  
1312 also more affected by mineral dust aerosols (Figure 14). We can also observe very low values in Cagliari (for  
1313 the period of 14 to 17 June) that could be due to local pollution. Anyway, it should be remained that those  
1314 retrievals have been performed under low AOD ( $\sim 0.10$  at 440 nm) conditions and are associated to large  
1315 uncertainties. One important point concerns the changes in the SSA spectral signature between Ersa  
1316 (negative tendency between 440 nm to 1020 nm) and Lampedusa (positive) stations. This observation is  
1317 consistent with AERONET/PHOTONS data analysed for a long-time period over the Mediterranean by Mallet  
1318 et al. (2013), who report different spectral variations in SSA, following the aerosol regime (dusty and/or  
1319 polluted particles). One of the main conclusions here is that aerosols are found to be moderately absorbing  
1320 during the SOP-1a period, what is consistent with in-situ observations performed onboard the ATR-42  
1321 aircraft and summarized by Denjean et al. (2015).

### 1322 **5.2.3 ATR-42 and F-20 aircraft observations**

1323 In parallel to surface observations, an example of the vertical profiles of aerosol optical properties obtained  
1324 from ATR-42 measurements is shown Figure 20 that corresponds to the flight 35-36 over the station of  
1325 Lampedusa for the 22<sup>nd</sup> of June (see also Denjean et al., 2015 and Nicolas et al., in prep.). Scattering  
1326 coefficients (in  $\text{Mm}^{-1}$ ) are plotted at 450, 550 and 700 nm (left) versus altitude (in meter). Completely  
1327 different behaviours in the scattering spectral dependence as a function of altitude were observed. Two  
1328 different aerosol plumes characterized by a significant spectral dependence (typically of submicronic  
1329 polluted, smoke or fine marine aerosols) are observed around 1000 and 2000-2500 m. Above 3000 m, the  
1330 spectral dependence is clearly reduced, corresponding to air masses with high mineral dust concentrations.  
1331 For this upper aerosol layer, the scattering coefficient increases up to  $60 \text{ Mm}^{-1}$ . The analysis of the extinction

1332 (at 530 nm) vertical profiles obtained from the CAPS system (Table 3) reveals an excellent agreement with  
1333 nephelometer data showing the peaks of extinction at similar altitudes (see Denjean et al., 2015), with  
1334 maxima ( $\sim 90 \text{ Mm}^{-1}$ ) logically observed within the dust plumes (4000-5000 m). Number concentrations, as  
1335 well as volume size distributions, highlight the significant atmospheric loading by particles with diameter  
1336 higher than  $1 \mu\text{m}$  above 3000 m (maxima of  $5000 \# \text{ cm}^{-3}$ ). For this atmospheric layer, the volume size  
1337 distribution is characterized by a coarse mode, around 6-8  $\mu\text{m}$ . As previously mentioned, vertical profiles of  
1338 optical properties in terms of AE, SSA, asymmetry parameters as well as their spectral dependence are  
1339 presented and discussed in details by Denjean et al. (2015) and Nicolas et al. (in prep.). The airborne SW  
1340 and LW radiation measurements and the comparison with radiative transfer model simulations at  
1341 Lampedusa are presented by Meloni et al. (in prep.).

## 1342 **5.3 Aerosol vertical structure**

### 1343 **5.3.1 Lidar surface observations**

1344 Although deeply analysed in other dedicated papers, some examples of the aerosol vertical profiles are  
1345 presented here. First and over the Minorca station, surface lidar observations in Figure 21a were obtained  
1346 during June 16 and 17, that corresponds to the first event of transported mineral dust over the western  
1347 basin. They show a dust aerosol layer located between 1.5 and 5 km, with a maximum of aerosol extinction  
1348 (at 355 nm) around  $0.10 \text{ km}^{-1}$  on 16<sup>th</sup> of June between 12:00 and 14:00 Local Time (LT). Comparisons of  
1349 retrieved AOD with the lidar system is shown to be very consistent with sun-photometer observations for  
1350 these two days (Figure 21a, top), with moderate AOD (at 355 nm) ranging between 0.2 and 0.4 at  
1351 maximum. During 17 June, the dust layer is less intense and the aerosol extinction above 1.5 km decreases.  
1352 After 14:00 LT, Figure 21a clearly shows that most of the contribution to AOD is due to the MBL over the  
1353 Minorca station. At Ersa (Figure 21b), the dust event reached the northern tip of Corsica on 19 June. A deep  
1354 depolarizing aerosol layer was observed at altitudes between 3 and 6 km. In the night of the 20<sup>th</sup>, the  
1355 particulate depolarization ratio is close to 18% and the lidar ratio within the dust layer was estimated at 46  
1356 sr. The extinction coefficient remains moderate within the dust layer  $\sim 0.05 \text{ km}^{-1}$  (Figure 21b) between 4 and  
1357 6 km. It should be noted that a complete analysis of lidar observations series obtained over the cape Corsica  
1358 site is reported in Leon et al. (2015). The dust event vertical distribution is further analysed by means of the

1359 EARLINET lidar stations in Sicard et al. (2015) and by means of the EARLINET and ChArMEx lidar stations in  
1360 Barragan et al. (in prep.).

1361 In addition to Minorca and Ersa, two lidars were also operated at Lampedusa during the SOP-1a and  
1362 provided vertical profiles of aerosol backscattering and depolarization. The ENEA/University of Rome lidar  
1363 measures the aerosol backscattering at 532 and 1064 nm, plus the depolarization at 532 nm. This system  
1364 was operated throughout the campaign, although not continuously. The lidar data retrieval is described by  
1365 Di Iorio et al. (2009), and uses sun-photometer AOD observations to constrain the determination of the  
1366 aerosol backscattering profile. Figure 22a shows the evolution of the vertical profile of the aerosol  
1367 backscattering coefficient at 1064 nm on 3 July 2013 at Lampedusa. At low altitudes the air masses reaching  
1368 Lampedusa originated from the North. Air masses above 2 km conversely came from a southwesterly  
1369 direction crossing North Algeria and Tunisia, and carried desert dust. Elevated backscattering attributed to  
1370 dust was observed up to 5 km altitude, and a steep transition in the backscattering coefficient occurred at  
1371 this altitude throughout the day. Figure 22b shows the backscattering coefficient profile at 532 and 1064  
1372 nm, and the depolarization ratio measured at 15:45 UT by the ENEA/University of Rome and the LISA lidars.  
1373 Evidently, the backscattering coefficient above 2 km shows small wavelength dependence, and elevated  
1374 values of the depolarization ratio, as expected from large irregular desert dust particles (Sassen, 1999). The  
1375 influence of large particles is smaller below 2 km, where the backscattering coefficient shows some  
1376 dependency on wavelength, and the depolarization ratio decreases. The significant role played by the large  
1377 particles on 3 July is also confirmed by the aerosol size distribution and optical properties (i.e., values and  
1378 spectral dependency of the refractive index and single scattering albedo) retrieved from the AERONET  
1379 observations at Lampedusa. The average AOD (at 500 nm) was 0.28, and the AE (calculated between 440  
1380 and 870 nm) was 0.39, as expected for cases with a large contribution of desert dust. The retrieved  
1381 columnar volume size distributions on the two days show that the mode with a median radius around 2  $\mu\text{m}$   
1382 is 2-3 times more intense on 3 July than on 17 June.

1383 Finally, nighttime measurements at Potenza (Italy) on 21 June starting at 23:40 UT, which coincides with the  
1384 arrival of the Saharan dust event over southern Italy, indicate a clear signature of Saharan dust in the  
1385 tropospheric layer between 1.8 and 3.9 km, an extinction-related AE value of approximately 0 is measured

1386 between roughly 2 and 3 km and a quite constant LR around 50 sr at both 355 and 532 nm (not shown, see  
1387 Sicard et al., 2015a; Barragan et al., in prep.).

### 1388 **5.3.2 LNG observations**

1389 An example of LNG (Lidar Nouvelle Génération) observations onboard the F-20 aircraft is presented in the  
1390 Figure 23 for the 19<sup>th</sup> of June that corresponds to a flight (12:46 to 13:26 TU) from Sardinia to the Gulf of  
1391 Genoa. The aerosol extinction (in  $\text{km}^{-1}$  and at 532 nm) is represented in function of latitude during this flight  
1392 as well as the associated AOD with a high temporal and spatial frequency. One can observe the significant  
1393 North-South gradient during this dust event with low-values of AOD (around 0.1 at 532 nm) for latitude of  
1394 44°N and moderate-high AOD (0.40 to 0.55) for latitudes lower than 42-43°N. In terms of vertical structure,  
1395 this increase of AOD is due to an upper dust layer (around 5 to 6 km) characterized by an aerosol extinction  
1396 of about  $0.1 \text{ km}^{-1}$ . This intense dust layer transported over most of the investigated region (40.5°N-43.5°N) is  
1397 associated with a second more diluted aerosol layer observed between 3 and 4 km with LNG. Another  
1398 interesting aspect is the variability of aerosol extinction detected in the marine boundary layer showing  
1399 large differences throughout the F-20 transect. The aerosol extinction is found to be significant around 41°N  
1400 to 41.5°N that could be due to sea-spray particles generated in south Corsica Island due to the local  
1401 acceleration of the wind occurring between the Corsica and Sardinia islands (not shown). This increase of  
1402 the aerosol loading in the MBL associated with dust aerosol transported to higher altitudes results in an  
1403 increase of total AOD at these latitudes. Such aircraft lidar data will be useful for testing the different  
1404 modeling systems used for the SOP-1a experiment and more specifically their ability to reproduce complex  
1405 vertical aerosol structures over the western Mediterranean. Additional observations of the aerosol  
1406 extinction vertical profile obtained over different surface-stations from the passive remote-sensing PLASMA  
1407 instrument onboard the ATR-42 aircraft are presented in Torres et al. (in prep.).

### 1408 **5.3.3 Sounding balloon observations**

1409 Figure 24 shows an example of the vertical profile of the aerosol particle size distribution obtained on June  
1410 19 near the end of the dust episode that started on 16 June over Minorca. The daytime average AOD  
1411 geographical distribution derived from MSG/SEVIRI is shown in Figure 6. The vertical profile clearly shows  
1412 the presence of the dust layer between about 2.5 and 4.5 km in altitude, in agreement with coincident lidar

1413 continuous observations at Minorca that show the more limited vertical extent of dust compared to  
1414 previous days and the end of the episode on June 19 in this area (Chazette et al., submitted). It should be  
1415 noted that sounding balloons appear to under-detect very large particles within dust layers compared to the  
1416 drifting balloons. This can be due isokinetic sampling differences between sounding systems that have a  
1417 vertical velocity of several  $\text{m s}^{-1}$  and systems drifting at a constant air density that are quasi-Lagrangian.  
1418 However coincident AERONET and LOAC vertically integrated particle size distribution in the range 0.1-  
1419  $30 \mu\text{m}$  in diameter performed on June 16 and 17 were found quite comparable. In the marine atmospheric  
1420 boundary layer, the LOAC speciation index (Renard et al., 2015a) indicates hydrated particles. In the free  
1421 troposphere above dust, the concentration of particles rapidly decreased by one order of magnitude and  
1422 particles were mainly of submicronic size with sometimes a significant number of particles in the 1.1-3  $\mu\text{m}$   
1423 channel.

## 1424 **5.4 Local Direct Radiative Forcing**

### 1425 **5.4.1 Estimates using in-situ aircraft data and radiative transfer codes over the two super-sites**

1426 Before investigating the possible climatic effect of aerosols on the Mediterranean climate, an important  
1427 preliminary step is the calculation of the direct radiative forcing (DRF) exerted by aerosols. This can be  
1428 addressed by using in-situ (physical-optical properties) and remote-sensing (vertical profiles) observations  
1429 of aerosols as input to radiative transfer models. Simulated SW and LW radiative fluxes can be evaluated  
1430 using observed radiative fluxes both at the surface and onboard the two aircraft. The combination of in-situ  
1431 and remote sensing measurements provide a complete and unique dataset for conducting such 1-D  
1432 radiative transfer simulations. To this end, vertical profiles from the ATR-42 were combined with surface  
1433 observations from the two (Ersa and Lampedusa) stations to calculate the SW DRF of different aerosol  
1434 events (Nicolas et al., in prep.; Meloni et al., in prep.). Over the western basin and for the first period of the  
1435 campaign (16 to 20 June), different calculations, with the GAME radiative transfer model (Dubuisson et al.,  
1436 2004), of the downward and upward SW cloud-free irradiances have been performed by Nicolas et al. (in  
1437 prep.) for 6 vertical profiles over Granada, Minorca and Corsica islands. Briefly, the methodology is based on  
1438 extinction, SSA and phase function vertical profiles (and their spectral dependence), obtained from  
1439 observations and Mie calculations, and associated with atmospheric thermodynamic properties. They

1440 clearly show a significant change in surface radiative fluxes with a well-known decrease (dimming effect) of  
1441 downward radiations due to scattering and absorption of solar radiation by dust aerosols. Inter-comparisons  
1442 between observed/simulated downward and upward clear-sky SW fluxes show a good agreement during  
1443 the ascent and descent profiles. At TOA, Nicolas et al. (in prep.) reported a direct (instantaneous at noon)  
1444 SW DRF ranged between  $-4$  and  $-33 \text{ W m}^{-2}$ , revealing a cooling effect due to dust particles. These  
1445 simulations also indicate that the decrease in surface radiation is not completely compensated by the TOA  
1446 cooling, meaning that aerosols exerted a positive atmospheric forcing due to their ability to absorb solar  
1447 radiations.

1448 Similar calculations (not shown) have been done over the Lampedusa reference-site by Meloni et al. (in  
1449 prep.) by using a similar method based on lidar, sun-photometer, in-situ surface, ATR-42 and F-20  
1450 observations and the MODTRAN 5.3 radiative transfer code. Meloni et al. (in prep.) estimate both the SW  
1451 and the LW aerosol radiative forcing profiles and the balance between the two spectral components (SW  
1452 and LW). During the descent towards Lampedusa airport on 22 June, the instantaneous ( $12.5^\circ$  solar zenith  
1453 angle and aerosol optical depth at 500 nm of 0.32) SW cooling at the surface ( $-44 \text{ W m}^{-2}$ ) is reduced by  
1454 about 10% due to infrared emission. The dust SW radiative forcing at TOA is  $-6 \text{ W m}^{-2}$ . These values are  
1455 obtained using the AERONET aerosol size distribution and different aerosol refractive indices in the SW and  
1456 in the LW spectral regions. The LW contribution at the surface is lower than the values reported in previous  
1457 studies (di Sarra et al., 2011; Meloni et al., 2015), partially due to the different solar zenith angle and to the  
1458 presence of mixed aerosol below the dust layer down to the surface.

#### 1459 **5.4.2 Estimates of instantaneous clear-sky SW DRF using AERONET/PHOTONS observations**

1460 As reported previously, AERONET/PHOTONS network provides, in addition to microphysical and optical  
1461 aerosol properties, an estimate of the local (instantaneous) clear-sky direct radiative forcing at any  
1462 AERONET/PHOTONS location as an operational product of the network. The method of derivation is  
1463 described in Garcia et al. (2012). As mentioned above, the extremely good regional coverage of  
1464 AERONET/PHOTONS sun-photometer instruments during the SOP-1a allow a complementary estimate of  
1465 the local radiative (clear-sky) forcing to those derived by Meloni et al. (in prep.) and Nicolas et al. (in prep.).  
1466 The Figure 25 indicated the averaged of all instantaneous (clear-sky) DRF (in  $\text{W m}^{-2}$ ) estimated during a day



1467 for both AERONET/PHOTONS station. Estimates are reported at the surface (bottom left), at TOA (bottom  
1468 right) and within the total atmosphere (down). Averaged values of the DRF are also indicated in the Figure  
1469 25. As mentioned above, sun-photometers retrievals demonstrate a significant DRF during the SOP-1a  
1470 experiment. As an example and at the surface, the mean forcing is comprised between  $-15 \text{ W m}^{-2}$   
1471 (Barcelona, not affected by dust transport) and  $-35 \text{ W m}^{-2}$  in Burjassot. Such values are consistent with  
1472 independent 1-D estimates reported by Nicolas et al. (in prep.) and Meloni et al. (in prep.).  
1473 AERONET/PHOTONS data also reveal a negative DRF at TOA over most of sites, meaning that aerosols exert  
1474 in majority a cooling effect at TOA, with values around  $\sim -6$  to  $-12 \text{ W m}^{-2}$ . These negative values are also due  
1475 to the fact that most of AERONET/PHOTONS stations are located over islands, which are characterized by  
1476 low surface albedo. Logically and due to the moderate values of aerosol absorption observed during the  
1477 SOP-1a (Denjean et al., this special issue), a positive atmospheric forcing is observed with mean values from  
1478  $+7$  to  $+30 \text{ W m}^{-2}$  (with maxima in Burjassot), that could affect the vertical profiles of temperature and  
1479 relative humidity as shown recently by Nabat et al. (2015a).

#### 1480 **5.4.3 Estimates using in-situ radiative flux observations**

1481 As shown by di Sarra et al. (2011), an estimate of the aerosol radiative forcing can be obtained by comparing  
1482 irradiance measurements made during days characterized by different aerosol loads. In particular, the  
1483 identification of a cloud-free day with low aerosol amounts is important to provide a reference for pristine  
1484 conditions. During the SOP-1a, 17 June at Lampedusa displayed a very low aerosol optical depth (daily  
1485 average of 0.064 at 500 nm) and cloud-free conditions throughout the day, and was identified as the  
1486 reference day for pristine conditions. July 3, conversely, was one of the days characterized by the presence  
1487 of desert dust, with moderate values of the AOD (0.28). As shown in figure 22a, dust was present above 2  
1488 km altitude and there were no major changes in the aerosol vertical distribution during the day, as it also  
1489 appears from the limited daily variability of the AOD (daily standard deviation of the AOD at 500 nm of  
1490 0.015). Cloud-free conditions were present throughout the day.

1491 Figure 27 displays the downward solar irradiance measured on 3 July, compared with the one measured on  
1492 the pristine reference day (17 June). The irradiance measurements were corrected for the radiometer  
1493 thermal offset as discussed by Di Biagio et al. (2009). The sharp narrow peak occurring on 17 June around

1494 6:30 was related to a small isolated cloud, and these data were discarded from the analysis. The differences  
1495 between the downward irradiances measured on these two days were calculated as a function of the solar  
1496 zenith angle; these differences are due to the effect of aerosol and, to a smaller extent, column water  
1497 vapour. The effect of water vapour was estimated by means of a radiative transfer model (see e.g., di Sarra  
1498 et al., 2011), and the remaining difference was integrated over 24 hours to obtain the daily average effect,  
1499  $\Delta I$ , on the downward solar irradiance. The daily aerosol radiative forcing RF can be derived as:

$$1500 \text{ RF}=\Delta I(1-A)$$

1501 where  $\Delta I$  is the difference between the two curves of Figure 27 integrated over 24 hours, and A is the  
1502 surface albedo. For a surface albedo of 0.07 (di Sarra et al., 2011), the estimated surface RF is  $-14.8 \text{ W m}^{-2}$ .

1503 The radiative forcing efficiency (RFE), which is the radiative forcing produced by a unit AOD, was calculated  
1504 as:

$$1505 \text{ RFE}=\text{RF}/(\text{AOD}_2-\text{AOD}_1)$$

1506 where  $\text{AOD}_1$  and  $\text{AOD}_2$  are the measured daily average aerosol optical depth on 17 June and 3 July,  
1507 respectively. The estimated RFE is  $-67.4 \text{ W m}^{-2}$ . Di Biagio et al. (2010), based on a multi-year dataset at  
1508 Lampedusa, derived a similar value for desert dust ( $-68.9 \text{ W m}^{-2}$ ) at the equinox; di Sarra et al. (2010), for an  
1509 intense desert dust event occurring in March 2010 found values between  $-70$  and  $-85 \text{ W m}^{-2}$ . For a desert  
1510 dust event associated with the propagation of a gravity wave, with values of AOD similar to those of 3 July,  
1511 di Sarra et al. (2013) derived an RFE equal to  $-79 \text{ W m}^{-2}$ . Valenzuela et al. (2012) determined REF for  
1512 Saharan dust episodes over the western Mediterranean with different origins, showing values in the range  
1513 from  $-74 \text{ W m}^{-2}$  (for air masses coming from North Morocco) to  $-65 \text{ W m}^{-2}$  (for air masses coming from  
1514 Algeria and Tunisia). Values of the dust RFE at the surface in the same range were obtained by Derimian et  
1515 al. (2006), although they were derived in different conditions for which the influence of surface albedo  
1516 should be taken into account.

1517 The downward LW irradiance measured on 3 July was higher than on 17 June by  $23 \text{ W m}^{-2}$ . Most of this  
1518 effect is due to differences in the water vapour column amount (about 1 cm difference between the two  
1519 days, with larger values on 3 July). Once the water vapour contribution was subtracted by means of  
1520 radiative transfer calculations, we found a net positive effect induced by the aerosol of about  $+5.5 \text{ W m}^{-2}$ .

1521 This is, on the daily timescale, about 35% of the SW effect. The resulting aerosol RFE in the LW spectral  
 1522 range is  $+25.5 \text{ W m}^{-2}$ , in agreement with previous results by di Sarra et al. (2011) who found values between  
 1523  $+25.9$  and  $+27.9 \text{ W m}^{-2}$ , or Anton et al. (2014) who reported RFE values around  $+20 \text{ W m}^{-2}$  (in reference to  
 1524 AOD at 675 nm).

#### 1525 **5.4.4 Estimations of the SW and LW radiative heating rate along the vertical**

1526 One important original aspects of this study concerns the estimates of the vertical profiles of SW and LW  
 1527 radiative heating rate. To our knowledge, all the referenced estimates of this important parameter, which  
 1528 controls for a part the semi-direct radiative effect of aerosols, have been conducted using remote-sensing  
 1529 techniques or in-situ observations of aerosol optical properties, coupled with radiative transfer modeling.  
 1530 Here, we propose a first estimate of the SW and LW heating rate derived directly from upward and  
 1531 downward (SW and LW) radiative fluxes obtained on-board the ATR-42 aircraft. Because of the nature  
 1532 mainly diffuse of longwave upward and downward irradiances (irradiances in thermal infrared), and of the  
 1533 upward shortwave irradiance (irradiance in solar domain), in first approximation, no correction due to the  
 1534 altitude of the aircraft will be applied to these measurements. Only shortwave downward irradiances will  
 1535 be corrected. Three kinds of corrections are applied:

- 1536 - Correction of the aircraft attitude (unavoidable movements due to the aircraft pitch and roll)
- 1537 - Correction of cosine response of the pyranometer
- 1538 - Correction due to the non-horizontal position of the sensor when a stabilized leg (ie. determination  
 1539 of offsets on roll and pitch)

1540 Let  $\theta_m$  the angle between the sun direction and the normal to the pyranometer sensor (depending on pitch,  
 1541 roll and aircraft heading given by the inertial navigation system), and  $\theta_s$  the solar zenith angle, the attitude  
 1542 correction coefficient is:

$$1543 \quad X_d^n = \frac{\cos \theta_m}{\cos \theta_s}$$

1544 Finally, we obtain the global (direct plus diffuse) downward irradiance, for the solar zenith angle  $\theta_s$ :

$$1545 \quad E_{SW}^\downarrow(\theta_s) = \frac{E_{SW}^{m\downarrow}(\theta_m)}{(X_d^n [1 - c(\theta_s)] - D) f(\theta_s) + D}.$$

1546 In this equation,  $E_{SW}^{m\downarrow}(\theta_m)$  is the measured global irradiance,  $c(\theta_s)$  is the cosine response of the  
1547 pyranometer,  $D = 2 \int_0^1 [1 - C(\theta_m)] \mu d\mu$  and  $f(\theta_s)$  is the part of direct downward irradiance in the global  
1548 (estimation obtained from radiative transfer code). Taking into account these corrections, Figure 28a shows  
1549 downward ( $E_{SW}^{Dwn}$ ), upward ( $E_{SW}^{Up}$ ), and net ( $E_{SW}^{Net}$ ) shortwave irradiances obtained from measurements  
1550 performed onboard ATR-42 aircraft on 22 June between 10.35 and 11.30 TU. Irradiances are reduced to the  
1551 mean solar zenith angle  $\theta_s = 29.7^\circ$ . Similarly, Figure 28b shows corresponding measurements of  
1552 downward ( $E_{LW}^{Dwn}$ ), upward ( $E_{LW}^{Up}$ ), and net ( $E_{LW}^{Net}$ ) longwave irradiances. Total net irradiances are then  
1553 determined versus the aircraft altitude for the mean air mass factor of the considered studied flight phase.  
1554 Radiative cooling/heating rate is finally derived and shown in the figure 28c, in which the longwave (LW)  
1555 and shortwave (SW) parts are distinguished.

1556 Concerning the SW heating rate vertical profiles (Figure 28c), one can observe the significant increase of  
1557 the calculated instantaneous SW heating rate in the two different aerosol layers detected for this case  
1558 (Figure 21), especially above 4 km, that corresponds to the maximum of extinction coefficient (up to 100  
1559  $Mm^{-1}$ ) due to the presence of mineral dust. For this specific layer, the values of SW heating rate peak at 4-5  
1560  $^\circ K$  per day for a solar angle of  $29.7^\circ$ . We can also observe a similar tendency in the second aerosol layer,  
1561 located between 1.5 and 3 km (see Figure 21). Concerning the LW heating rate, the figure 28c indicates  
1562 instantaneous values ranging between -2 to -4  $^\circ K$  per day, which is also consistent with the well known  
1563 cooling effect of mineral dust in the longwave spectrum (Mallet et al., 2006, Zhu et al., 2007). As shown in  
1564 Figure 28c, the net heating rate is dominated by the SW heating (the maximum LW cooling is less than 60%  
1565 of the SW heating), which leads to net SW radiative heating ranging between +0.5 and +2 K per day inside  
1566 the dust layer above the MBL. Such unique and original database of SW and LW radiative heating obtained  
1567 over the western Mediterranean should be now used to evaluate the ability of the different models  
1568 involved in the ChArMEx/ADRIMED project (see the following section 6) to simulate this important radiative  
1569 property for the different identified dust cases.

## 1570 6. Overview of Modeling Activities

1571 Several models are used to analyze the SOP-1a period: the meso-scale meteorological COSMO-MUSCAT  
1572 model, the chemistry transport model (CTM) CHIMERE model, and two regional climate (RegCM and CNRM-  
1573 RCSM) models. These models differ in terms of horizontal and vertical resolutions, physical  
1574 parameterizations, aerosol-chemical schemes and are able to deliver complementary information to  
1575 address key scientific questions of the ChArMEx/ADRIMED experiment. Their main characteristics are  
1576 summarized in Table 8.

### 1577 **6.1 COSMO-MUSCAT model**

1578 The parallelized multi-scale regional model system COSMO-MUSCAT (Wolke et al., 2012) consists of the non-  
1579 hydrostatic atmosphere model COSMO (Consortium for Small-scale Modelling) that is on-line coupled to the  
1580 3-D chemistry tracer transport model MUSCAT (MULTiScale Chemistry Aerosol Transport Model). The  
1581 atmospheric dust cycle consisting of the emission, transport and deposition of dust particles is simulated  
1582 within MUSCAT using meteorological and hydrological fields from COSMO. Dust emission is calculated using  
1583 the emission scheme by Tegen et al. (2002) and depends on local surface wind friction velocities, surface  
1584 roughness length, soil texture and soil moisture. Calculated dust emission fluxes depend on particle  
1585 diameter for individual size classes that are assumed to be log-normally distributed. Following Marticorena  
1586 and Bergametti (1995), dust emission is considered as threshold function of local friction velocities and thus  
1587 initial dust emission is computed as a function of soil particle size distribution. Dust emission is limited to  
1588 regions where active dust sources have been identified during 2006-2009 from MSG SEVIRI observations  
1589 (Schepanski et al., 2007). The advection of dust particles is described by a third order upstream scheme;  
1590 dust particles are transported as passive tracer in five independent size classes with limiting radius at  
1591  $0.1\mu\text{m}$ ,  $0.3\mu\text{m}$ ,  $0.9\mu\text{m}$ ,  $2.6\mu\text{m}$ ,  $8\mu\text{m}$ , and  $24\mu\text{m}$ . The removal of dust particles from the atmosphere is  
1592 described by dry and wet deposition taking particle size, particle density, and atmospheric conditions into  
1593 account. Here, the simulations of the atmospheric dust cycle are performed at a 28 km horizontal grid and  
1594 40 vertical layers, covering North African dust sources, the eastern North Atlantic, the Mediterranean basin  
1595 and Europe.

### 1596 **6.2 The CHIMERE chemistry-transport model**

1597 CHIMERE is a chemistry-transport model able to simulate concentrations fields of gaseous and aerosols

1598 species at a regional scale. The model is off-line and thus needs pre-calculated meteorological fields to run.  
1599 In this study, we used the version fully described in Menut et al. (2013), forced by the WRF meso-scale  
1600 model. The horizontal domain is the same as the one of WRF, and, for the vertical grid, the 28 vertical levels  
1601 of WRF are projected on the 20 levels of the CHIMERE mesh. The gaseous species are calculated using the  
1602 MELCHIOR 2 scheme and the aerosols using the scheme developed by Bessagnet et al. (2004). This module  
1603 takes into account species such as sulfate, nitrate, ammonium, primary organic (OC) and black carbon (BC),  
1604 secondary organic aerosols (SOA), sea-spray, mineral dust, and water. These aerosols are represented using  
1605 ten bins, from 40 nm to 20  $\mu\text{m}$ , in diameter. The life cycle of these aerosols is completely represented with  
1606 nucleation of sulfuric acid, coagulation, adsorption/desorption, wet and dry deposition and scavenging. This  
1607 scavenging is both represented by coagulation with cloud droplets and precipitation. The formation of SOA  
1608 is also taken into account. The anthropogenic emissions are estimated using the same methodology as the  
1609 one described in Menut et al. (2013) but with the HTAP masses as input data. These masses were prepared  
1610 by the EDGAR Team, using inventories based on MICS-Asia, EPA-US/Canada and TNO databases  
1611 ([http://edgar.jrc.ec.europa.eu/htap\\_v2](http://edgar.jrc.ec.europa.eu/htap_v2)). Biogenic emissions are calculated using the MEGAN emissions  
1612 scheme (Guenther et al., 2006), which provides fluxes of isoprene, terpene and pinenes. In addition to this  
1613 2013 version, several processes were improved and added in the framework of this study. First, mineral dust  
1614 emissions are now calculated using new soil and surface databases, as described in Menut et al. (2013).  
1615 Second, chemical species emissions fluxes produced by vegetation fires are estimated using the new high  
1616 resolution fire model presented in Turquety et al. (2014). Finally, the photolysis rates are explicitly  
1617 calculated using the FastJ radiation module (Mailler et al., 2015).

### 1618 **6.3 The RegCM Regional Climate model**

1619 The RegCM system is a community model designed for use by a varied community composed of scientists in  
1620 industrialized countries as well as developing nations. It is supported through the Regional Climate Network,  
1621 or RegCNET, a widespread network of scientists coordinated by the Earth System Physics section of the  
1622 Abdus Salam International Centre for the Theoretical Physics (ICTP, Giorgi et al., 2012). RegCM is a  
1623 hydrostatic, compressible, sigma-p vertical coordinate model. As a limited area model, RegCM requires  
1624 initial and boundary conditions that can be provided both by NCEP or ECMWF analyses. The horizontal

1625 resolution used need to be higher than 10 km, due to the hydrostatic dynamic core of the model, associated  
1626 with 23 vertical levels. A simplified aerosol scheme specifically designed for application to long-term climate  
1627 simulations has been incrementally developed within the RegCM system. Solmon et al. (2006, 2008) first  
1628 implemented a first-generation aerosol model including sulfates, organic carbon, and black carbon. Zakey et  
1629 al. (2006) then added a 4-bin desert dust module, and Zakey et al. (2008) implemented a 2-bin sea-spray  
1630 scheme. In RegCM, the dust emission scheme accounts for sub-grid emissions by different types of soil. The  
1631 dust emission size distribution can now also be treated according to Kok (2011). When all aerosols are  
1632 simulated, 12 additional prognostic equations are solved in RegCM, including transport by resolvable scale  
1633 winds, turbulence and deep convection, sources, and wet and dry removal processes. In RegCM, the  
1634 natural/anthropogenic aerosols are radiatively interactive both in the solar and infrared regions and so are  
1635 able to feedback on the meteorological fields.

#### 1636 **6.4 The CNRM-RCSM Regional Climate model**

1637 The fully coupled RCSM (Regional Climate System Model), which is developed at CNRM has been also used  
1638 within the ChArMEx/ADRIMED project. This model includes the regional climate atmospheric model  
1639 ALADIN-Climate (Déqué and Somot 2008), the regional ocean model NEMOMED8 (Beuvier et al., 2010) and  
1640 the land-surface model ISBA (Noilhan and Mahfouf, 1996). We used here the version described in Nabat et  
1641 al. (2015b) with a 50 km horizontal resolution. ALADIN-Climate includes the Fouquart and Morcrette  
1642 radiation scheme based on the ECMWF model incorporating effects of greenhouse gases as well as direct  
1643 effects of aerosols. The ocean model NEMOMED8 is the regional eddy-permitting version of the NEMOV2.3  
1644 ocean model that covers the Mediterranean Sea. Concerning the aerosol phase, the model ALADIN-Climate  
1645 incorporates a radiative scheme to take into account the direct and semi-direct effects of five aerosol types  
1646 (sea-spray, desert dust, sulfates, black and organic carbon aerosols) through either AOD climatologies or a  
1647 prognostic aerosol scheme (Nabat et al., 2013, 2015b). On the one hand, Nabat et al. (2013) have proposed  
1648 a new AOD monthly climatology over the period 2003-2009, based on a combination of satellite-derived  
1649 and model-simulated products. The objective is having the best estimation of the atmospheric aerosol  
1650 content for these five most relevant aerosol species. On the other hand, a prognostic aerosol scheme has  
1651 been recently implemented in ALADIN-Climate, and has shown its ability to reproduce the main patterns of

1652 the aerosol variability over the Mediterranean (Nabat et al., 2015b).  
1653 Using CNRM-RCSM with the new AOD monthly climatology over the period 2003-2009 (Nabat et al., 2013),  
1654 Nabat et al. (2015a) have notably highlighted the response of the Mediterranean Sea Surface Temperature  
1655 (SST) to the aerosol direct and semi-direct radiative forcing. Figure 29a presents the annual average  
1656 difference in SST over the period 2003-2009 between a simulation ensemble including aerosols and a  
1657 second one without any aerosol. Aerosols are found to induce an average decrease in SST by 0.5°C, because  
1658 of the scattering and absorption of incident radiation. As a consequence, the latent heat loss is also reduced  
1659 by aerosols (Figure 29b), as well as precipitation (Figure 29c). This result also underlines the importance of  
1660 taking into account the ocean-atmosphere coupling in regional aerosol-climate studies over the  
1661 Mediterranean.

## 1662 **6.5 SOP-1a multi-model aerosol simulations**

### 1663 **6.5.1 Aerosol Optical Depth**

1664 Figure 30 reports the AOD (in the visible range) simulated for the SOP-1a period and for the COSMO-M (550  
1665 nm), RegCM (between 440 and 670 nm), CNRM-RCSM (550 nm) and CHIMERE (500 nm) models. Except the  
1666 CTM-CHIMERE model which includes all the secondary species (SOA and inorganic), the others have  
1667 different aerosols schemes and take into account both natural (COSMO-M) or natural plus a part of  
1668 anthropogenic aerosols as described in Table 7. The configurations used for each models are listed in Table  
1669 7. One can observe the large variability of AOD simulated by models over the Mediterranean region with  
1670 highest values clearly simulated by the COSMO-M (AOD ~1-1.5 in the visible wavelengths) over the  
1671 Northern Africa region. The CHIMERE model indicates two different regions where AOD peaks around 1,  
1672 over Algeria-Tunisia and southern of Morocco. For COSMO-M and CHIMERE, no intense dust AOD are  
1673 simulated over the northeast Africa (Lybia and Egypt) and values are below 0.25, contrary to RegCM and  
1674 CNRM-RCSM that simulate moderate AOD over this region with more intense peaks (~0.7 for CNRM-RCSM  
1675 simulations). Some identified regions with important AOD over Tunisia, Algeria, and South Morocco are well  
1676 captured by all models except COSMO-M which show more intense AOD south of Algeria. It should be noted  
1677 that this regional pattern of AOD is found to be consistent with MODIS observations as shown by Menut et  
1678 al. (2015) for the CHIMERE model. Averaged over the SOP-1a period, all models simulate low to moderate



1679 AOD over the EURO-Mediterranean region which is consistent with AERONET/PHOTONS observations  
1680 (Figure 14). Once again and as noted by Menut et al. (2015), this modeling exercise clearly shows that the  
1681 summer 2013 was not characterized by intense dust plumes or intense anthropogenic or forest fire  
1682 emissions. However, modeling results indicate regular dust intrusions during the SOP-1a characterized by  
1683 moderate atmospheric loads. Over Europe, the CTM CHIMERE model obviously simulates anthropogenic  
1684 aerosol AOD (AOD ~ 0.3), especially over the Benelux and Pô Valley that are not simulated by the two other  
1685 regional models. Indeed, CNRM-RCSM simulations reveal a more diffuse AOD about 0.2 over Europe with  
1686 maximum over Western France certainly due to the advection of primary marine particles generated over  
1687 the Atlantic Ocean. RegCM simulations indicate a plume of anthropogenic aerosols over the Balkan region  
1688 mainly due to secondary inorganic species. As RegCM does not use the spectral nudging technique in this  
1689 simulation and are only forced at the boundaries during the period of simulation, some biases in  
1690 meteorological fields could appear (as for the precipitation location and intensity), which need to be  
1691 evaluated. Finally and in addition to analysis of the AOD regional pattern, a specific comparison with in-situ  
1692 observations and remote-sensing (AERONET/PHOTONS and satellite) data has been made for the CTM-  
1693 CHIMERE model (Menut et al., 2015) and is planned in accompanied studies for the COSMO-M, RegCM and  
1694 CNRM-RCSM models, associated with an inter-comparison exercise for evaluating the dust emissions,  
1695 vertical distribution, size distribution and dry/wet deposition using all data collected in the framework of  
1696 the SOP-1a.

1697 In parallel to time averaged AOD simulated at the regional scale, we report comparisons of simulated AOD  
1698 with AERONET/PHOTONS data for the two reference stations (Lampedusa and Ersa). As reported in Table 7,  
1699 it should be reminded here that all models did not take into account aerosol species in a similar way. As an  
1700 example, COSMO-MUSCAT includes mineral dust only in this simulation, while CNRM-RCSM and RegCM  
1701 model include natural (sea-spray and dust) and sulfates as well as secondary ammonium and nitrate  
1702 particles (treated as bulk aerosols) but for RegCM only. **The most complete regional model is the CTM-  
1703 CHIMERE, which takes into account natural and all anthropogenic particles (including secondary organics  
1704 and inorganic) resolved in size by using a number of bins (Menut et al., 2013) higher than used in RegCM,  
1705 CNRM-RCSM or COSMO-MUSCAT (number of dust bins between 3 to 4 bins) models.** Figure 31 reports the

1706 time evolution of simulated and observed AOD at 550 nm for the two sites (Ersa and Lampedusa) during the  
1707 SOP-1a. Time correlation, as well as bias, is calculated after removing AERONET/PHOTONS data for the 27<sup>th</sup>  
1708 of June, strongly affected by smoke aerosols transported from Northern America biomass burning sources  
1709 that are not included in the different domains. Figure 31 indicates that all models are able to simulate AOD  
1710 in the range of magnitude of observations. For the dusty Lampedusa site, CNRM-RCSM and CHIMERE reveal  
1711 high temporal correlations (0.82, 0.85, respectively), with standard deviations close to AERONET/PHOTONS  
1712 data, especially for CHIMERE. For this station, COSMO-M and RegCM display moderate temporal correlation  
1713 (0.55 and 0.49, respectively) compared to CNRM-RCSM and CHIMERE. As already mentioned, one reason of  
1714 lowest time-correlation for these models is related to the fact that they are only forced at the boundaries  
1715 and the synoptic conditions inside the domain can derive during the simulation. This effect is limited for  
1716 CNRM-RCSM that used the spectral nudging technique and for CHIMERE forced by WRF meteorological field  
1717 (Menut et al., 2015). For each models, biases are shown to be low, both positive (for CNRM-RCSM and  
1718 CHIMERE) and negative (for COSMO-M and RegCM).

1719 For the Ersa station, less influenced by long-range transport of mineral dust during this period, temporal  
1720 correlations are lowest and found to be moderate (0.40) for CHIMERE and COSMO-M and low for RegCM  
1721 and CNRM-RCSM. In terms of bias, values are positive and low (0.02 to 0.04) for all models, except for  
1722 COSMO-M (-0.07) that does not include anthropogenic aerosols nor sea-spray in the present simulation  
1723 (Table 7). For each model, calculated standard deviations are in the same range of magnitude but slightly  
1724 higher than observations, especially for RegCM (bias of 0.08) that simulated a large AOD for 19-20 of June  
1725 period. By comparison with the values obtained in Lampedusa, these low correlations at Ersa reveal the  
1726 limitations of these models in terms of horizontal resolution with respect to the representativeness of the  
1727 site. Lampedusa being isolated in the middle of the Mediterranean and under the main pathways of African  
1728 mineral dust, AOD is mostly related to long-ranged transport. On the other hand, the site of Ersa in Corsica  
1729 may be under several types of aerosols contributions (anthropogenic, biogenic) more intense and more  
1730 spatially variables than in Lampedusa. Ersa being closer to large industrial areas, the models with a  
1731 horizontal resolution of tens of kilometers are probably not highly enough resolved to catch small scales  
1732 aerosols plumes from the continent.

## 1733 **6.5.2 Regional SW 3-D direct radiative forcing**

1734 The SW (clear-sky) DRF, averaged for the SOP-1a period, has been estimated from the RegCM and CNRM-  
1735 RCSM models, both at the surface and TOA, as shown in the Figure 32. For this discussion, we only consider  
1736 these two models as they estimate the clear-sky SW DRF by taking into account natural and anthropogenic  
1737 aerosols, contrary to the COSMO-MUSCAT model in this study. At the surface first, one can observe the  
1738 large regional dimming due to anthropogenic (especially over Europe) and natural (Northern Africa and  
1739 Mediterranean) particles over the Euro-Mediterranean. Concerning the North African region, both models  
1740 simulate large surface forcing  $\sim -20 \text{ W m}^{-2}$  (with local maxima of  $-50 \text{ W m}^{-2}$  associated with higher AOD).  
1741 CNRM-RCSM is shown to simulate higher surface radiative forcing for the whole domain, especially over  
1742 Algeria. Although such RCM climate models are not designed to simulate finely the size distribution and the  
1743 chemical composition of aerosols as an A-Q system (Menut et al., 2013), a first estimate of the radiative  
1744 effect of polluted particles over Europe is provided. Figure 32 displays a negative forcing, obviously lower  
1745 than for mineral dust, of about  $-10$  to  $-15 \text{ W m}^{-2}$  for RegCM, especially over Balkans and no significant  
1746 radiative effect over the Benelux region for this period. Over the continental region, CNRM-RCSM simulated  
1747 a more diffuse surface forcing with values around  $-10 \text{ W m}^{-2}$ , including a large part of Europe (France,  
1748 Benelux and Eastern Europe). As shown recently by Nabat et al. (2015a), this decrease in SW radiations due  
1749 to aerosols could perturb the surface continental temperature, SST and latent heat fluxes over the  
1750 Mediterranean Sea and more largely on meteorological fields.

1751 At TOA, the dipole of the direct forcing between the North and the South of the domain is well reproduced  
1752 by the two RCM systems with more intense values for CNRM-RCSM. One can clearly observe positive forcing  
1753 at TOA (heating) over Northern Africa and negative forcing (cooling) over the Mediterranean and Europe.  
1754 This represents one of the characteristics of the Euro-Mediterranean region with a large variability of  
1755 surface albedo from the South (with higher values) to the North (low to moderate albedo). Due to this  
1756 gradient in the surface albedo, moderate absorbing dust aerosols emitted over Northern Africa  
1757 (characterized by high surface albedo) decrease the shortwave radiations reflected at TOA, compared to a  
1758 non-turbid atmosphere. When advected above low surface reflectance as marine or dense forest over  
1759 Europe, dust aerosols increase the upward SW radiations at TOA, leading to a cooling effect. One can see

1760 the transition between positive to negative TOA forcing that occurs over Northern Algeria and Morocco as  
1761 soon as dust particles are transported over darker surfaces. This TOA radiative forcing gradient is well  
1762 captured by such RCM models which use a finer resolution than GCM. Over Europe and Mediterranean, the  
1763 TOA forcing is simulated to be negative for both RCM with lower values around -5 to -10 W m<sup>-2</sup>. Such results  
1764 are consistent with the study of Nicolas et al. (in prep.), who performed two different simulations using  
1765 different surface albedo (from marine to continental), based on the ATR-42 observations above the Balearic  
1766 Islands and the Granada station. The inclusion of high surface albedo (0.27 at 870 nm) in the 1-D radiative  
1767 transfer model compared to low sea-surface albedo (0.02 at 870 nm) contributes to decrease the TOA  
1768 radiative effect at Granada.

1769 The last important point to mention here concerns the fact that most of SW radiations losses at the surface  
1770 are not completely compensated by fluxes reflected back to space. Hence, this gain of solar energy within  
1771 dusty layers (due to moderate dust SW absorption, see Denjean et al., this special issue) has been shown to  
1772 result in significant feedbacks on the temperature and relative humidity profiles over the Mediterranean  
1773 region with some important implications on its climate (Nabat et al., 2015a).

## 1774 **7. Conclusions**

1775  
1776 The special observing period (SOP-1a) performed during the Mediterranean dry season (11 June to 05 July  
1777 2013) over the western and central Mediterranean basins has been described in detail, as well as the 1D to  
1778 3D modeling effort, involved in the ChArMEx/ADRIMED project focused on aerosol-radiation-climate  
1779 interactions. Details of the in-situ and remote-sensing instrumentation deployed at the different sites and  
1780 the main meteorological conditions that occurred during the campaign have been provided. Some results  
1781 from the in-situ and remote-sensing observations, vertical profiles, 1-D and 3-D aerosols direct radiative  
1782 forcing (DRF) computations have also been presented. Concerning the aerosol loading during the SOP-1a,  
1783 our results indicate that numerous but moderate mineral dust plumes were observed during the campaign  
1784 with main sources located in Morocco, Algeria and Tunisia, leading to AOD between 0.1 to 0.6 (at 440 nm)  
1785 over the western and central Mediterranean. Analysis of synoptic situations demonstrates unfavorable  
1786 conditions to produce large concentrations of polluted-smoke particles during the SOP-1a but interesting  
1787 sea-spray events have been observed.

1788 Aerosol extinctions measured on-board the ATR-42 show local maxima reaching up to  $150 \text{ Mm}^{-1}$  within the  
1789 dust plume, associated to extinctions of about  $50 \text{ Mm}^{-1}$  within the Marine Boundary Layer (MBL) possibly  
1790 due to the presence of sea-spray aerosols. By combining ATR-42 extinction, absorption and scattering  
1791 measurements, complete optical closures have been made revealing an excellent agreement in estimated  
1792 optical properties. This additional information on extinction properties has allowed calculating the dust  
1793 single scattering albedo (SSA) with a high level of confidence over the Western Mediterranean. Our results  
1794 show a surprising moderate variability from 0.90 to 1.00 (at 530 nm) for all flights studied, corroborated by  
1795 AERONET/PHOTONS SSA retrievals. The SSA derived during the ChArMEx/ADRIMED project has been also  
1796 compared with referenced values obtained near dust sources, showing a relatively low difference in this  
1797 optical parameter at 530 nm.

1798 Concerning the aerosol vertical structure, active remote-sensing observations, at the surface and onboard  
1799 the F-20, indicate complex vertical profiles of particles with sea-spray and pollution located in the MBL, and  
1800 mineral dust and/or even aged North American smoke particles located above (up to 6-7 km in altitude).  
1801 Microphysical properties of aerosols measured onboard the ATR-42 and balloon-borne observations for  
1802 transported/aged mineral dust reveal particle volume size distributions with diameters greater than  $10 \mu\text{m}$ .  
1803 In most of cases, a coarse mode of mineral dust particles, characterized by an effective diameter  $D_{\text{eff},c}$   
1804 ranging between 5 and  $10 \mu\text{m}$ , has been detected within the dust layer located above the MBL. Such values  
1805 are found to be larger than those referenced in dust source regions during FENNEC, SAMUM1 and AMMA,  
1806 as well as measurements in the Atlantic Ocean at Cape-Verde region during SAMUM-2 and at Puerto-Rico  
1807 during PRIDE.

1808 In terms of shortwave (SW) and longwave (LW) DRF, in-situ surface and aircraft observations have been  
1809 merged and used as inputs in different radiative transfer codes for calculating the 1-D DRF. Modeling results  
1810 show significant surface (instantaneous) SW radiative forcing down to as much as  $-90 \text{ W m}^{-2}$  over super-  
1811 sites. In parallel, AOD together with surface radiative fluxes observations have also been used to directly  
1812 estimate the local daily surface forcing in SW (and LW) spectral regions, showing a significant effect with  
1813 values of  $-15 \text{ W m}^{-2}$  ( $+5.5 \text{ W m}^{-2}$ ) over Lampedusa. Such DRF values are consistent with those previously  
1814 referenced over the Mediterranean basin. In parallel, aircraft observations provide also original and new

1815 estimates of SW and LW radiative heating vertical profiles with significant values of SW heating of about 5°K  
1816 per day within the dust layer (for a solar angle of 30°).

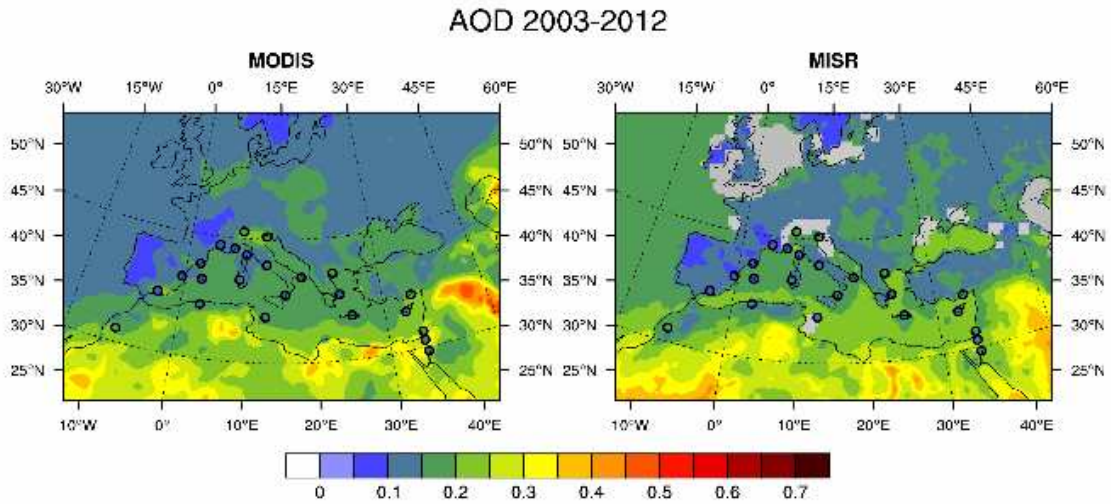
1817 Associated 3-D modeling studies, using regional climate (RCM) and chemistry transport (CTM) models,  
1818 indicate a relatively good agreement between simulated AOD and that determined from  
1819 AERONET/PHOTONS data. Such models allow 3-D calculations of the daily SW DRF revealing a regional DRF  
1820 of -10 to -20 Wm<sup>-2</sup> (at the surface and in clear-sky conditions), when averaged over the SOP-1a period. At  
1821 TOA, a significant dipole in the DRF is estimated between the North and the South of the domain, with  
1822 positive (heating) over Northern Africa and negative (cooling) DRF over the Mediterranean basin and  
1823 Europe, reflecting changes in surface albedo associated to moderately absorbing aerosols. A first multi-year  
1824 simulation (conducted for the 2003 to 2009 period) that takes into account the ocean-atmosphere coupling  
1825 has demonstrated that the significant aerosol radiative forcing is responsible for a decrease in sea surface  
1826 temperature (on average -0.5 °C for the Mediterranean). In addition, the latent heat loss is shown to be  
1827 weaker in the presence of aerosols, resulting in a decrease in specific humidity in the lower troposphere,  
1828 and a reduction in cloud cover and precipitation.

1829 This unprecedented dataset of aerosol microphysical, chemical, optical properties and vertical profiles  
1830 obtained over the western Mediterranean will now be used for evaluating regional models to reproduce  
1831 such properties. In addition to classical model evaluations based generally on the AOD, new comparisons  
1832 between models and in-situ observations on aerosol absorbing (SSA and AAOD) properties and SW and LW  
1833 heating rates, which control the semi-direct effect of aerosols, should be conducted. Comparisons will also  
1834 be performed on the aerosol size distribution for investigating the ability of regional models to simulate the  
1835 observed large dust particle size during the transport over the Mediterranean, which could be helpful for  
1836 improving the representation of deposition in such models. In parallel, in-situ observations of sea-spray  
1837 particles obtained at the surface and from ATR-42 measurements will also be used to evaluate the different  
1838 primary sea-spray generation schemes, in terms of concentration and size distribution. The objective is to  
1839 improve the representation of microphysical and optical properties of aerosols in regional climate models  
1840 which will be used in multi-year simulations to assess the impact of natural and anthropogenic aerosols on  
1841 climate in this region.

## 1842 Acknowledgments

1843 This research has received funding from the French National Research Agency (ANR) projects ADRIMED  
1844 (contract ANR-11-BS56-0006). This work is part of the ChArMEx project supported by ADEME, CEA, CNRS-  
1845 INSU and Météo-France through the multidisciplinary programme MISTRALS (Mediterranean Integrated  
1846 Studies at Regional And Local Scales). The station at Erba was partly supported by the CORSiCA project  
1847 funded by the Collectivité Territoriale de Corse through the Fonds Européen de Développement Régional of  
1848 the European Operational Program 2007-2013 and the Contrat de Plan Etat-Région. We acknowledge the  
1849 AERONET/PHOTONS sun-photometer networks and the PIs of the selected stations and their staff for their  
1850 work to produce the dataset used in this study. The financial support for EARLINET in the ACTRIS Research  
1851 Infrastructure Project by the European Union's Horizon 2020 research and innovation programme under  
1852 grant agreement n. 654169 and previously under grant agreement n. 262254 in the 7th Framework  
1853 Programme (FP7/2007-2013) is gratefully acknowledged. In particular, the authors are thankful to the  
1854 Italian EARLINET PIs (Maria Rita Perrone, Lecce; Nicola Spinelli, Naples; Gelsomina Pappalardo, Potenza;  
1855 Simona Scollo, Serra La Nave) and their staff. Measurements at Lampedusa by ENEA were partly supported  
1856 by the Italian Ministry for University and Research through the NextData and Ritmare Projects. This study,  
1857 especially the balloon campaign and part of the aircraft operations has also been supported by the French  
1858 space agency (CNES). The technical staff of SAFIRE, INSU Technical Division and the CNES Balloon sub-  
1859 directorate (with special mention to Aurélien Bourdon and Gilles Dupouy) are warmly acknowledged for  
1860 their contribution to the success of the experimental work. Contributions by Didier Bruneau (Latmos), Silvia  
1861 Becagli (Univ. of Florence, Italy), Marco Cacciani (Univ. of Rome, Italy), Julian Groebner and Natalia  
1862 Kouremeti (Physikalisch-Meteorologisches Observatorium Davos, World Radiation Center, Switzerland), and  
1863 José Antonio Martínez Lozano (University of Valencia, Spain) are gratefully acknowledged. Barcelona station  
1864 was partially supported by the Spanish Ministry of Economy and Competitiveness (project TEC2012-34575) and  
1865 of Science and Innovation (project UNPC10-4E-442) and FEDER funds, and by the Department of Economy  
1866 and Knowledge of the Catalan Autonomous Government (grant 2014 SGR 583). Granada station was  
1867 partially supported by the Andalusian Regional Government through project P12-RNM-2409 and by the  
1868 Spanish Ministry of Science and Technology through project CGL2013-45410-R. Sahar Hassazadeh,  
1869 Constantino Muñoz-Porcar, Santi Bertolín and Diego Lange are also acknowledged for their kind assistance  
1870 in operating the Menorca surface station, as well as François Gheusi, Brice Barret, Flore Tocquer, and Yves  
1871 Meyerfeld for their contribution to the balloon campaign preparation and/or deployment. Claude  
1872 Basdevant, Alexis Doerenbecher, and Fabien Bernard are acknowledged for their help and very useful tools  
1873 in support of our drifting balloon experiment. The Granada station was partially supported by the  
1874 Andalusian Regional Government through project P12-RNM-2409 and by the Spanish Ministry of Science  
1875 and Technology through project CGL2013-45410-R.

1876  
1877  
1878  
1879  
1880  
1881  
1882  
1883  
1884  
1885  
1886  
1887  
1888  
1889  
1890  
1891  
1892  
1893  
1894



1897  
1898 **Figure 1.** Aerosol Optical Depth (at 550 nm) derived from MODIS and MISR satellites for the 2003 to 2012 period. **The**  
1899 **AERONET/PHOTONS AOD are also indicated.**  
1900  
1901  
1902  
1903  
1904  
1905  
1906  
1907  
1908  
1909  
1910  
1911  
1912  
1913  
1914  
1915  
1916  
1917  
1918  
1919  
1920  
1921  
1922  
1923  
1924



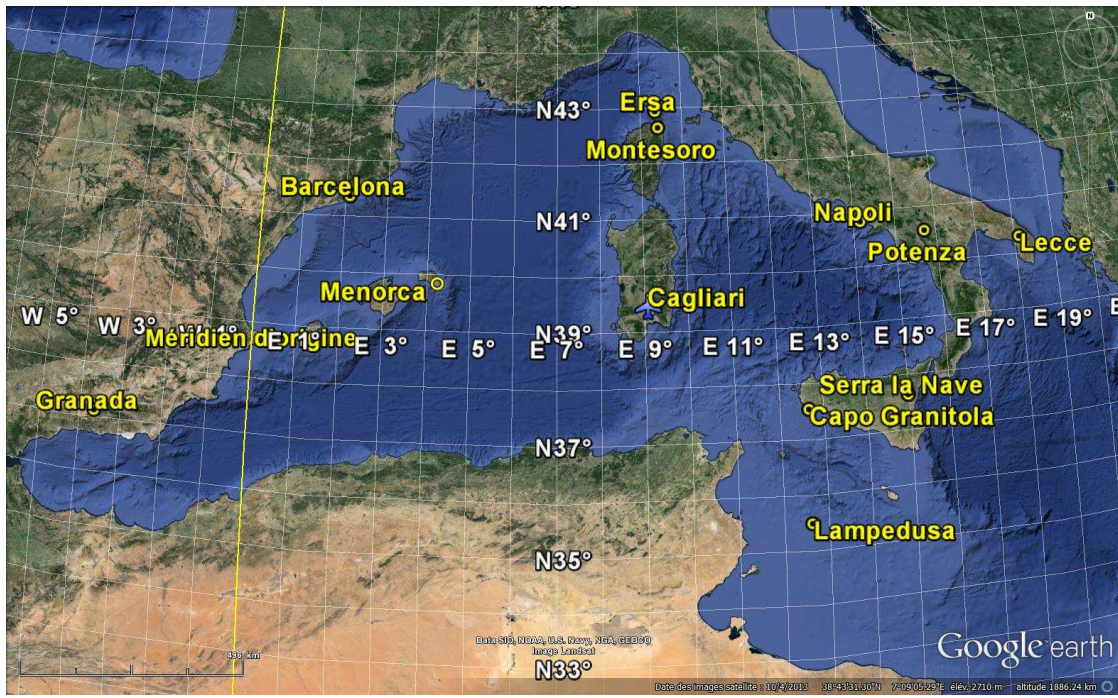


**Figure 2.** The regional experimental set-up deployed in the western and central Mediterranean during the campaign ChArMEx SOP-1a. The two aircrafts were based at Cagliari.

- 1925
- 1926
- 1927
- 1928
- 1929
- 1930
- 1931
- 1932
- 1933
- 1934
- 1935
- 1936
- 1937
- 1938
- 1939
- 1940
- 1941
- 1942
- 1943
- 1944
- 1945
- 1946
- 1947
- 1948
- 1949
- 1950
- 1951
- 1952
- 1953
- 1954
- 1955
- 1956
- 1957
- 1958
- 1959
- 1960
- 1961
- 1962
- 1963

## ADRIDMED flights - ATR42 & Falcon20 - JUNE & JULY 2013

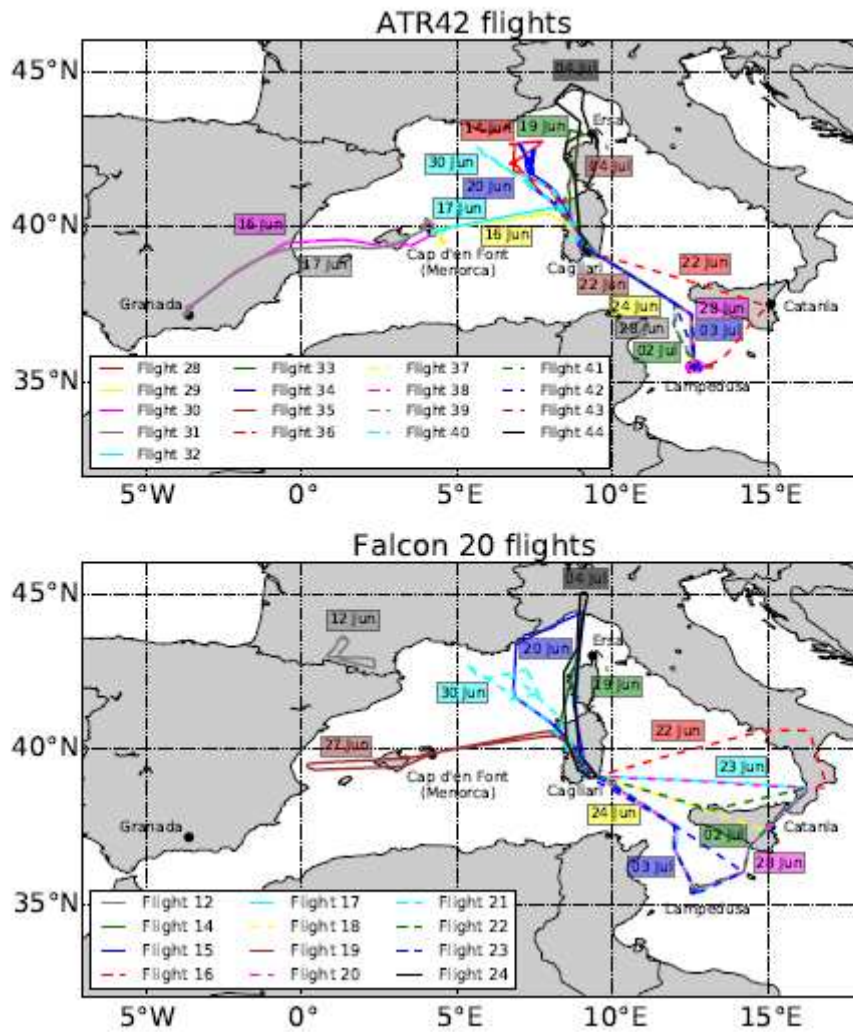


**Figure 3.** Overview of the different ATR-42 and F-20 flight trajectories performed during the SOP-1a experiment.

1964  
1965  
1966  
1967  
1968  
1969  
1970  
1971  
1972  
1973  
1974  
1975  
1976  
1977  
1978  
1979  
1980  
1981  
1982  
1983  
1984  
1985  
1986  
1987  
1988

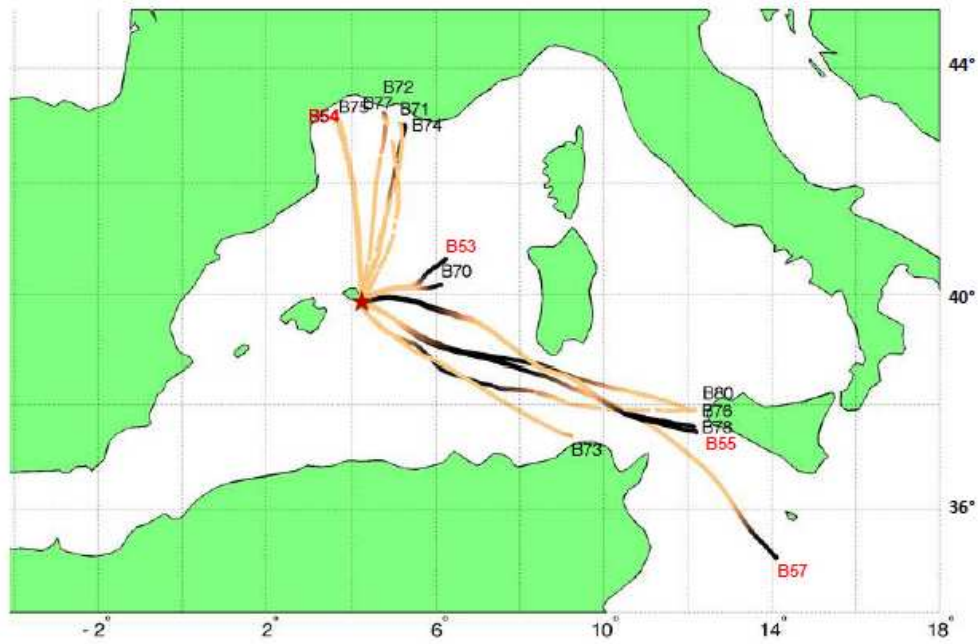


**Figure 4.** Trajectories of the 14 BPCL drifting balloons launched from Minorca Island during the campaign. Dark portion along trajectories correspond to night-time conditions. The four red labels from B54 to B57 indicate balloons with an ozone sonde and the 10 others carried a LOAC instrument.

- 1989
- 1990
- 1991
- 1992
- 1993
- 1994
- 1995
- 1996
- 1997
- 1998
- 1999
- 2000
- 2001
- 2002
- 2003
- 2004
- 2005
- 2006
- 2007
- 2008
- 2009
- 2010
- 2011
- 2012
- 2013
- 2014
- 2015
- 2016
- 2017
- 2018
- 2019
- 2020
- 2021
- 2022
- 2023
- 2024
- 2025

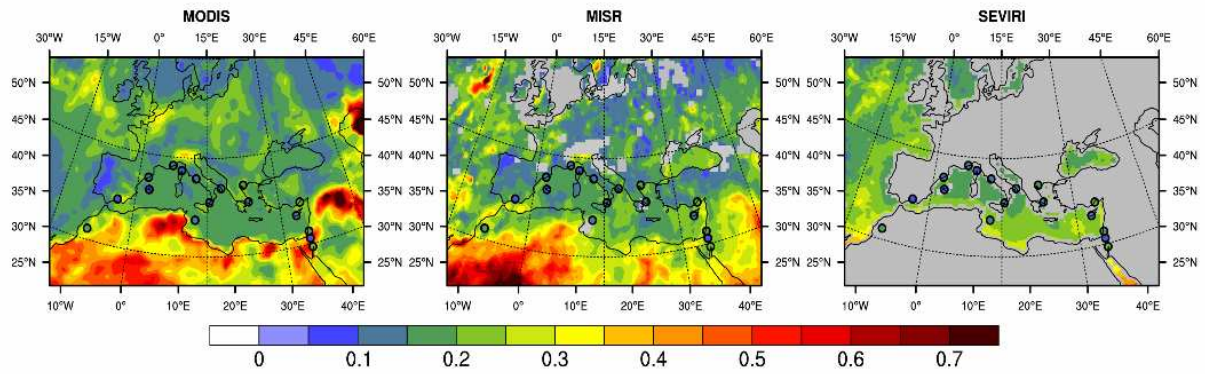
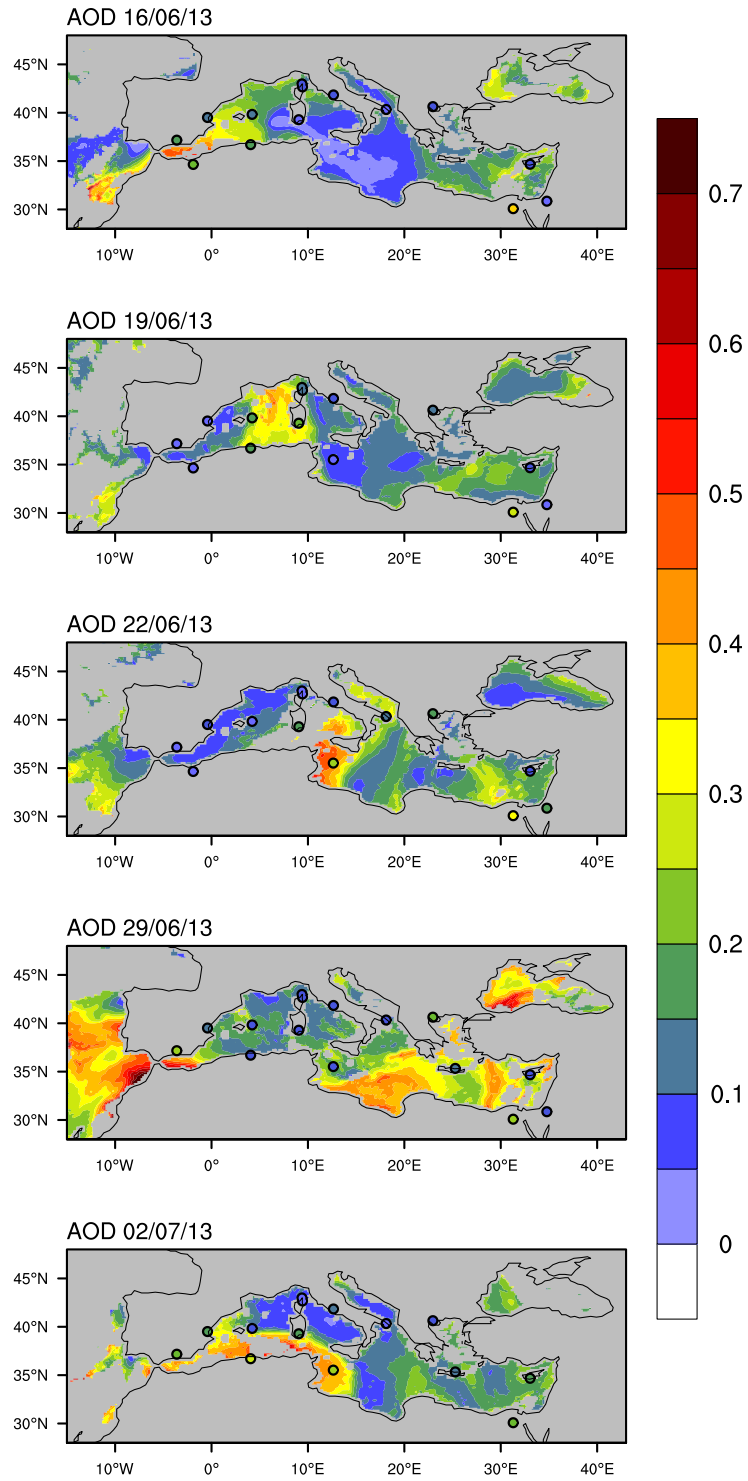


**Figure 5.** Total AOD (500 nm) obtained from the MODIS, MISR and SEVIRI (sea only) sensors for the June-July 2013 period. The AERONET/PHOTONS AOD are also indicated.

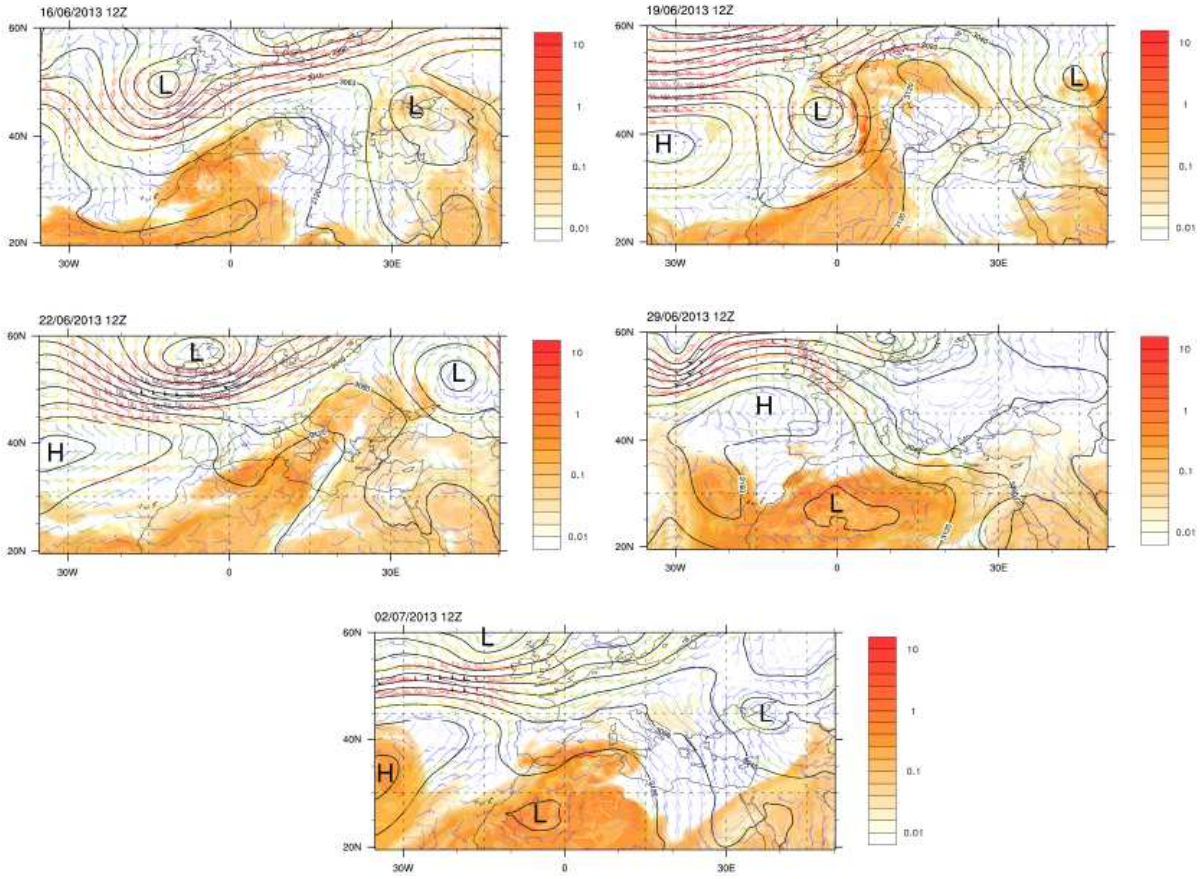
2026  
 2027  
 2028  
 2029  
 2030  
 2031  
 2032  
 2033  
 2034  
 2035  
 2036  
 2037  
 2038  
 2039  
 2040  
 2041  
 2042  
 2043  
 2044  
 2045  
 2046  
 2047  
 2048  
 2049  
 2050  
 2051  
 2052  
 2053  
 2054  
 2055  
 2056  
 2057  
 2058  
 2059  
 2060  
 2061  
 2062  
 2063  
 2064  
 2065



2067  
 2068  
 2069  
 2070  
 2071  
 2072  
 2073  
 2074  
 2075  
 2076  
 2077  
 2078  
 2079

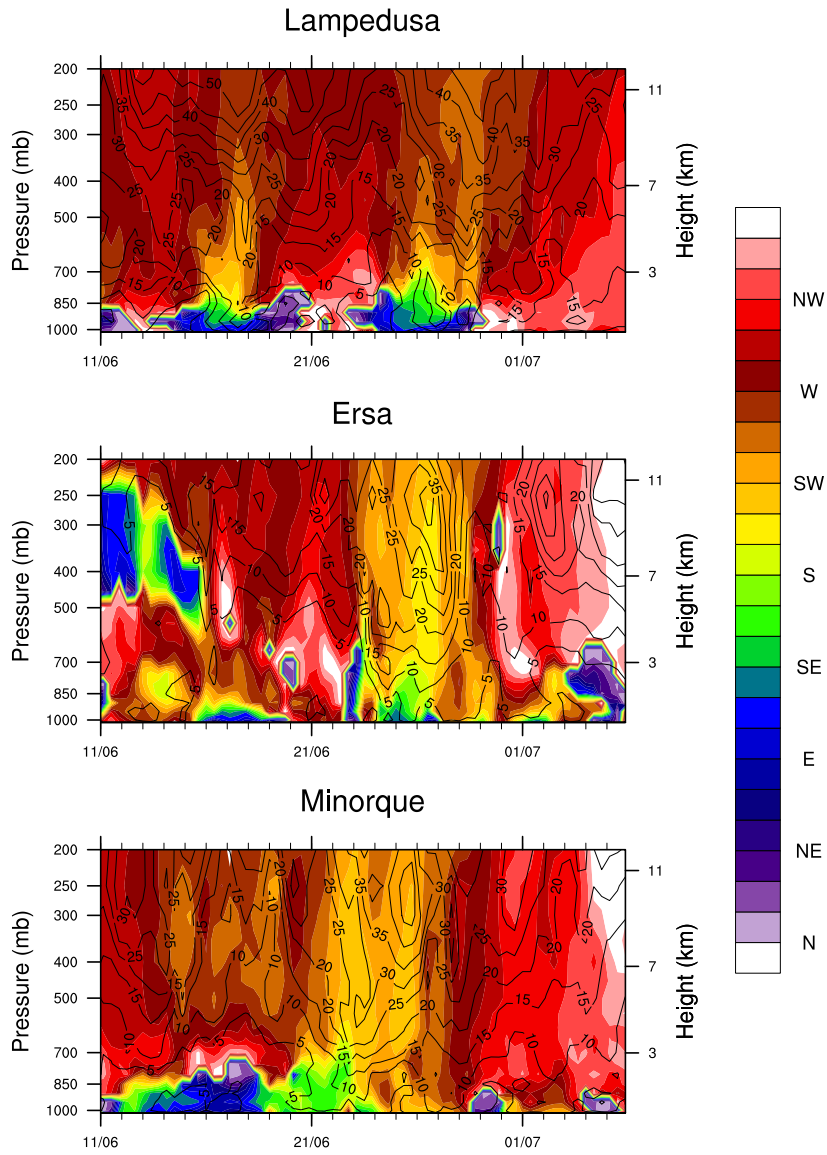
**Figure 6.** AOD MSG/SEVIRI observations for five different days during the SOP-1a experiment (16/06, 19/06, 22/06, 29/06 and 03/07). The AERONET/PHOTONS AOD are also indicated.

2080



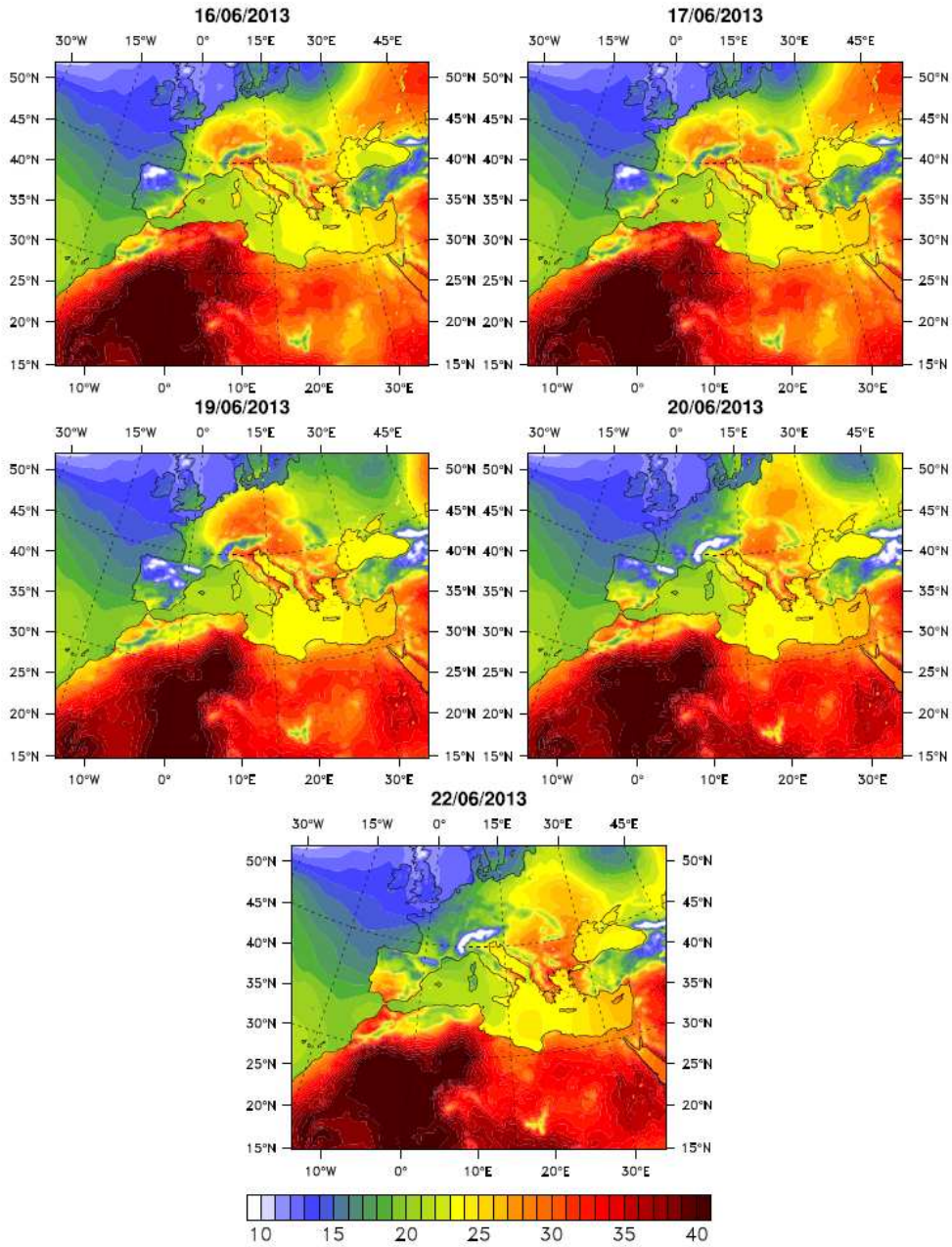
2081  
2082  
2083  
2084  
2085  
2086  
2087  
2088  
2089  
2090  
2091  
2092  
2093  
2094  
2095  
2096  
2097  
2098  
2099  
2100  
2101  
2102  
2103  
2104  
2105  
2106  
2107  
2108  
2109  
2110  
2111  
2112

**Figure 7.** Geopotential at 700 hPa, mass dust concentration (in  $\text{mg}\cdot\text{m}^{-3}$ ), and wind intensity at 700 hPa for the 06, 19, 22, 29 of June and 02 of July at 12:00 UTC, simulated from the ALADIN model.



2114  
 2115  
 2116  
 2117  
 2118  
 2119  
 2120  
 2121  
 2122  
 2123  
 2124  
 2125  
 2126  
 2127  
 2128  
 2129  
 2130  
 2131  
 2132  
 2133  
 2134  
 2135  
 2136

**Figure 8.** Wind profiles between 1000 and 200 hPa during the SOP-1a experiment for three different sites (Ersa, Lampedusa and Minorca) simulated from the ALADIN model. The wind intensity (in  $m s^{-1}$ ) is also reported at the differents stations.

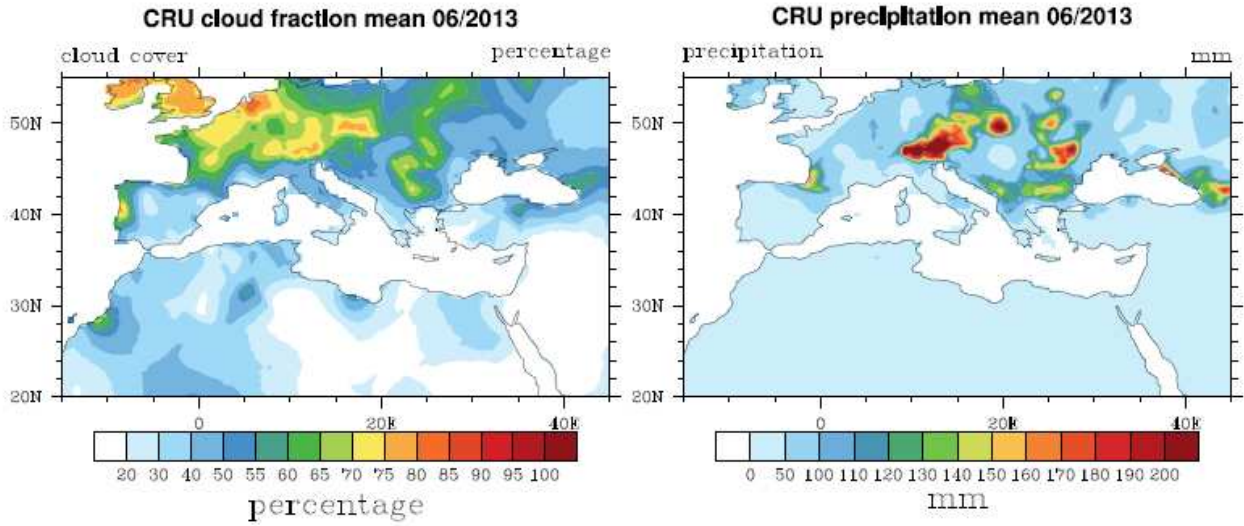


2138  
 2139  
 2140  
 2141  
 2142  
 2143  
 2144  
 2145  
 2146  
 2147  
 2148  
 2149  
 2150  
 2151  
 2152  
 2153  
 2154  
 2155  
 2156

**Figure 9.** Surface Temperature (at 12:00 UTC) obtained from NCEP re-analysis for the 16, 17, 19, 20 and 22 of June.



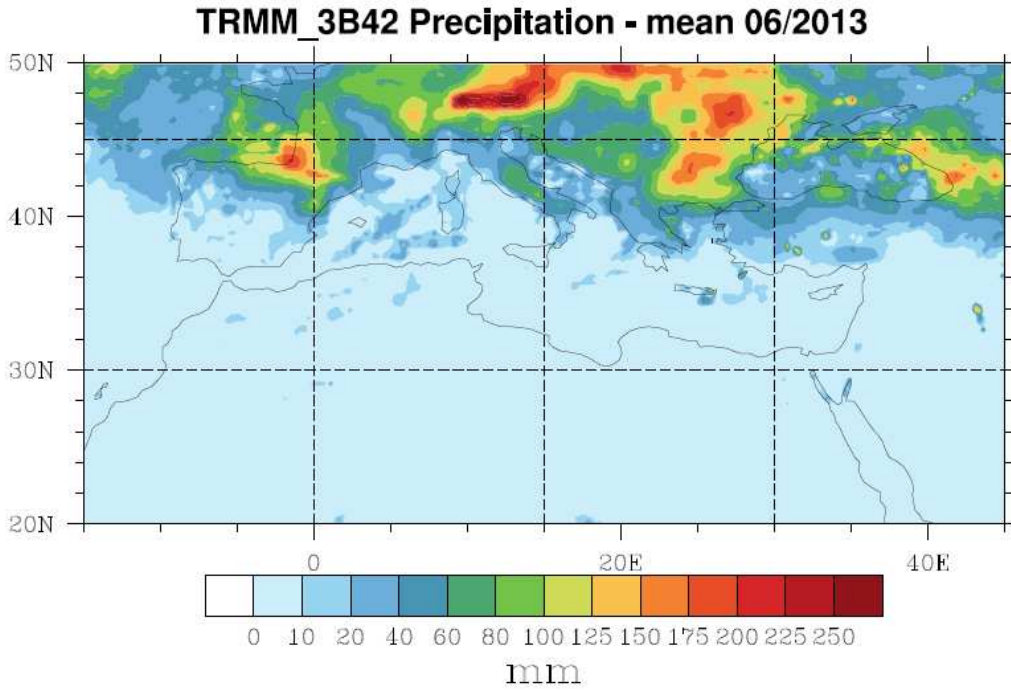
2157



2158  
2159  
2160  
2161  
2162  
2163  
2164  
2165  
2166  
2167  
2168  
2169  
2170  
2171  
2172  
2173  
2174  
2175  
2176  
2177  
2178  
2179  
2180  
2181  
2182  
2183  
2184  
2185  
2186  
2187  
2188  
2189  
2190  
2191  
2192  
2193  
2194  
2195  
2196  
2197  
2198

**Figure 10.** Monthly cloud cover and precipitation (over land only) derived from the Climate Research Unit (CRU) data for June 2013.

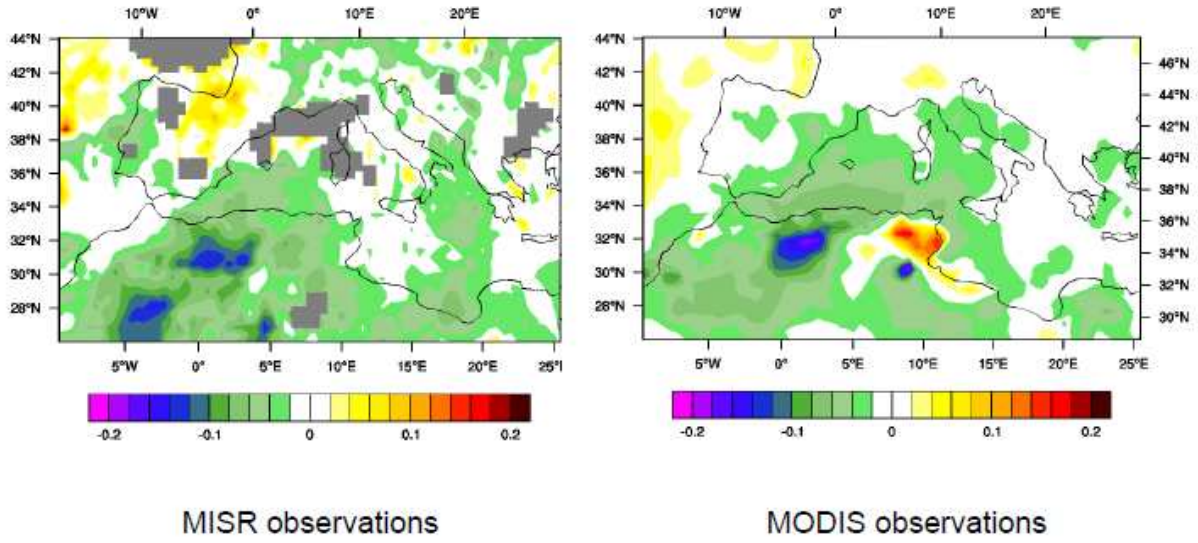
2199



2200  
2201  
2202  
2203  
2204  
2205  
2206  
2207  
2208  
2209  
2210  
2211  
2212  
2213  
2214  
2215  
2216  
2217  
2218  
2219  
2220  
2221  
2222  
2223  
2224  
2225  
2226  
2227  
2228  
2229  
2230  
2231  
2232  
2233  
2234  
2235

**Figure 11.** Same figure as 10 but for the Tropical Rainfall Measuring Mission (TRMM) precipitation observations.

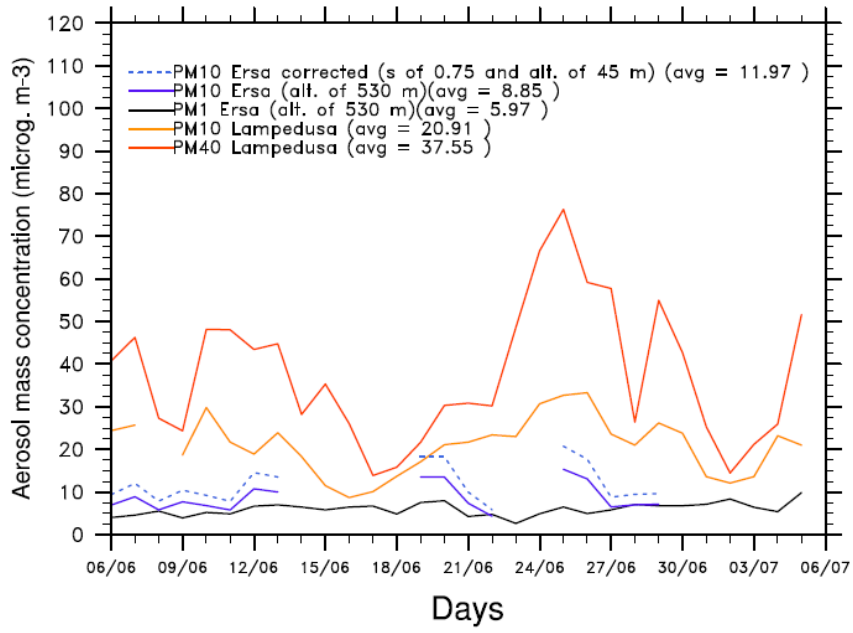
2236



2237  
2238  
2239  
2240  
2241  
2242  
2243  
2244  
2245  
2246  
2247  
2248  
2249  
2250  
2251  
2252  
2253  
2254  
2255  
2256  
2257  
2258  
2259  
2260  
2261  
2262  
2263  
2264  
2265  
2266  
2267  
2268  
2269  
2270  
2271  
2272  
2273  
2274  
2275  
2276

Figure 12. AOD anomaly for summer 2013 estimated from the MODIS and MISR sensor data.

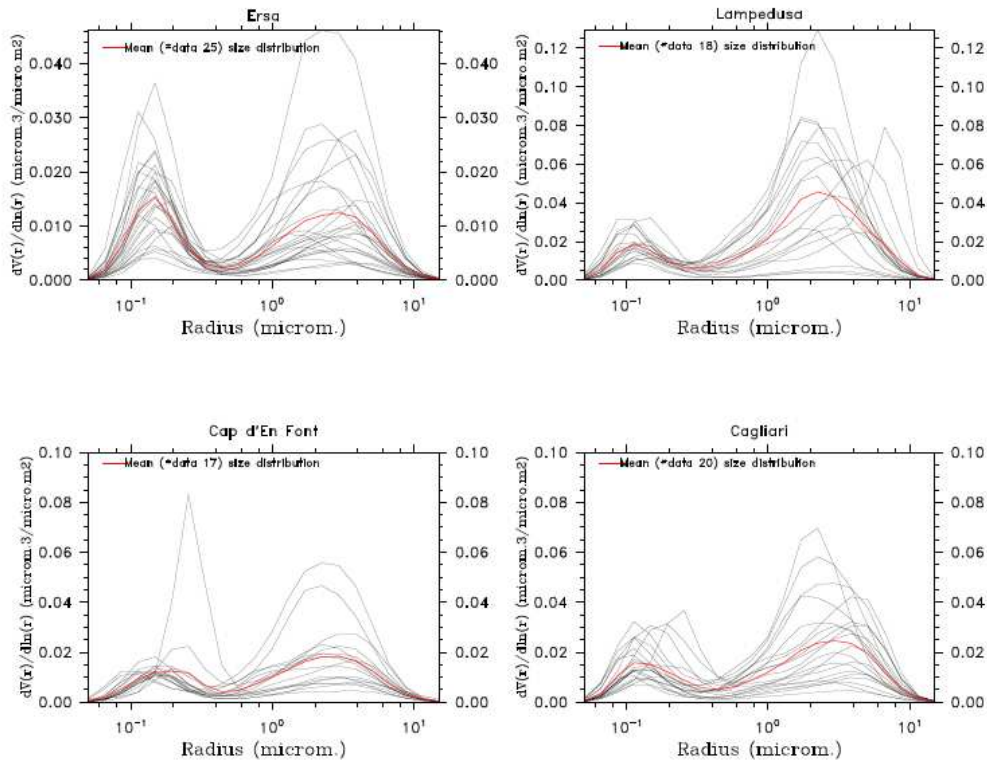
2277



2278  
2279  
2280  
2281  
2282  
2283  
2284  
2285  
2286  
2287  
2288  
2289  
2290  
2291  
2292  
2293  
2294  
2295  
2296  
2297  
2298  
2299  
2300  
2301  
2302  
2303  
2304  
2305  
2306  
2307  
2308  
2309  
2310  
2311  
2312  
2313  
2314

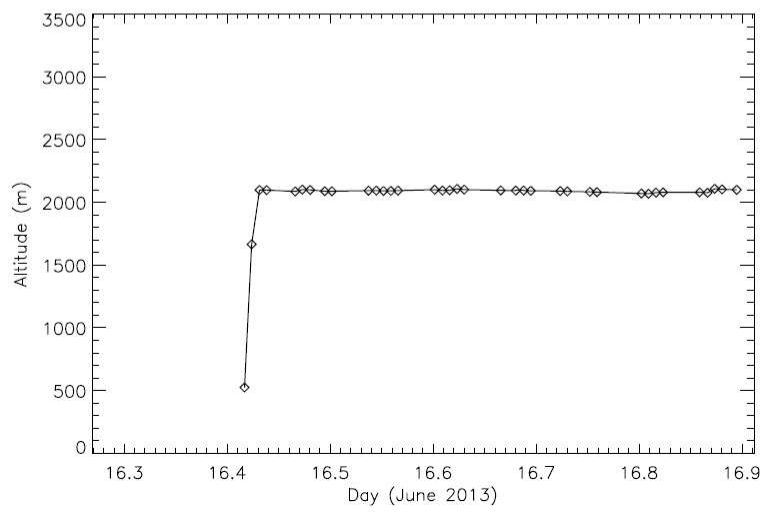
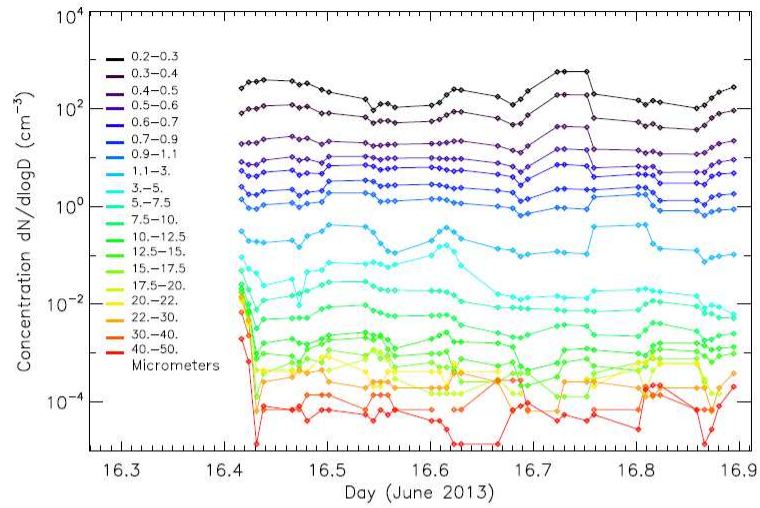
**Figure 13.** Time-series of daily PM mass concentrations estimated at the Lampedusa (PM40 and PM10) and Ersal (PM1 and PM10) super-stations. Problems in PM10 data acquisition that occurred at Ersal explain the gaps. “PM10 Ersal corrected” curve correspond to PM10 estimated at an altitude of 45m to be comparable with Lampedusa results, following the logarithmic law provided by Piazzola et al. (2015), (see text in section 5.1.1 for details).

SOP-1a AERONET/PHOTONS Volume size distribution



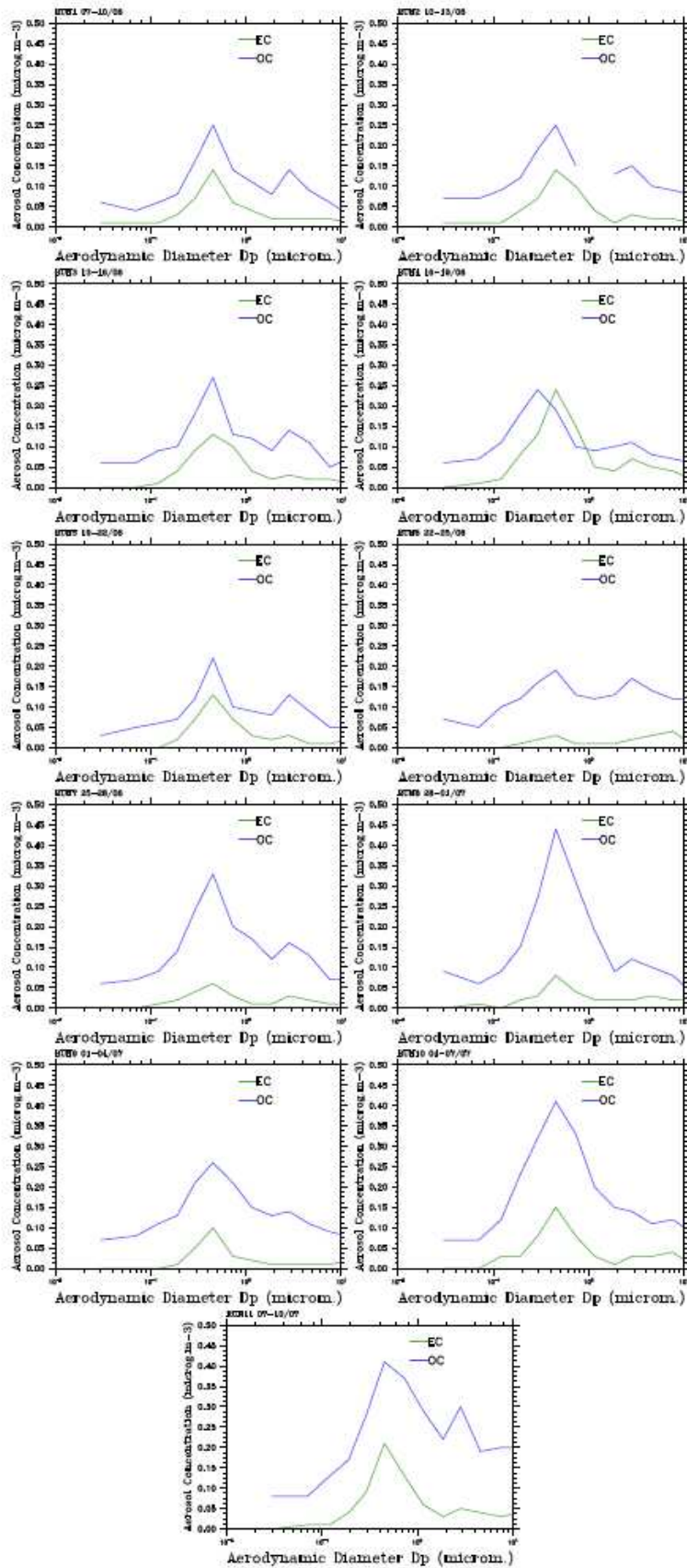
2315  
 2316  
 2317  
 2318  
 2319  
 2320  
 2321  
 2322  
 2323  
 2324  
 2325  
 2326  
 2327  
 2328  
 2329  
 2330  
 2331  
 2332  
 2333  
 2334  
 2335  
 2336  
 2337  
 2338  
 2339  
 2340  
 2341  
 2342

**Figure 14.** AERONET/PHOTONS volume size distribution derived at four different stations: Ersa, Lampedusa, Cagliari and Cap d'En Font (the red curve represents the mean of observations). The characteristics of the volume size distribution are provided in Table 6.



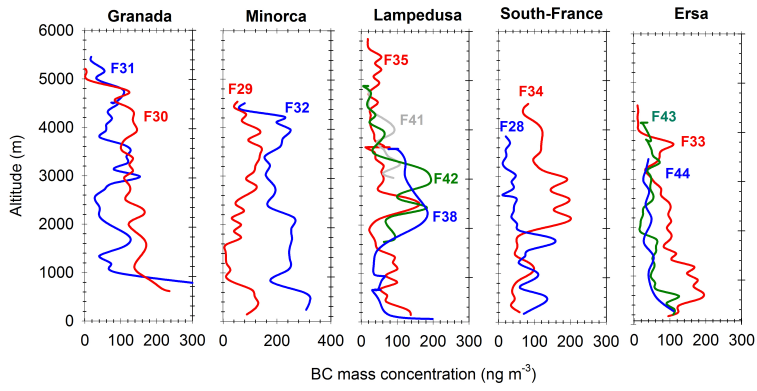
2343  
 2344  
 2345  
 2346  
 2347  
 2348  
 2349  
 2350  
 2351  
 2352  
 2353  
 2354  
 2355  
 2356  
 2357  
 2358  
 2359  
 2360  
 2361

**Figure 15.** Particle size distribution measured with a LOAC during the ~12-h flight of the BPCL balloon B74 drifting from Minorca Island towards Marseille (see trajectory in Figure 4). The first and last 20 min correspond to the ascending and descending phases of the quasi-Lagrangian flight which occurred at a constant altitude of  $2091 \pm 10$  m.



2362  
 2363  
 2364  
 2365  
 2366  
 2367

**Figure 16.** EC and OC (48h-mean) aerosol mass size distributions obtained at Ersa from the impactor DEKATI instrument for all the SOP-1a period.



2368  
2369  
2370

**Figure 17.** Vertical profiles of rBC concentrations estimated from SP2 instrument for 5 different zones (Granada, Minorca, Lampedusa, South-France and Ersa).



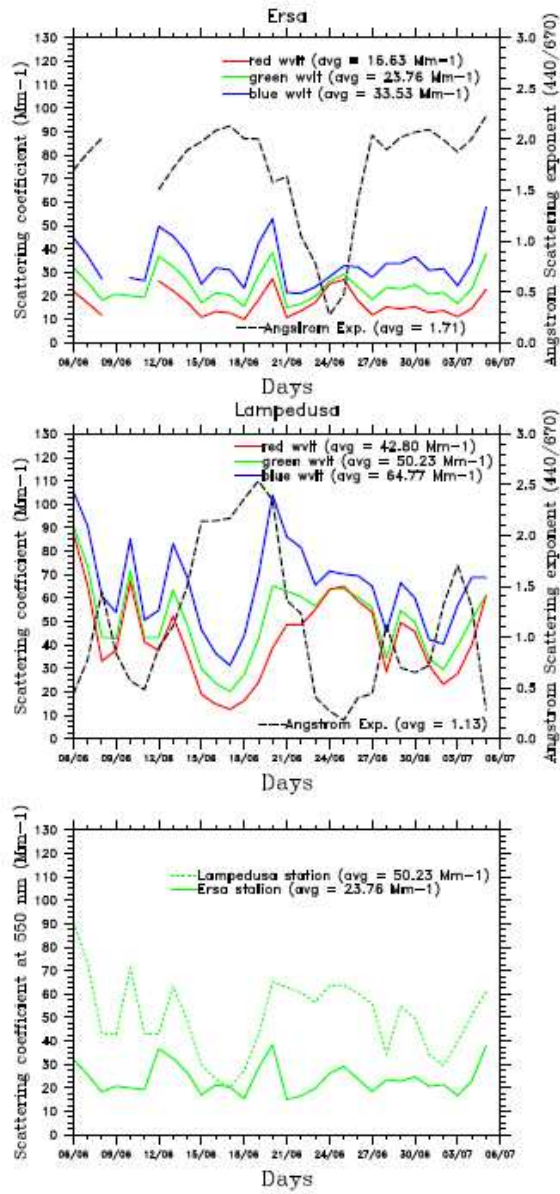


**Figure 18.** Time-series of daily scattering coefficient (in Mm<sup>-1</sup>) estimated in the Ersu and Lampedusa stations. The daily Angström Exponent (AE), calculated between 440 and 670 nm, is also reported.

2371  
 2372  
 2373  
 2374  
 2375  
 2376  
 2377  
 2378  
 2379  
 2380  
 2381  
 2382  
 2383  
 2384  
 2385  
 2386  
 2387  
 2388  
 2389  
 2390  
 2391

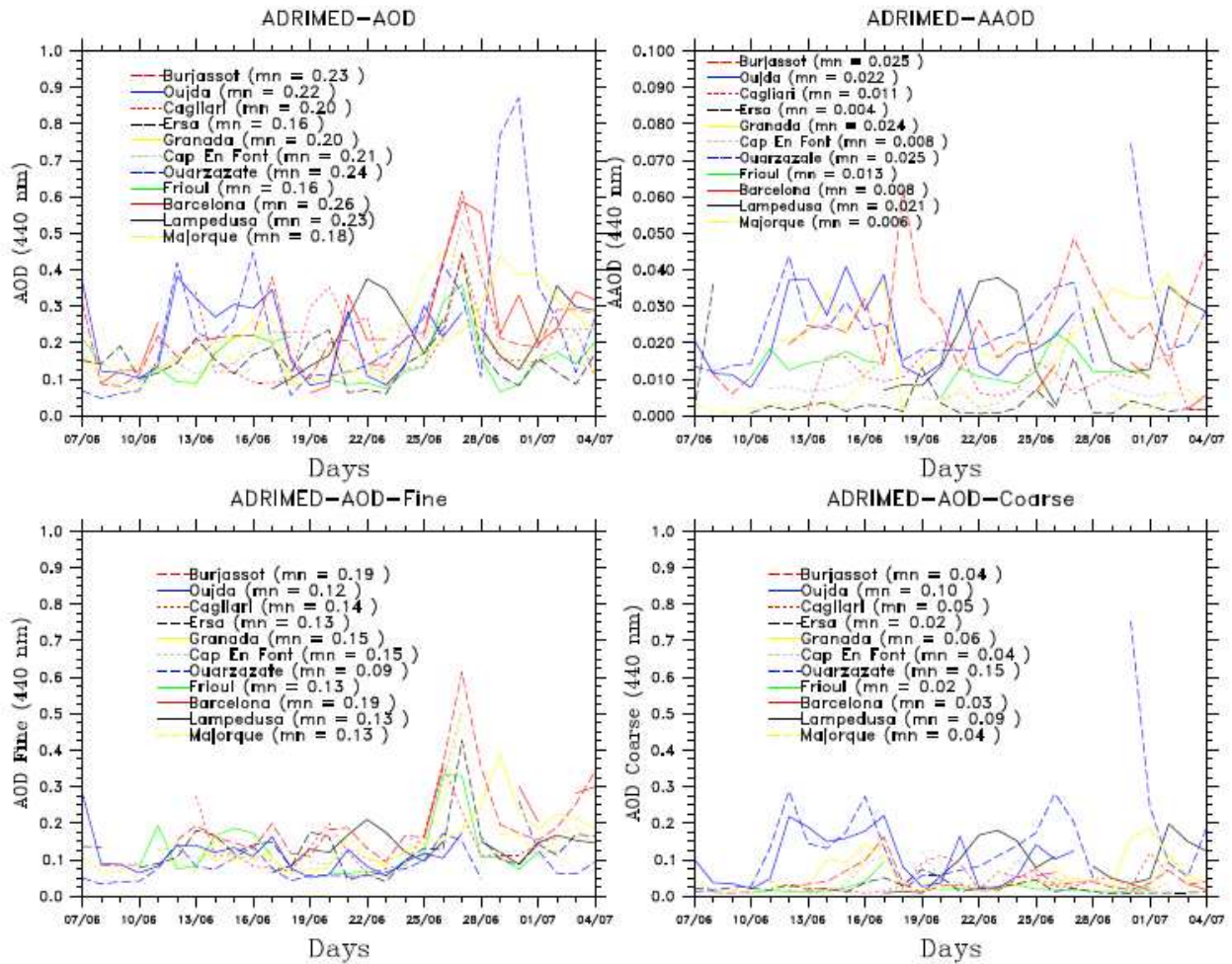
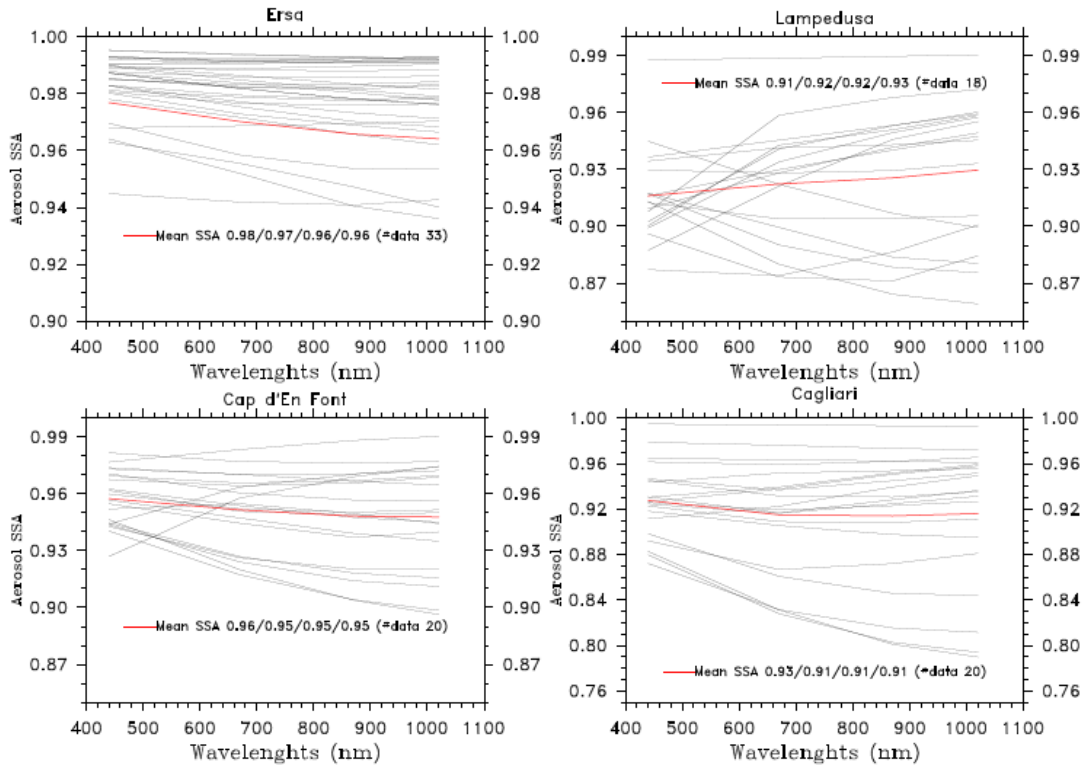


**Figure 19.** AERONET/PHOTONS observations of the total extinction AOD, AOD Fine (AODf), AOD Coarse (AODc) and Absorbing AOD (AAOD), at 440 nm obtained for the whole SOP-1a period.

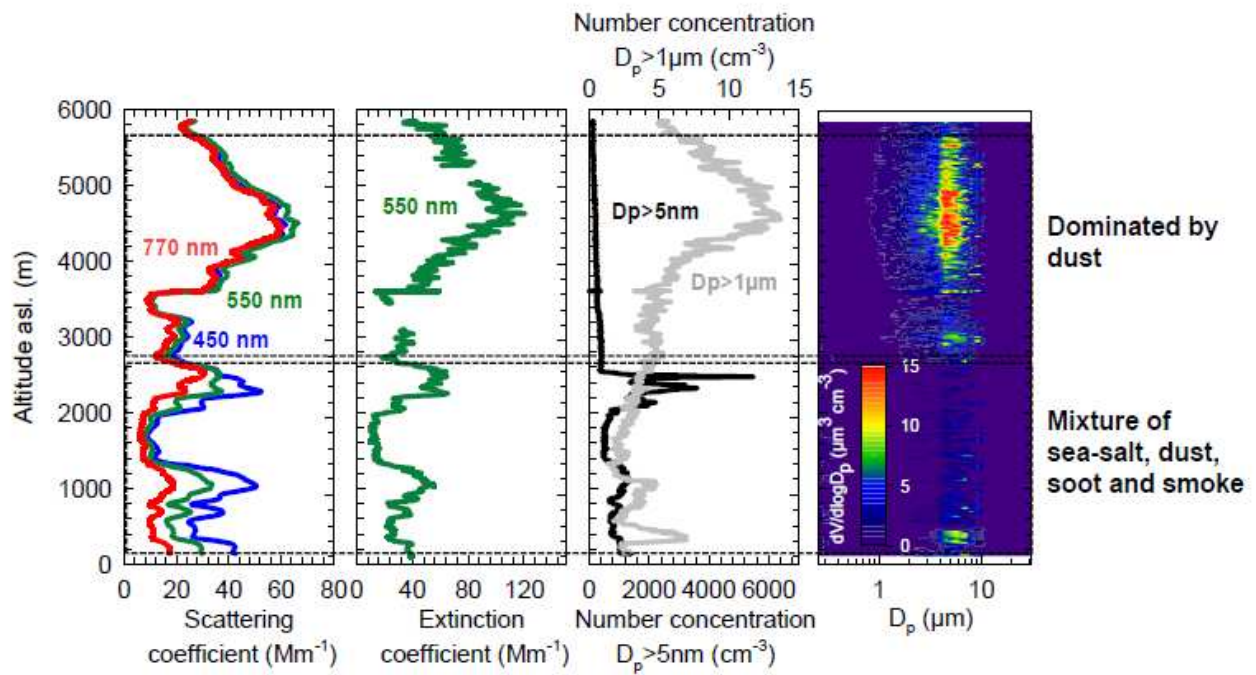
2392  
 2393  
 2394  
 2395  
 2396  
 2397  
 2398  
 2399  
 2400  
 2401  
 2402  
 2403  
 2404  
 2405  
 2406  
 2407  
 2408  
 2409  
 2410  
 2411  
 2412  
 2413  
 2414  
 2415  
 2416  
 2417  
 2418  
 2419

## SOP-1a AERONET/PHOTONS SSA



2420  
 2421  
 2422  
 2423  
 2424  
 2425  
 2426  
 2427  
 2428  
 2429  
 2430  
 2431  
 2432  
 2433  
 2434  
 2435  
 2436  
 2437  
 2438  
 2439  
 2440  
 2441  
 2442  
 2443  
 2444  
 2445  
 2446  
 2447  
 2448  
 2449  
 2450

**Figure 20.** AERONET/PHOTONS observations of the total single scattering albedo (SSA) at 440, 670, 880 and 1020 nm obtained for the whole SOP-1a period (the red curve represents the mean of observations).



2451  
 2452  
 2453  
 2454  
 2455  
 2456  
 2457  
 2458  
 2459  
 2460  
 2461  
 2462  
 2463  
 2464  
 2465  
 2466  
 2467  
 2468  
 2469  
 2470  
 2471  
 2472  
 2473  
 2474  
 2475  
 2476  
 2477  
 2478  
 2479  
 2480  
 2481  
 2482  
 2483  
 2484  
 2485  
 2486

**Figure 21.** Optical (scattering and extinction coefficients) and physical (number concentration and volume size distribution) aerosol properties estimated along the vertical onboard the ATR-42 aircraft for the flights 35-36 on 22 June over the Lampedusa station.

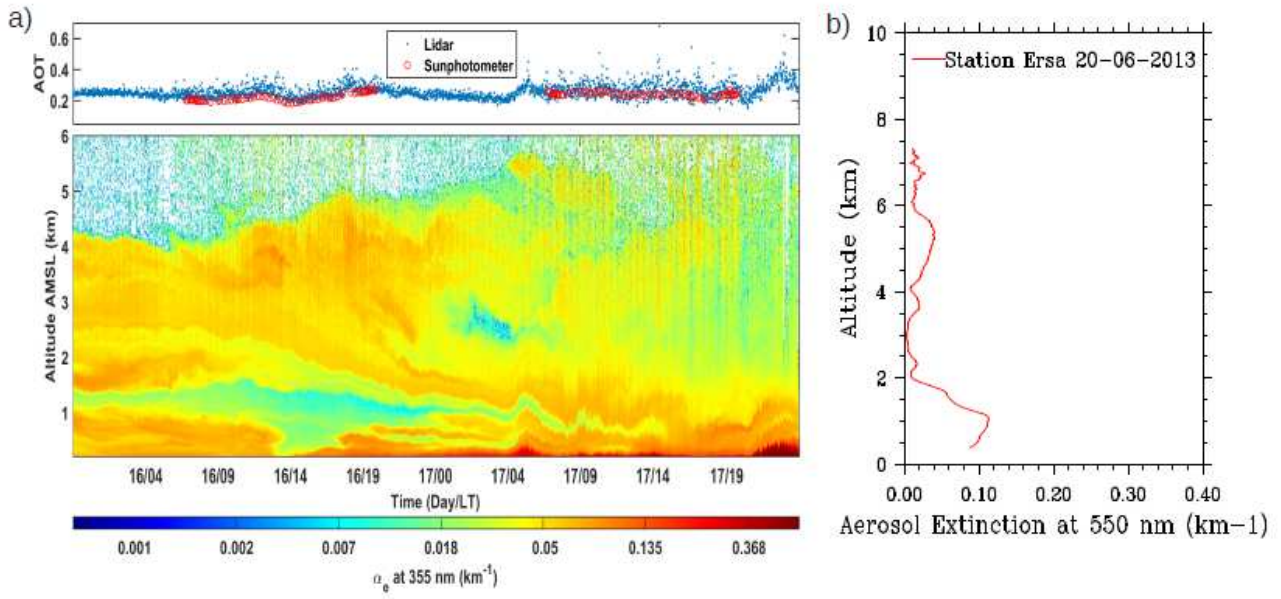


**Figure 22.** Minorca and Ersa lidar observations obtained during the dust plume of 16 to 17 June transported over the western Mediterranean basin.

2487  
 2488  
 2489  
 2490  
 2491  
 2492  
 2493  
 2494  
 2495  
 2496  
 2497  
 2498  
 2499  
 2500  
 2501  
 2502  
 2503  
 2504  
 2505  
 2506  
 2507  
 2508  
 2509  
 2510  
 2511  
 2512  
 2513  
 2514  
 2515  
 2516  
 2517  
 2518  
 2519  
 2520  
 2521  
 2522  
 2523  
 2524  
 2525  
 2526

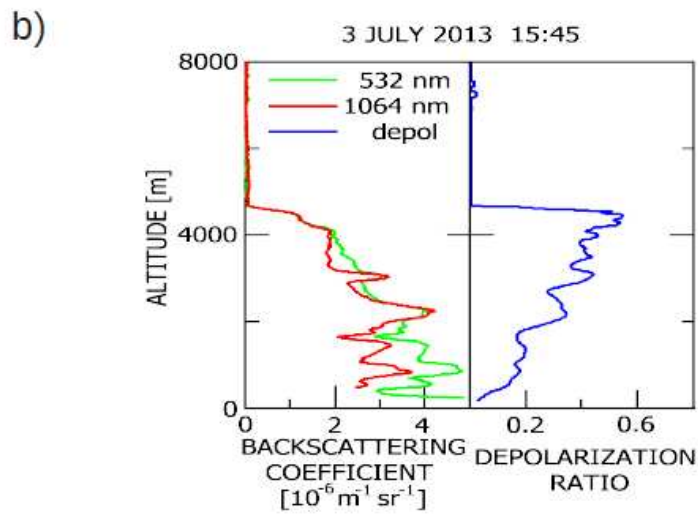
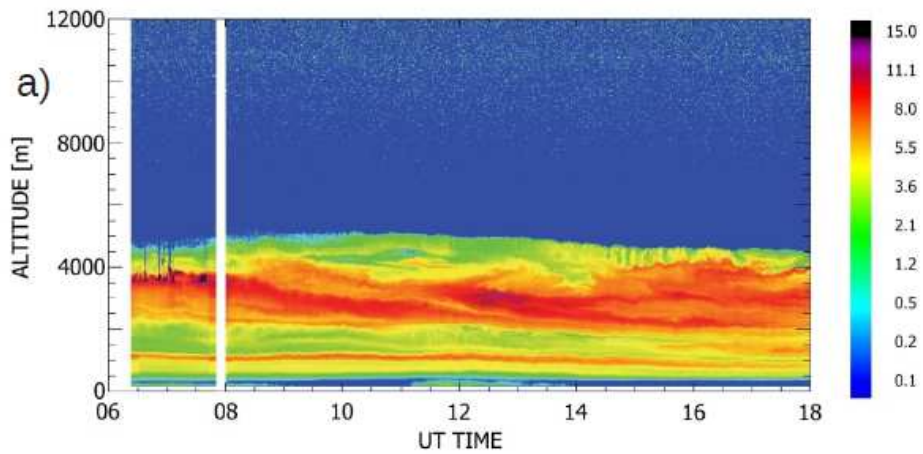


**Figure 23.** a) Time evolution of the vertical profile of the aerosol backscattering coefficient at 1064 nm at Lampedusa on 3 July 2013. The color scale is in units of  $10^{-7} \text{ m}^{-1} \text{ sr}^{-1}$ . b) Vertical profile of aerosol backscattering coefficient at two wavelengths and of aerosol depolarization ratio at 355 nm measured at Lampedusa on 3 July 2013 at 15:45 UT.

2527  
 2528  
 2529  
 2530  
 2531  
 2532  
 2533  
 2534  
 2535  
 2536  
 2537  
 2538  
 2539  
 2540  
 2541  
 2542  
 2543  
 2544  
 2545  
 2546  
 2547  
 2548  
 2549  
 2550  
 2551  
 2552

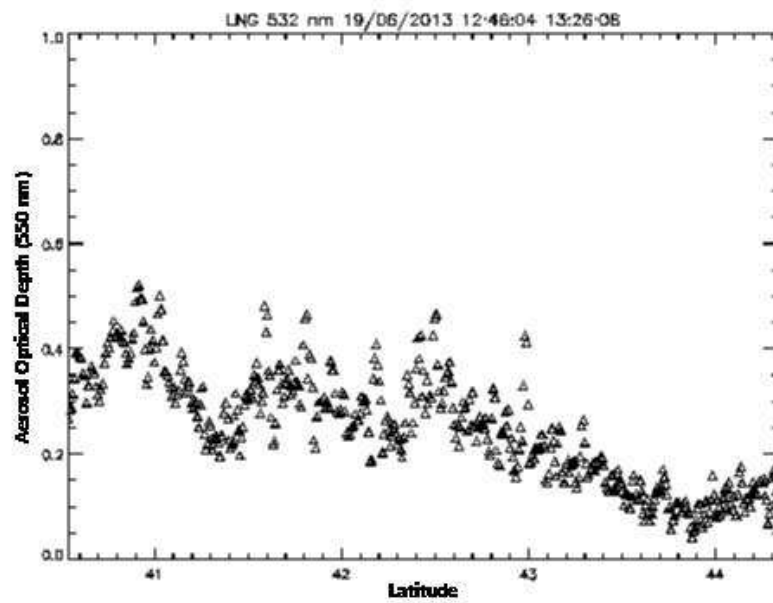
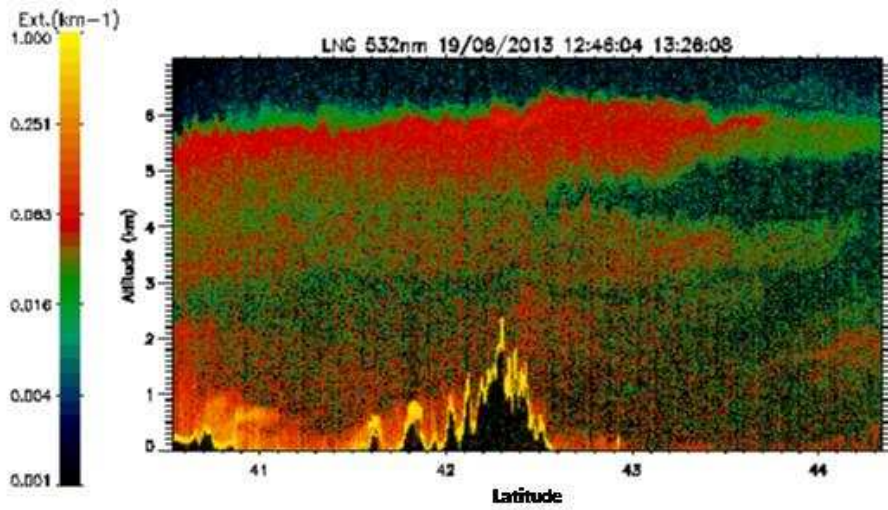
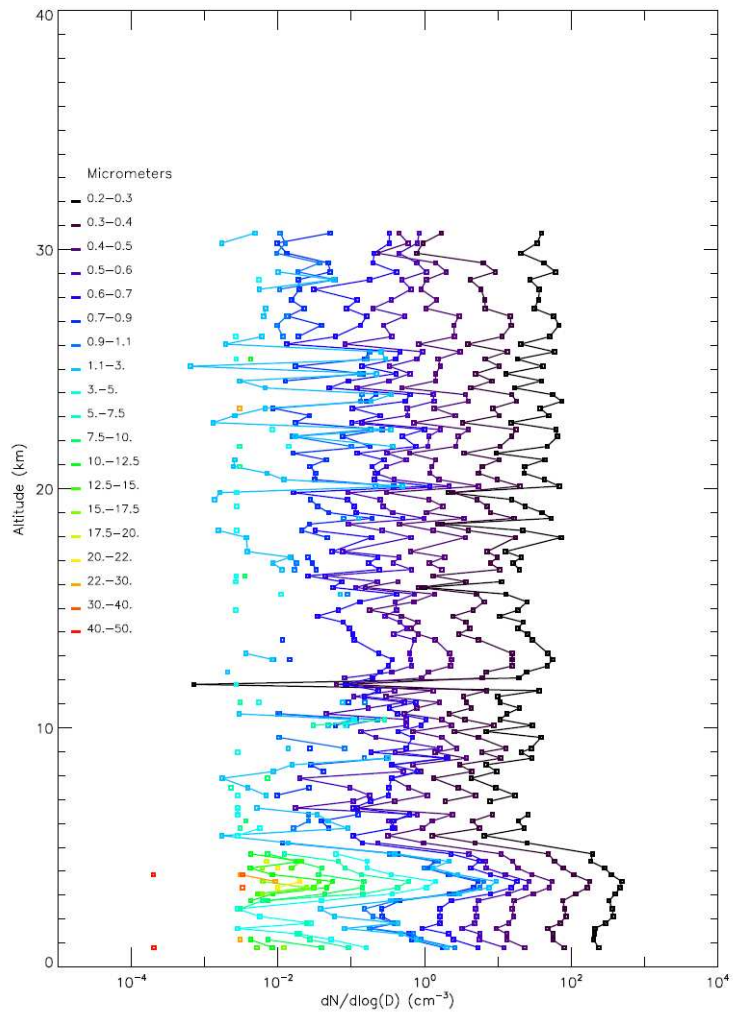


**Figure 24.** Observations of aerosol extinction coefficient (top, in  $\text{km}^{-1}$  at 532 nm) and aerosol optical depth (bottom) obtained from the lidar LNG system onboard the F-20 aircraft during the 19<sup>th</sup> of June that corresponds to the flight (12:46 to 13:26) from Cagliari to the Gulf of Genoa.

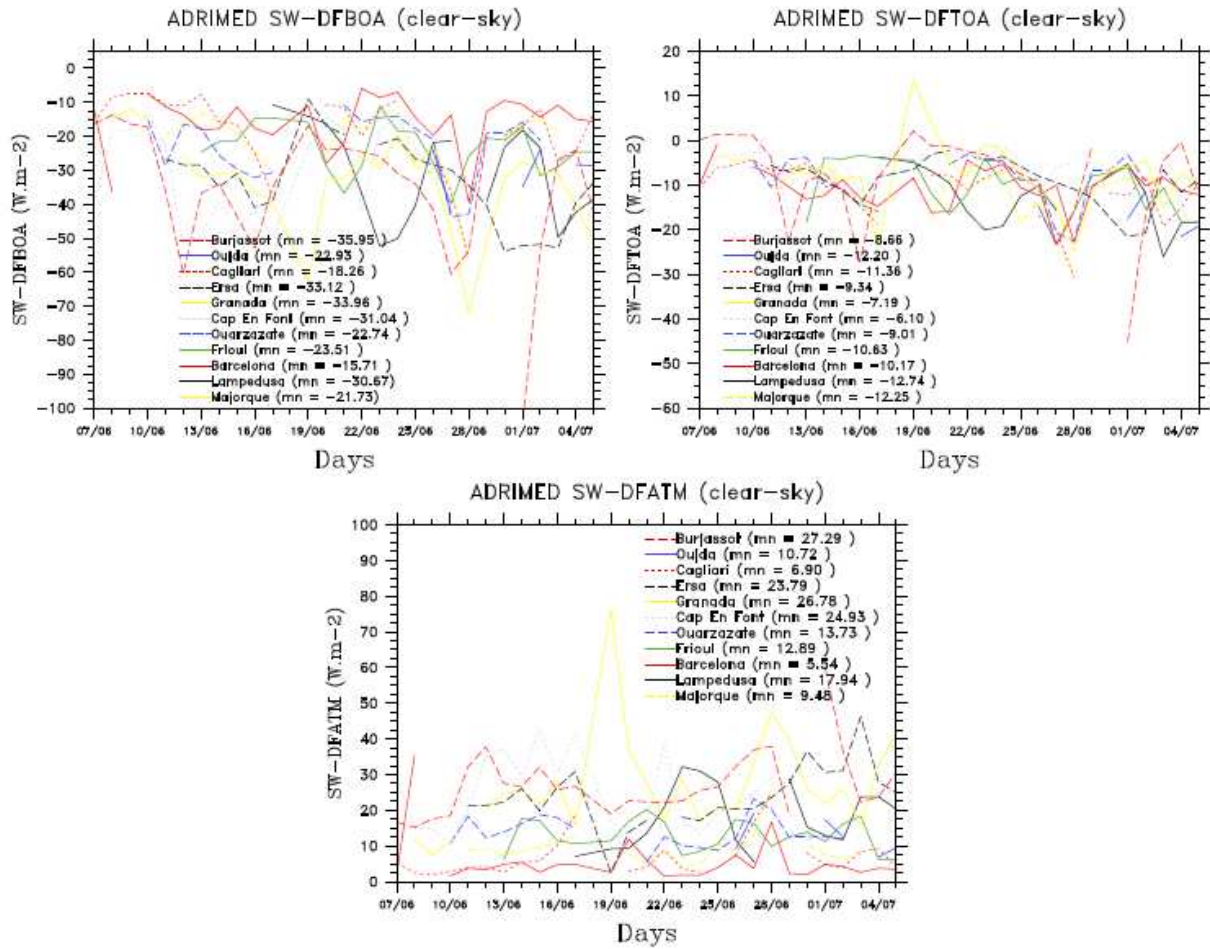
2553  
 2554  
 2555  
 2556  
 2557  
 2558  
 2559  
 2560  
 2561  
 2562  
 2563  
 2564  
 2565  
 2566  
 2567  
 2568  
 2569  
 2570  
 2571  
 2572  
 2573  
 2574



2575  
 2576  
 2577  
 2578  
 2579  
 2580  
 2581  
 2582  
 2583  
 2584  
 2585  
 2586  
 2587  
 2588  
 2589  
 2590  
 2591  
 2592  
 2593

**Figure 25:** Particle concentrations as a function of size and altitude in the troposphere and lower stratosphere from the LOAC flight under the meteorological balloon BLD9 launched from Minorca at the end of a dust event on 19 June 2013, 10:12 UT (Table 4; see the daytime averaged aerosol optical depth over the sea in Figure 6).





2594  
 2595  
 2596  
 2597  
 2598  
 2599  
 2600  
 2601  
 2602  
 2603  
 2604  
 2605  
 2606  
 2607  
 2608  
 2609  
 2610  
 2611  
 2612  
 2613  
 2614  
 2615  
 2616  
 2617  
 2618  
 2619

**Figure 26.** 1-D (clear-sky) instantaneous (shortwave only) DRF calculations (in  $W m^{-2}$ ) based on AERONET/PHOTONS dataset for the different stations listed in Table 2 (BOA, TOA and ATM refer to bottom of the atmosphere, top of atmosphere and atmospheric forcings).

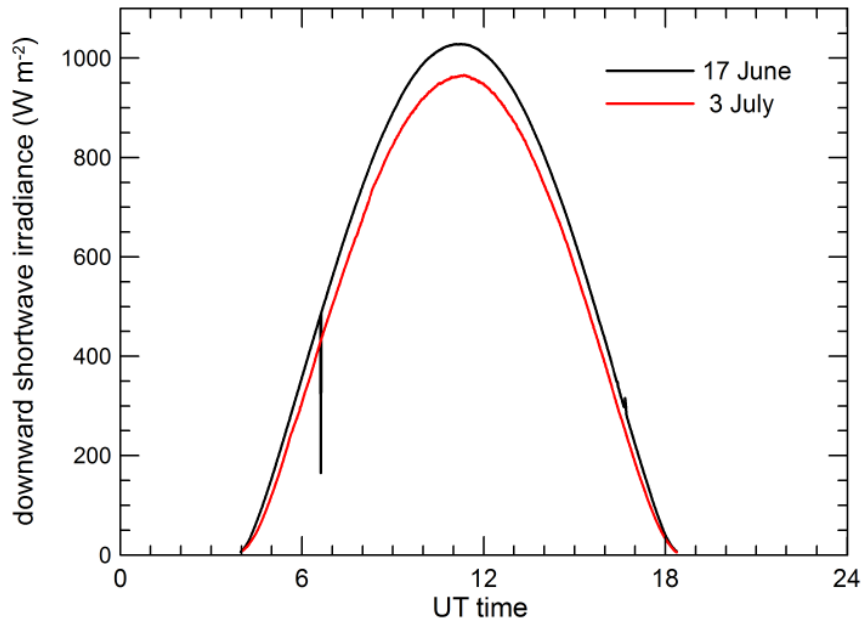


**Figure 27.** Time evolution of the downward solar irradiance observed at Lampedusa on 17 June and on 3 July, 2013.

2620  
 2621  
 2622  
 2623  
 2624  
 2625  
 2626  
 2627  
 2628  
 2629  
 2630  
 2631  
 2632  
 2633  
 2634  
 2635  
 2636  
 2637  
 2638  
 2639  
 2640  
 2641  
 2642  
 2643  
 2644  
 2645  
 2646  
 2647  
 2648  
 2649  
 2650  
 2651  
 2652  
 2653  
 2654  
 2655  
 2656  
 2657

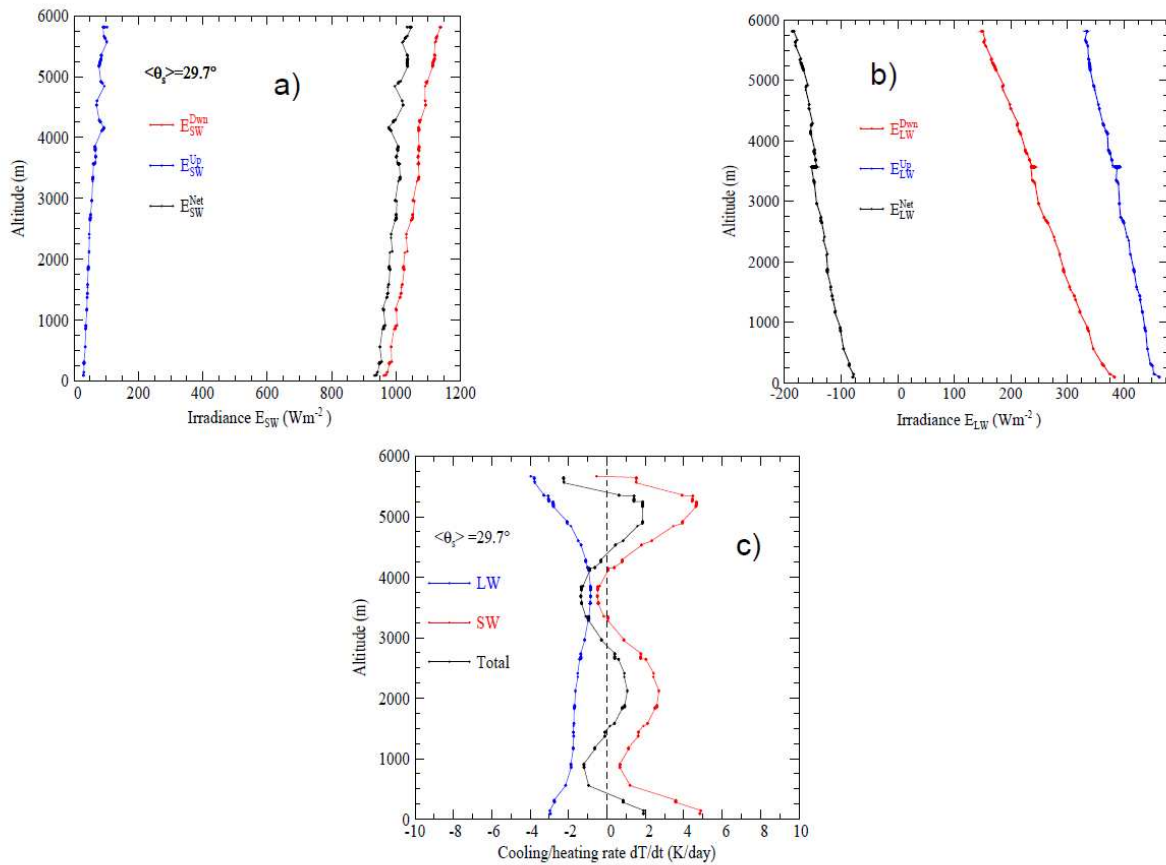
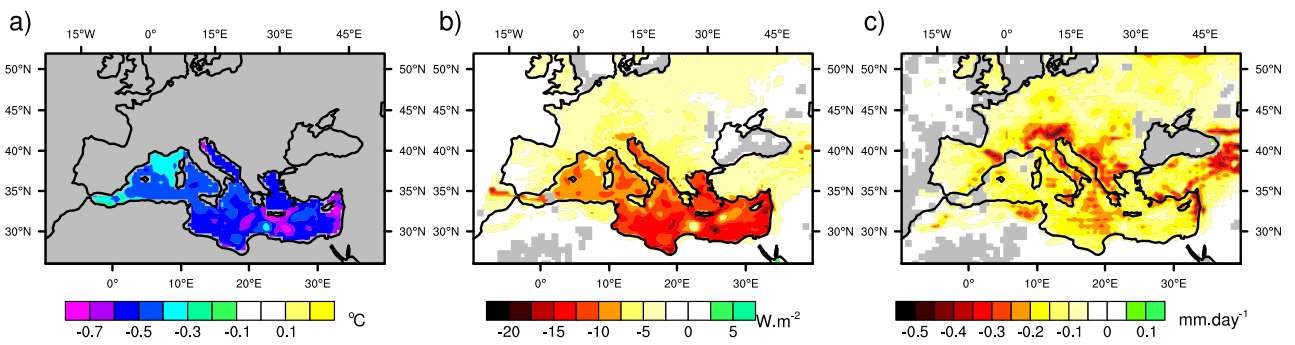


**Figure 28.** SW (a) and LW (b) upward and downward radiative fluxes observed over the Lampedusa station for the 22 June and estimated SW and LW heating rate (c) in the two spectral regions (see section 5.4.4 for details).

2658  
 2659  
 2660  
 2661  
 2662  
 2663  
 2664  
 2665  
 2666  
 2667  
 2668  
 2669  
 2670  
 2671  
 2672  
 2673  
 2674  
 2675  
 2676  
 2677  
 2678  
 2679  
 2680  
 2681  
 2682  
 2683  
 2684  
 2685  
 2686  
 2687



2688  
 2689  
 2690  
 2691  
 2692

**Figure 29.** Annual average difference in (a) Sea Surface Temperature (SST), latent heat loss (b) and precipitation (c) over the period 2003-2009 between a simulation ensemble including aerosols and a second one without any aerosol.

## Aerosol optical Depth (visible band)

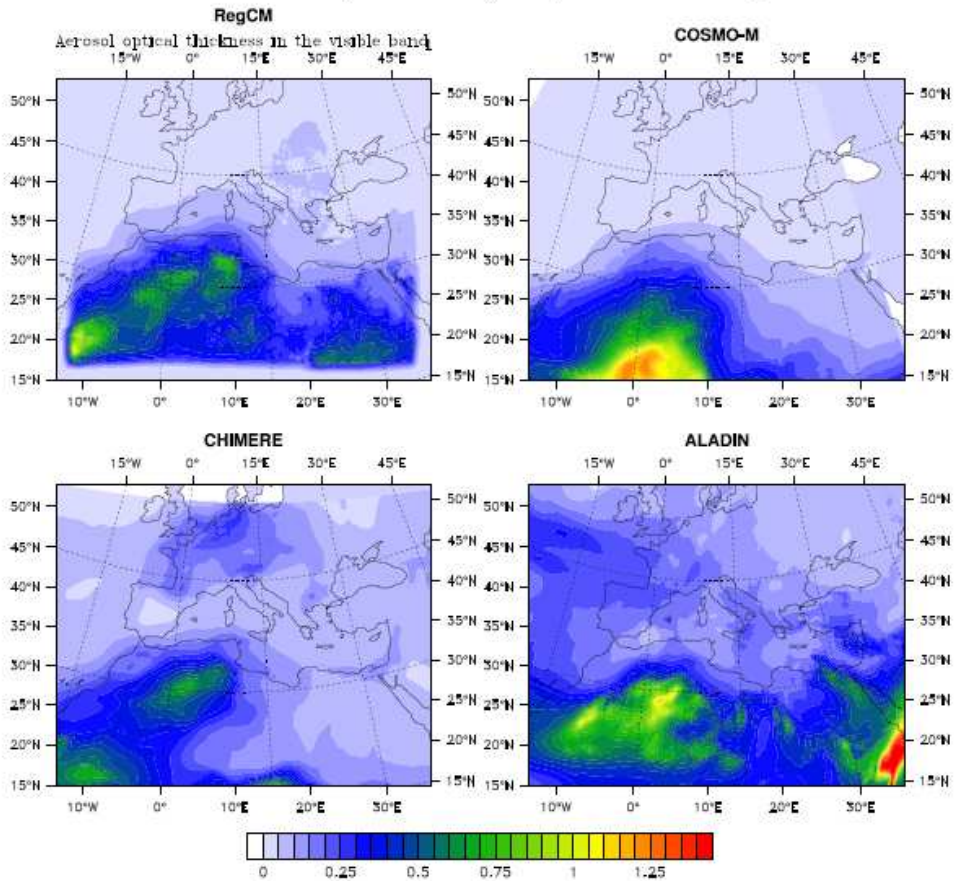


**Figure 30.** AOD averaged for the 15 to 25 June 2013 period from the meso-scale COSMO-MUSCAT (a), CTM-CHIMERE (b) models and the two regional climate models; CNRM-RCSM (c) and RegCM (d). Details about the model configurations are provided in Table 8.

2693  
 2694  
 2695  
 2696  
 2697  
 2698  
 2699  
 2700  
 2701  
 2702  
 2703  
 2704  
 2705  
 2706  
 2707  
 2708  
 2709  
 2710  
 2711  
 2712  
 2713  
 2714  
 2715  
 2716  
 2717  
 2718  
 2719  
 2720  
 2721

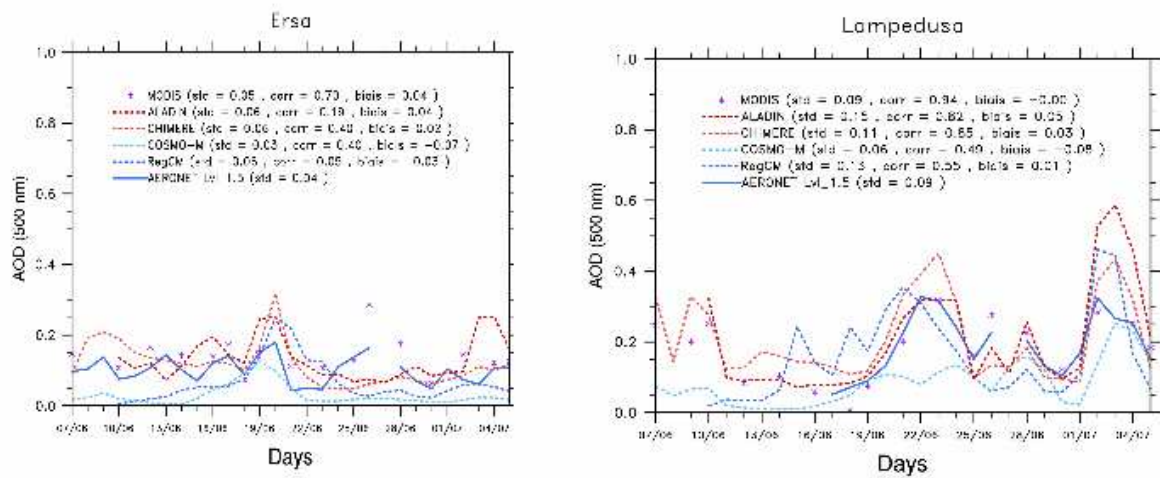
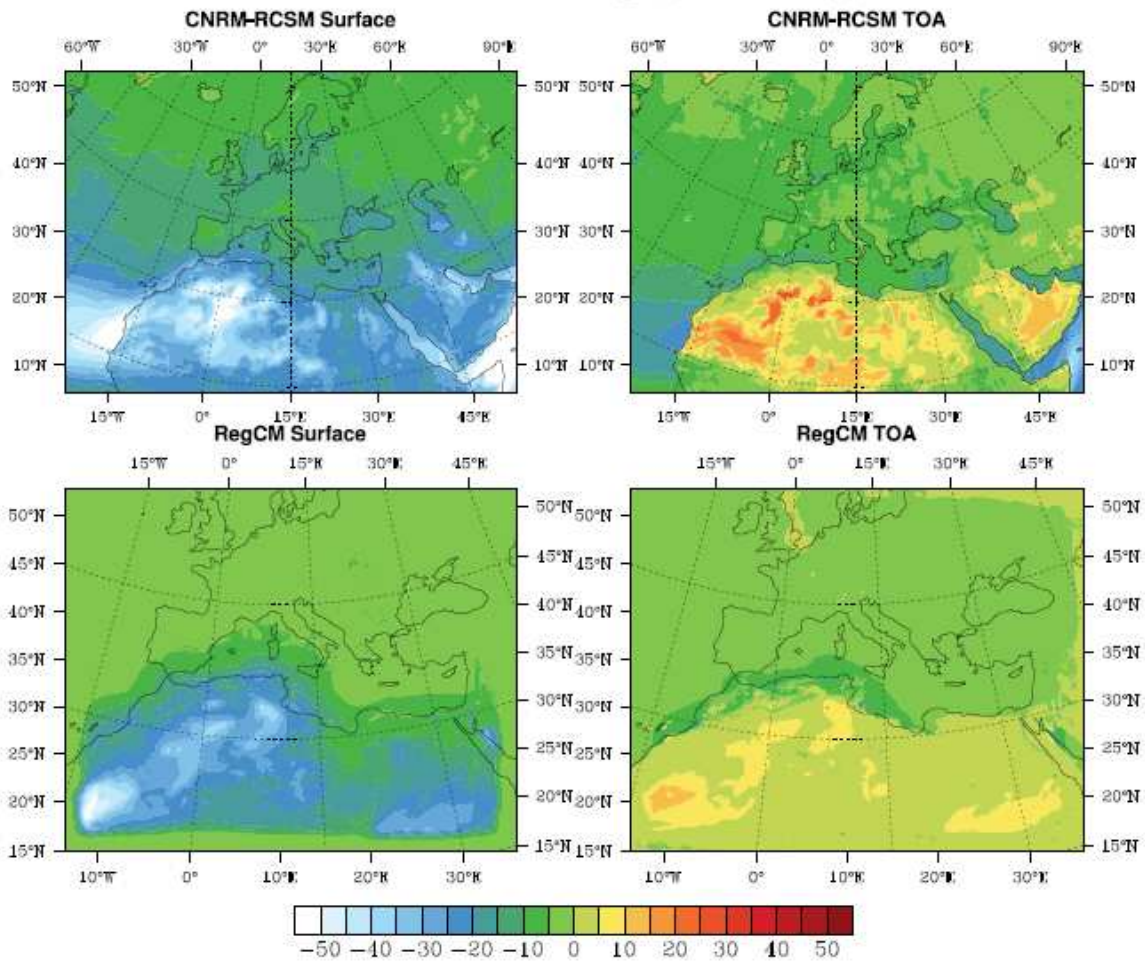


**Figure 31.** Times-series of AOD comparisons between AERONET/PHOTONS observations and COSMO-MUSCAT, CHIMERE, CNRM-RCSM and RegCM model outputs over the two stations of Ersa and Lampedusa. The MODIS retrievals are also reported.

2722  
 2723  
 2724  
 2725  
 2726  
 2727  
 2728  
 2729  
 2730  
 2731  
 2732  
 2733  
 2734  
 2735  
 2736  
 2737  
 2738  
 2739  
 2740  
 2741  
 2742  
 2743  
 2744  
 2745  
 2746  
 2747  
 2748  
 2749  
 2750  
 2751  
 2752  
 2753  
 2754  
 2755  
 2756

## SW Direct Radiative Forcing (clear-sky) SOP-1a



2757  
 2758  
 2759  
 2760  
 2761  
 2762  
 2763  
 2764

**Figure 32.** Averaged surface and TOA SW DRF simulated in clear-sky conditions and over the SOP-1a period by the CNRM-RCSM and RegCM models.

	<b>Ersa</b>		<b>Lampedusa</b>	
	Instruments	Frequency	Instruments	Frequency
Number concentration	1 CPC (0.01 - 3 $\mu\text{m}$ )	continuous (1')	1 W-CPC (0.01 - 3 $\mu\text{m}$ )	continuous (2')
CCN concentration	1 CCN counter	continuous	1 CCN counter	continuous
Mass concentration	1 PM2.5	continuous	1 PM40 (TEOM)	continuous
	1 PM10	continuous		
Number size distribution	1 OPC (0.3 - 5 $\mu\text{m}$ )	continuous	2 GRIMM (0.25 - 32 $\mu\text{m}$ )	continuous
	1 APS (TSI)	continuous	1 APS (TSI) (0.5 - 20 $\mu\text{m}$ )	continuous
	1 SMPS (3 - 300 nm)	continuous	2 (dry/ambient) SMPS	continuous
Mass size distribution	2 Impactor DEKATI (13 stages)	48h	2 Impactor DEKATI (13 stages)	48h
			1 Impactor Nano-MOUDI	24 h
PM1 composition	1 PILS	continuous	AMS (Aerodyne)	continuous
			1 PILS	continuous
PM10 composition			1 FAI Hydra Sampler	12h
Mass BC concentration	1 (7- $\lambda$ ) aethalometer	continuous	1 PSAP	continuous (1h)
			1 MAAP	continuous
Vertical Profiles	1 (1- $\lambda$ 355 nm) Leosphere	continuous	1 (1- $\lambda$ ) Leosphere ALS 300	continuous (20')
			2 (3-l) ENEA/Univ. of Rome lidar	continuous (1')
			microwave radiometer (p, T, RH)	continuous (15')
			radiosondes	on event
Scattering coefficient	1 (3- $\lambda$ ) TSI nephelometer (450-550-700 nm)	continuous (1')	1 (3- $\lambda$ ) TSI nephelometer (450-550-700 nm)	continuous (1')
Absorbing coefficient	1 (7- $\lambda$ ) aethalometer (370-420-490-520-660-880-950 nm)	continuous	1 (7- $\lambda$ ) aethalometer (370-420-490-520-660-880-95 nm)	continuous
Extinction coefficient	1 (1- $\lambda$ ) (860 nm) PAX	continuous (1')		
Column optical properties	1 (9- $\lambda$ ) AERONET/PHOTONS	continuous (15' for AOD)	1 (9- $\lambda$ ) AERONET/PHOTONS	continuous (15' for AOD)
			2 (12-l) MFRSRs	continuous (15 s)
Mineral Aerosol Deposition	1 CARAGA	continuous (7-days)	1 CARAGA	continuous (7-days)
Downward shortwave irradiance	1 pyranometer	continuous (30 s)	1 (CMP 21) pyranometer	continuous (30 s)
Downward longwave irradiance	1 pyrgeometer	continuous (30 s)	1 (CGR4) pyrgeometer	continuous (30 s)
Downward window (8-14 $\mu\text{m}$ ) irradiance			1 modified CG3 pyrgeometer	continuous (60 s)
Direct Solar radiance			1 CHP1 Pyrheliometer	continuous (30 s)
Direct spectral solar radiation			1 PMOD Precision SpectroRad.	Continuous (30 s)
Spectral downward global solar irradiance			1 HyperOCR spectrometer	continuous (30 s)



Spectral downward diffuse solar irradiance	1 HyperOCR spectrometer	continuous (30 s)
Spectral direct solar irradiance	1 spectroradiometer	continuous (60 s)
Downward spectral actinic flux	1 Diode array spectrometer	continuous (60s)

**Table 1.** List of the Instrumentations deployed over the two super-sites (Ersa and Lampedusa) during the SOP-1a experiment for the characterization of physical, chemical and optical properties of aerosols, vertical profiles, columnar-averaged properties and radiation measurements. Meteorological parameters and gas concentrations are not included in this table.

AERONET/PHOTONS Site Name	Latitude (°N)	Longitude (°E)	Altitude (m)	# wavelengths	Site characteristics
Modena	44.63	10.94	56	7	Urban
Avignon	43.93	4.87	32	4	Rural
Villefranche-sur-Mer	43.68	7.33	130	4	Peri-urban coastal
Frioul	43.26	5.29	40	8	Peri-urban coastal
Toulon	43.13	6.00	50	4	Urban coastal
Ersa	43.00	9.35	80	8	Remote island
Rome Tor Vergata	41.84	12.65	130	7	Peri-urban
Barcelone	41.38	2.17	125	4	Urban coastal
IMAA-Potenza	40.60	15.72	820	8	Urban
Lecce University	40.33	18.11	30	7	Peri-urban coastal
Cap d'en Font	39.82	4.21	10	7	Remote Island
Oristano	39.91	8.5	10	4	Peri-urban coastal
Burjassot	39.50	-0.42	30	8	Urban coastal
Majorque	39.55	2.62	10	7	Peri-urban coastal
Cagliari	39.28	9.05	3	7	Urban coastal
Messina	38.20	15.57	15	4	Urban coastal
Granada	37.16	-3.6	680	7	Urban
Malaga	36.71	-4.47	40	7	Peri-urban
Blida	36.50	2.88	230	7	Rural coastal
Lampedusa	35.51	12.63	45	7	Remote Island
Ouijda	34.65	1.90	620	8	Urban coastal
Ouarzazate	30.93	6.91	1136	8	Remote desert

**Table 2.** List of the long-term AERONET/PHOTONS sun-photometer stations operated in the western Mediterranean during the ChArMEx/ADRIMED (SOP-1a) experiment.

Parameter measured	Instrument	Abreviation	Location in the aircraft	Wavelength (nm)	Nominal size range ( $\mu\text{m}$ )
Size distribution	Forward Scattering Spectrometer Probe, Model 300, Particle Measuring Systems	FSSP-300	wing-mounted	632.8	0.28-20
	Ultra High Sensitivity Aerosol Spectrometer, Droplet Measurement Technologies	UHSAS	wing-mounted	1054	0.04-1
	Sky-Optical Particle Counter, Model 1.129, Grimm Technik	GRIMM1	AVIRAD inlet	655	0.25-32
	Optical Particle Counter, Model 1.109, Grimm Technik	GRIMM2	Communautory aerosol inlet	655	0.25-32
	Optical Particle Counter, Model 1.109, Grimm Technik	GRIMM3	Communautory aerosol inlet	655	0.25-32
	Scanning mobility particle sizer, custom-built (Villani et al., 2007)	SMPS	Communautory aerosol inlet	n/a	0.03-0.4
Integrated number concentration	Condensation Particle Counters, Model 3075, TSI	CPC	AVIRAD inlet	n/a	> 0.005
Scattering coefficient	$3\lambda$ Integrated Nephelometer, Model 3563, TSI	Nephelometer	AVIRAD inlet	450, 550, 700	n/a
Absorption coefficient	$3\lambda$ Particle Soot Absorption Photometer, Radiance Research	PSAP	Communautory aerosol inlet	467, 530, 660	n/a
Extinction coefficient	Cavity Attenuated Phase Shift, Aerodyne Research Inc.	CAPS	Communautory Aerosol inlet	530	n/a
	Photomètre Léger Aéroporté pour la Surveillance des Masses d'Air	PLASMA	roof-mounted	340-2250	n/a
Chemical composition	Filter sampling	n/a	AVIRAD inlet	n/a	n/a
	Single particle soot photometer, Droplet Measurement Technologies	SP2	Communautory aerosol inlet	1064	0.08-0.5

**Table 3.** In-situ instrumentation deployed onboard the ATR-42 during the SOP-1a experiment.



No.	Date (2013)	Start time (UTC)	Ceiling altitude (m)	Latitude at ceiling	Longitude at ceiling	Sensors
BLD1	12 June	21:13	21178	39.5156°N	04.3010°E	T, U
BLD2	15 June	21:40	32119	39.9903°N	04.1801°E	T, U, LOAC, O <sub>3</sub>
BLD3	16 June	10:29	31880	40.0527°N	04.1524°E	T, U, LOAC, O <sub>3</sub>
BLD4	16 June	21:13	33390	40.0999°N	04.0118°E	T, U, LOAC, O <sub>3</sub>
BLD5	17 June	10:01	32744	40.2109°N	03.9672°E	T, U, LOAC, O <sub>3</sub>
BLD6	17 June	18:25	33411	40.2502°N	03.9402°E	T, U, LOAC, O <sub>3</sub>
BLD7	18 June	16:34	35635	40.5832°N	04.0515°E	T, U, LOAC
BLD8	18 June	21:17	21507	40.6372°N	04.4889°E	T, U, LOAC, O <sub>3</sub>
BLD9	19 June	10:12	30902	40.6794°N	04.3691°E	T, U, LOAC, O <sub>3</sub>
BLD10	19 June	13:48	36129	40.6553°N	04.1970°E	T,U, LOAC
BLD11	27 June	09:43	35832	39.7546°N	04.4746°E	T,U, LOAC
BLD12	28 June	05:36	36293	39.4505°N	04.1709°E	T,U, LOAC
BLD13	29/30 June	23:31	36310	39.6168°N	03.7383°E	T,U, LOAC
BLD14	30 June	14:03	36319	39.8937°N	03.9568°E	T,U, LOAC
BLD15	02 July	10:27	32833	39.9942°N	04.2996°E	T, U, LOAC, O <sub>3</sub>

**Table 4.** Characteristics of the 15 sounding balloon flights from Sant Lluís, Minorca Island, during the ChArMEx SOP1a/ADRIMED campaign.

Date and time of launch (UT)	Balloon Nbr and type of sensor	Last data time (UT)	Last data location	Trajectory length (km)	Flight duration (h)	Approximate float altitude (m)
16 June, 09:46	B74, LOAC	16 June, 21:51	43.0265°N 05.2285°E	368	11:57	2100
16 June, 09:53	B53, O3	17 June, 00:26	40.6541°N 06.2398°E	203	14:28	3000-3050
16 June, 09:58	B70, LOAC	16 June, 23:01	40.1825°N 06.1293°E	174	13:17	3050-3150
17 June, 09:27	B54, O3	17 June, 16:49	43.1433°N 03.5293°E	371	07:22	1850-2000
17 June, 09:29	B75, LOAC	17 June, 16:51	43.0868°N 03.6866°E	365	07:23	1950-2050
17 June, 11:07	B72, LOAC	17 June, 19:07	43.2333°N 04.7403°E	382	08:03	2750
19 June, 10:34	B77, LOAC	19 June, 17:59	43.1576°N 04.7562°E	387	07:37	2550
19 June, 10:35	B71, LOAC	19 June, 15:03	43.0560°N 05.1336°E	369	04:39	3250-3350
27 June, 10:00	B80, LOAC	28 June, 12:07	37.9165°N 12.1605°E	759	26:19	2950-3050
28 June, 05:20	B73, LOAC	28 June, 17:24	37.4095°N 09.2346°E	523	12:16	2650-2750
02 July, 13:03	B76, LOAC	03 July,, 09:38	37.8897°N 12.1312°E	731	20:39	3150-3250
02 July, 13:11	B57, O3	03 July, 22:43	35.0900°N 14.1140°E	1053	33:44	3100-3200
02 July, 17:59	B55, O3	04 July, 02:20	37.3545°N 12.21980E	762	32.32	2400-2450
02 July, 17:50	B78, LOAC	04 July, 02:13	37.5639°N 12.1507°E	755	32.25	2350-2450

**Table 5.** Characteristics of the 14 BPCL drifting balloon flights.

	Ersa	Ersa corrected	Lampedusa	Cagliari	Cap d'En Font
Number of observations	25		18	20	17
$r_{vf}$ ( $\mu\text{m}$ )	$0.16 \pm 0.02$	#	$0.14 \pm 0.01$	$0.15 \pm 0.03$	$0.17 \pm 0.03$
$\sigma_f$	$0.43 \pm 0.03$	#	$0.50 \pm 0.06$	$0.46 \pm 0.04$	$0.45 \pm 0.04$
$r_{vc}$ ( $\mu\text{m}$ )	$2.49 \pm 0.43$	#	$2.36 \pm 0.48$	$2.52 \pm 0.28$	$2.48 \pm 0.30$
$\sigma_c$	$0.69 \pm 0.03$	#	$0.68 \pm 0.05$	$0.71 \pm 0.04$	$0.71 \pm 0.04$
$C_{vf}$ ( $\mu\text{m}^3/\mu\text{m}^2$ )	$0.02 \pm 0.01$	#	$0.02 \pm 0.01$	$0.02 \pm 0.01$	$0.02 \pm 0.01$
$C_{vc}$ ( $\mu\text{m}^3/\mu\text{m}^2$ )	$0.03 \pm 0.01$	0.04	$0.08 \pm 0.05$	$0.05 \pm 0.03$	$0.04 \pm 0.03$

**Table 6.** Main aerosol volume size distribution characteristics:  $r_{vf}$  ( $\mu\text{m}$ ),  $\sigma_f$ ,  $r_{vc}$  ( $\mu\text{m}$ ),  $\sigma_c$ ,  $C_{vf}$ ,  $C_{vc}$ , for the four different AERONET/PHOTONS stations: Ersa, Lampedusa, Cagliari and Cap d'En Font.  $C_{vi}$  denotes the particle volume concentration,  $r_{vi}$  is the median radius, and  $\sigma_i$  is the standard deviation. Each average value in the table is accompanied by its standard deviation (this is not an accuracy of the retrieval). As mentioned in the text, the concentration of the coarse mode at Ersa has been corrected to be comparable to results at other stations closer to the sea surface, using the logarithmic law proposed by Piazzola et al. (2015).

Models	Time of simulation	Horizontal resolution	Number of vertical layers	Aerosol species	Boundary Layer Forcing	Radiative transfer code
CHIMERE	01/06 31/07	- 50 km	20	Dust, Sea Salt, Secondary organic and inorganic, primary OC-BC	WRF	FastJX
CNRM-RCSM	01/06 31/07	- 50 km	31	Dust, Sea-Salt, Sulphates, primary OC-BC	ERA-Interim	SW: FMR (6 bands, Morcrette et al., 1989) LW: RRTM (Mlawer et al., 1997)
RegCM	13/06 05/07	- 25 km	23	Dust, Sea-Salt, Secondary inorganic, primary OC-BC	NCEP reanalysis	CCM3 or RRTM
COSMO-MUSCAT	15/05-31/07	28 km	40	Dust	GME	Ritter & Geleyn (1992)

**Table 7.** Main characteristics (period of simulations, horizontal resolution, number of vertical layers, main aerosol (primary and/or secondary) species, radiative transfer codes) of the four different 3-D models used during the SOP-1a experiment (see part. 6) (GME is for the global model of the German Weather Service).



## References

- Alados-Arboledas, L., Lyamani, H., Olmo, F.J. Aerosol size properties at Armilla, Granada (Spain), *Quarterly Journal of the Royal Meteorological Society*, 129 (590 PART A), pp. 1395-1413, 2003.
- Alados-Arboledas, L., Alcántara, A., Olmo, F.J., Martínez-Lozano, J.A., Estellés, V., Cachorro, V., Silva, A.M., Horvath, H., Gangl, M., Díaz, A., Pujadas, M., Lorente, J., Labajo, A., Sorribas, M., Pavese, G.: Aerosol columnar properties retrieved from CIMEL radiometers during VELETA 2002, *Atmos. Environ.*, 42, 2654-2667, 2008.
- Alados-Arboledas, L., et al.: Remote-sensing and in-situ characterization of atmospheric aerosol during ChArMEx/ADRIMED over Granada, in prep. for this special issue, 2015.
- Amiridis, V., Zerefos, C., Kazadzis, S., Gerasopoulos, E., Eleftheratos, K., Vrekoussis, M., Stohl, A., Mamouri, R.E., Kokkalis, P., Papayannis, A., Eleftheriadis, K., Diapouli, E., Keramitsoglou, I., Kontoes, C., Kotroni, V., Lagouvardos, K., Marinou, E., Giannakaki, E., Kostopoulou, E., Giannakopoulos, C., Richter, A., Burrows, J.P., Mihalopoulos, N.: Impact of the 2009 Attica wild fires on the air quality in urban Athens, *Atmos. Environ.* 46, 536–544, 2012.
- Ancellet, G., Pelon, J., Totems, J., Chazette, P., Bazureau, A., Sicard, M., Di Iorio, T., Dulac, F., and Mallet, M.: Mixing of aerosol sources during the North American biomass burning episode in summer 2013: analysis of lidar observations in the Mediterranean basin, *Atmos. Chem. Phys. Discuss.*, submitted to this special issue, 2015.
- Antón, M., Valenzuela, A., Mateos, D., Alados, I., Foyo-Moreno, I., Olmo, F. J., Alados-Arboledas, L.: Longwave aerosol radiative effects during an extreme desert dust event in southeastern Spain, *Atmos. Res.*, 148, 18-23, 2014.
- Baldassarre, G., Pozzoli, L., Schmidt, C. C., Unal, A., Kindap, T., Menzel, W. P., Whitburn, S., Coheur, P.-F., Kavgaci, A., and Kaiser, J. W.: Using SEVIRI fire observations to drive smoke plumes in the CMAQ air quality model: a case study over Antalya in 2008, *Atmos. Chem. Phys.*, 15, 8539-8558, doi:10.5194/acp-15-8539-2015, 2015.
- Balis, D.S., Amiridis, V., Nickovic, S., Papayannis, A., and Zerefos, C.: Optical properties of Saharan dust layers as detected by a Raman lidar at Thessaloniki, Greece, *Geophys. Res. Lett.*, 31, L13104, doi:10.1029/2004GL019881, 2004.
- Balis, D., Amiridis, V., Kazadzis, S., Papayannis, A., Tsaknakis, G., Tzortzakis, S., Kalivitis, N., Vrekoussis, M., Kanakidou, M., Mihalopoulos, N., Chourdakis, G., Nickovic, S., Pérez, C., Baldasano, J., and Drakakis, M.: Optical characteristics of desert dust over the East Mediterranean during summer: a case study, *Ann. Geophys.*, 24, 807-821, 2006.
- Barnaba, F., Angelini, F., Curci, G., and Gobbi, G. P.: An important fingerprint of wildfires on the European aerosol load, *Atmos. Chem. Phys.*, 11, 10487-10501, doi:10.5194/acp-11-10487-2011, 2011.
- Barragan, R., Sicard, M., Totems, J., Léon, J.-F., Renard, J.-B., Dulac, F., Mallet, M., Pelon, J., Alados-Arboledas, L., Amodeo, A., Augustin, P., Boselli, A., Bravo-Aranda, J. A., Burlizzi, P., Chazette, P., Comerón, A., D'Amico, G., Granados-Muñoz, M. J., Leto, G., Guerrero-Rascado, J. L., Madonna, F., Mona, L., Muñoz-Porcar, C., Pappalardo, G., Perrone, M. R., Pont, V., Rocadenbosch, F., Rodriguez, A., Scollo, S., Spinelli, N., Titos, G., Wang, X., and Zanmar Sanchez, R.: Characterization of aerosol transport and ageing during a multi-intrusion Saharan dust event over the western and central Mediterranean Basin in June 2013 in the framework of the ADRIMED/ChArMEx campaign, *Atmos. Chem. Phys.*, in prep. for this special issue, 2015.
- Berthier, S., Chazette, P., Couvert, P., Pelon, J., Dulac, F., Thieuleux, F., Moulin, C., and Pain, T.: Desert dust aerosol columnar properties over ocean and continental Africa from Lidar in-Space Technology Experiment (LITE) and Meteosat synergy, *J. Geophys. Res.*, 111, D21202, doi:10.1029/2005JD006999, 2006.
- Bessagnet, B., Hodzic, A., Vautard, R., Beekmann, M., Cheinet, S., Honoré, C., Liousse, C., and Rouil, L.: Aerosol modeling with CHIMERE: preliminary evaluation at the continental scale, *Atmos. Environ.*, 38, 2803–2817, 2004.
- Beuvier, J., Sevault, F., Herrmann, M., Kontoyiannis, H., Ludwig, W., Rixen, M., Stanev, E., Béranger, K., and Somot, S.: Modeling the Mediterranean Sea interannual variability during 1961–2000: Focus on the Eastern Mediterranean Transient, *J. Geophys. Res.*, 115, C08017, doi:10.1029/2009JC005950, 2010.
- Brauch, H.G.: Urbanization and natural disasters in the Mediterranean: Population growth and climate change in the 21<sup>st</sup> century, in *Building Safer Cities – The Future of Disaster Risk*, Edited by Kreimer, A., Arnold, M., and Carlin, A., The World Bank, Disaster Risk Management Series No.3, 149-164, 2003.
- Cachier, H., Aulagnier, F., Sarda, R., Gautier, F., Masclat, P., Besombes, J.L., Marchand, N., Despiiau, S., Croci, D., Mallet, M., Laj, P., Marinoni, A., Deveau, P.A., Roger, J.C., Putaud, J.P., Van Dingenen, R., Dell'Acqua, A., Viidanoja, J., Martins-Dos Santos, S., Liousse, C., Cousin, F., and Rosset, R.: Aerosol studies during the ESCOMPTE Experiment: an overview, *Atmos. Res.*, 74, 547-563, doi:10.1016/j.atmosres.2004.06.013, 2005.

- Cachorro, V. E., Toledano, C., Prats, N., Sorribas, M., Mogo, S., Berjon, A., Torres, B., Rodrigo, R., J. de la Rosa, and De Frutos, A.M.: The strongest desert dust intrusion mixed with smoke over the Iberian Peninsula registered with Sun photometry, *J. Geophys. Res.*, 113, D14S04, doi:10.1029/2007JD009582, 2008.
- Casasanta, G., di Sarra, A., Meloni, D., Monteleone, F., Pace, G., Piacentino, S., and Sferlazzo, D.: Large aerosol effects on ozone photolysis in the Mediterranean, *Atmos. Environ.*, 45, 3937-3943, doi:10.1016/j.atmosenv.2011.04.065, 2011.
- Chazette, P., and Lioussé, C.: A case study of optical and chemical ground apportionment for urban aerosols in Thessaloniki, *Atmos. Environ.*, 35, 2497-2506, doi:10.1016/S1352-2310(00)00425-8, 2001.
- Chazette, P., Marnas, F., and Totems, J.: The mobile Water vapor Aerosol Raman Lidar and its implication in the framework of the HyMeX and ChArMEx programs: application to a dust transport process, *Atmos. Meas. Tech.*, 7, 1629-1647, doi:10.5194/amt-7-1629-2014, doi:10.5194/amt-7-1629-2014, 2014a.
- Chazette, P., Marnas, F., Totems, J., and X. Shang, J.: Comparison of IASI water vapor retrieval with H<sub>2</sub>O-Raman lidar in the framework of the Mediterranean HyMeX and ChArMEx programs, *Atmos. Chem. Phys.*, 14, 9583-9596, doi:10.5194/acp-14-9583-2014, doi:10.5194/acp-14-9583-2014, 2014b.
- Chazette, P., Totems, J., Ancellet, G., Pelon, J., and Sicard, M.: Temporal consistency of lidar observables during aerosol transport events in the framework of the ChArMEx/ADRIMED campaign at Menorca Island in June 2013, *Atmos. Chem. Phys. Discuss.*, submitted to this special issue, 2015.
- Chenoweth J., Hadjinicolaou, P., Bruggeman, A., Lelieveld, J., Levin, Z., Lange, M. A., Xoplaki, E., and Hadzikakou, M.: Impact of climate change on the water resources of the eastern Mediterranean and middle east region: modeled 21st century, *Water Resour. Res.*, 47, W06506, doi:10.1029/2010WR010269, 2011.
- Ciardini, V., Di Iorio, T., Di Liberto, L., Tirelli, C., Casasanta, G., di Sarra, A., Fiocco, G., Fuà, D., and Cacciani, M.: Seasonal variability of tropospheric aerosols in Rome, *Atmos. Res.*, 118, 205-214, doi:10.1016/j.atmosres.2012.06.026, 2012.
- Claeys, M., Roberts, G., Mallet, M., Sciare, J., Sellegri, K., Sauvage, B., Tulet, P., Arndt, J.: Characterisation of a sea salt episode during ADRIMED campaign: ageing, transport and size distribution study, in prep. for this special issue, 2015.
- Collaud Coen, M., Weingartner, E., Schaub, D., Hueglin, C., Corrigan, C., Henning, S., Schwikowski, M., and Baltensperger, U.: Saharan dust events at the Jungfraujoch: detection by wavelength dependence of the single scattering albedo and first climatology analysis, *Atmos. Chem. Phys.*, 4, 2465-2480, 2004.
- Denjean, C., Chevaillier, S., Triquet, S., Grand, N., Cassola, F., Mazzino, A., Bourriane, T., Momboisse, G., Dupuy, R., Sellegri, K., Schwarzenbock, A., Mallet, M., and Formenti, P.: Size distribution and optical properties of mineral dust aerosols transported in the West Mediterranean, *Atmos. Chem. Phys. Discuss.*, 15, 21607-21669, 2015.
- Déqué, M. and Somot, S.: Extreme precipitation and high resolution with Aladin, *Idöjaras Quaterly Journal of the Hungarian Meteorological Service*, 112, 179-190, 2008.
- Derimian, Y., Karnieli, A., Kaufman, Y. J., Andreae, M. O., Andreae, T. W., Dubovik, O., Maenhaut, W., Koren, I., and Holben, B. N.: Dust and pollution aerosols over the Negev desert, Israel: Properties, transport, and radiative effect, *J. Geophys. Res.*, 111, D05205, doi:10.1029/2005JD006549, 2006.
- Deschamps, P.-Y., Bréon, F.-M., Leroy, M., Podaire, A., Bricaud, A., Buriez, J.C., and Sèze, G.: The POLDER mission: Instrument characteristics and scientific objectives, *IEEE Trans. Geosci. Remote Sens.*, 32, 598-615, 1994.
- Di Biagio, C., di Sarra, A., Meloni, D., Monteleone, F., Piacentino, S., and Sferlazzo, D.: Measurements of Mediterranean aerosol radiative forcing and influence of the single scattering albedo, *J. Geophys. Res.*, 114, D06211, doi:10.1029/2008JD011037, 2009.
- Di Biagio, C., di Sarra, A., and D. Meloni, D.: Large atmospheric shortwave radiative forcing by Mediterranean aerosol derived from simultaneous ground-based and spaceborne observations, and dependence on the aerosol type and single scattering albedo, *J. Geophys. Res.*, 115, D10209, doi:10.1029/2009JD012697, 2010.
- Di Iorio, T., Di Sarra, A., Junkermann, W., Cacciani, M., Fiocco, G., and Fuà, D.: Tropospheric aerosols in the Mediterranean: 1. Microphysical and optical properties, *J. Geophys. Res.*, 108, 4316, doi:10.1029/2002JD002815, 2003.
- Di Iorio, T., di Sarra, A., Sferlazzo, D. M., Cacciani, M., Meloni, D., Monteleone, F., Fuà, D., and Fiocco, G.: Seasonal evolution of the tropospheric aerosol vertical profile in the central Mediterranean and role of desert dust, *J. Geophys. Res.*, 114, D02201, doi:10.1029/2008JD010593, 2009.
- Di Iorio, T., Di Biagio, C., di Sarra, A., Formenti, P., Gomez Amo, J.-L., Meloni, D., and Pace, G.: Height resolved aerosol optical properties at Lampedusa during ADRIMED, in prep. for this special issue, 2015.
- di Sarra, A., Pace, G., Meloni, D., De Silvestri, L., Piacentino, S., and Monteleone, F.: Surface shortwave radiative forcing of different aerosol types in the central Mediterranean, *Geophys. Res. Lett.*, 35, L02714,

- doi:10.1029/2007GL032395, 2008.
- di Sarra, A., Di Biagio, C., Meloni, D., Monteleone, F., Pace, G., Pugnaghi, S., and Sferlazzo, D.: Shortwave and longwave radiative effects of the intense Saharan dust event of 25-26 March 2010 at Lampedusa (Mediterranean Sea), *J. Geophys. Res.*, 116, D23209, doi:10.1029/2011JD016238, 2011.
- di Sarra, A., Sferlazzo, D., Meloni, D., Anello, F., Bommarito, C., Corradini, S., De Silvestri, L., Di Iorio, T., Monteleone, F., Pace, G., Piacentino, S., and Pugnaghi, S.: Empirical correction of multi filter rotating shadowband radiometer (MFRSR) aerosol optical depths for the aerosol forward scattering and development of a long-term integrated MFRSR-Cimel dataset at Lampedusa, *Appl. Opt.*, 54, 2725-2737, doi:10.1364/AO.54.002725, 2015.
- Dubovik, O., and King, M. D.: A flexible inversion algorithm for retrieval of aerosol optical properties from Sun and sky radiance measurements, *J. Geophys. Res.*, 105, 20673–20696, doi:10.1029/2000JD900282, 2000.
- Dubovik, O., Smirnov, A., Holben, B. N., King, M. D., Kaufman, Y. J., Eck, T. F., and Slutsker, I.: Accuracy assessment of aerosol optical properties retrieval from AERONET Sun and sky radiance measurements, *J. Geophys. Res.*, 105, 9791–9806, doi:10.1029/2000JD900040, 2000.
- Dubovik, O., Holben, B., Eck, T.F., Smirnov, A., Kaufman, Y.J., King, M.D., Tanré, D., and Slutsker, I.: Variability of absorption and optical properties of key aerosol types observed in worldwide locations, *J. Atmos. Sci.*, 59, 590–608, doi:http://dx.doi.org/10.1175/1520-0469(2002)059<0590:VOAAOP>2.0.CO;2, 2002.
- Dubovik, O., Sinyuk, A., Lapyonok, T., Holben, B. N., Mishchenko, M., Yang, P., Eck, T. F., Volten, H., Muñoz, O., Veihelmann, B., van der Zande, W. J., Léon, J.-F., Sorokin, M., and Slutsker, I.: Application of spheroid models to account for aerosol particle nonsphericity in remote sensing of desert dust, *J. Geophys. Res.*, 111, D11208, doi:10.1029/2005JD006619, 2006.
- Dubovik, O., Herman, M., Holdak, A., Lapyonok, T., Tanré, D., Deuzé, J. L., Ducos, F., Sinyuk, A., and Lopatin, A.: Statistically optimized inversion algorithm for enhanced retrieval of aerosol properties from spectral multi-angle polarimetric satellite observations, *Atmos. Meas. Tech.*, 4, 975-1018, doi:10.5194/amt-4-975-2011, 2011.
- Dubuisson, P., Dessailly, D., Vesperini, M., and Frouin, R.: Water vapor retrieval over ocean using near-infrared radiometry, *J. Geophys. Res.*, 109, D19106, doi:10.1029/2004JD004516, 2004.
- Ducrocq, V., Braud, I., Davolio, S., Ferretti, R., Flamant, C., Jansa, A., Kalthoff, N., Richard, E., Taupier-Letage, I., Ayrat, P.A., Belamari, S., Berne, A., Borga, M., Boudevillain, B., Bock, O., Boichard, J.L., Bouin, M.N., Bousquet, O., Bouvier, C., Chiggiato, J., Cimini, D., Corsmeier, U., Coppola, L., Cocquerez, P., Defer, E., Delanoë, J., Delrieu, G., Di Girolamo, P., Doerenbecher, A., Drobinski, P., Dufournet, Y., Fourrié, N., Gourley, J.J., Labatut, L., Lambert, D., Le Coz, J., Marzano, F.S., Montani, A., Nuret, M., Ramage, K., Rison, B., Rousset, O., Saïd, F., Schwarzenboeck, A., Testor, P., Van Baelen, J., Vincendon, B., Aran, M., and Tamayo J.: HyMeX-SOP1, the Field Campaign Dedicated to Heavy Precipitation and Flash-Flooding in Northwestern Mediterranean. *Bull. Amer. Meteorol. Soc.*, 95, 1083-1100, doi: 10.1175/BAMS-D-12-00244.1 and doi: 10.1175/BAMS-D-12-00244.2, 2014.
- Dulac, F., and Chazette, P.: Airborne study of a multi-layer aerosol structure in the eastern Mediterranean observed with the airborne polarized lidar ALEX during a STAAARTE campaign (7 June 1997), *Atmos. Chem. Phys.*, 3, 1817-1831, 2003.
- Eleftheriadis, K., Colbeck, I., Housiadaa, C., Lazaridis, M., Mihalopoulos, N., Mitsakou, C., Smolik, J., and Zdimal, V.: Size distribution, composition and origin of the submicron aerosol in the marine boundary layer during the eastern Mediterranean “SUB-AERO” experiment, *Atmos. Environ.*, 40, 6245–6260, 2006.
- Foltz, G.R., and McPhaden, M.J., Impact of Saharan dust on tropical North Atlantic SST, *J. Climate*, 21, 5048-5060, doi: http://dx.doi.org/10.1175/2008JCLI2232.1, 2008.
- Formenti, P., Boucher, O., Reiner, T., Sprung, D., Andreae, M. O., Wendisch, M., Wex, H., Kindred, D., Tzortziou, M., Vasaras, A., and Zerefos, C.: STAAARTE-MED 1998 summer airborne measurements over the Aegean Sea, 2. Aerosol scattering and absorption, and radiative calculations, *J. Geophys. Res.* 107, 4451, doi:10.1029/2001JD001536, 2002.
- Formenti, P., et al.: Characterisation of aerosols in a remote marine atmosphere in the West Mediterranean, *Atmos. Chem. Phys. Discuss.*, in prep. for this special issue, 2015.
- Fotiadi, A., Hatzianastassiou, N., Drakakis, E., Matsoukas, C., Pavlakis, K.G., Hatzidimitriou, D., Gerasopoulos, E., Mihalopoulos, N., and Vardavas, I.: Aerosol physical and optical properties in the Eastern Mediterranean Basin, Crete, from Aerosol Robotic Network data, *Atmos. Chem. Phys.*, 6, 5399–5413, doi:10.5194/acp-6-5399-2006, 2006.
- Gangoiti, G., Millán, M., Salvador, R., and Mantilla, E.: Long-range transport and re-circulation of pollutants in the western Mediterranean during the project Regional Cycles of Air Pollution in the West-Central Mediterranean Area, *Atmos. Environ.*, 35, 6267-6276, doi:10.1016/S1352-2310(01)00440-X, 2001.
- Garcia, O. E., Diaz, J. P., Exposito, F. J., Diaz, A. M., Dubovik, O., Derimian, Y., Dubuisson, P., and Roger, J.-C.:

- Shortwave Radiative Forcing and Efficiency of Key Aerosol Types using AERONET Data, *Atmos. Chem. Phys.*, 12, 5129-5145, doi:10.5194/acp-12-5129-2012, 2012.
- García-Ruiz, J. M., López-Moreno, J. I., Vicente-Serrano, S. M., Lasanta-Martínez, T., and Beguería, S.: Mediterranean water resources in a global change scenario, *Earth-Sci. Rev.*, 105, 121-139, doi:10.1016/j.earscirev.2011.01.006, 2011.
- Gard, E., Mayer, J. E., Morrical, B. D., Dienes, T., Fergenson, D. P., and Prather, K.A.: Real-time analysis of individual atmospheric aerosol particles: Design and performance of a portable ATOFMS, *Anal. Chem.*, 69, 4083-4091, doi:10.1021/ac970540n, 1997.
- Gerasopoulos, E., Andreae, M.O., Zerefos, C.S., Andreae, T.W., Balis, D., Formenti, P., Merlet, P., Amiridis, V., and Papastefanou, C.: Climatological aspects of aerosol optical properties in Northern Greece, *Atmos. Chem. Phys.*, 3, 2025-2041, doi:10.5194/acp-3-2025-2003/, 2003.
- Gheusi, F., Durand, P., Verdier, N., Dulac, F., Attié, J.-L., Commun, P., Barret, B., Basdevant, C., Clenet, A., Derrien, S., Doerenbecher, El Amraoui, L., Fontaine, A., Hache, E., Lambert C., Jaumouillé, E., Meyerfeld, Y., Roblou, L., and Tocquer, F.: Adapted ECC ozone sonde for long-duration flights aboard boundary-layer pressurized balloons, *Atmos. Meas. Tech.*, in prep. for this special issue, 2015.
- Gimeno, L., Drumond, A., Nieto, R., Trigo, R. M., and Stohl, A.: On the origin of continental precipitation, *Geophys. Res. Lett.*, 37, L13804, doi:10.1029/2010GL043712, 2010.
- Giorgi, F., and Lionello, P.: Climate change projections for the Mediterranean region, *Global Planet. Change*, 63, 90-104, doi:10.1016/j.gloplacha.2007.09.005, 2008.
- Giorgi, F., Coppola, E., Solmon, F., Mariotti, L., Sylla, M. B., Bi, X., Elguindi, N., Diro, G.T., Nair, V., Giuliani, G., Turuncoglu, U. U., Cozzini, S., Guttler, I., O'Brien, T. A., Tawfik, A. B., Shalaby, A., Zakey, A. S., Steiner, A. L., Stordal, F., Sloan, L. C., and Brankovic, C.: RegCM4: Model description and preliminary tests over multiple CORDEX domains, *Clim. Res.*, 52, 7-29, doi: 10.3354/cr01018, 2012.
- Gobbi, G.P., Barnaba, F., Giorgi, R., and Santacasa, A.: Altitude-resolved properties of a Saharan dust event over the Mediterranean, *Atmos. Environ.*, 34, 5119-5127, 2000.
- Gross, D. S., Atlas, R., Rzeszutarski, J., Turetsky, E., Christensen, J., Benzaid, S., Olson, J., Smith, T., Steinberg, L. and Sulman, J.: Environmental chemistry through intelligent atmospheric data analysis, *Environ. Model. Software*, 25, 760-769, doi: 10.1016/j.envsoft.2009.12.001, 2010.
- Guenther, A., Karl, T., Harley, P., Wiedinmyer, C., Palmer, P. I., and Geron, C.: Estimates of global terrestrial isoprene emissions using MEGAN (Model of Emissions of Gases and Aerosols from Nature), *Atmos. Chem. Phys.*, 6, 3181-3210, doi:10.5194/acp-6-3181-2006, 2006.
- Guerrero-Rascado, J. L., Olmo, F. J., Avilés-Rodríguez, I., Navas-Guzmán, F., Pérez-Ramírez, D., Lyamani, H., Arboledas, L.A.: Extreme saharan dust event over the southern iberian peninsula in september 2007: Active and passive remote sensing from surface and satellite, *Atmos. Chem. and Phys.*, 9 (21), 8453-8469, 2009.
- Hamonou, E., Chazette, P., Balis, D., Dulac, F., Schneider, X., Galani, E., Ancellet, G., and Papayannis, A.: Characterization of the vertical structure of Saharan dust export to the Mediterranean basin, *J. Geophys. Res.*, 104, 22257-22270, 1999.
- Hashimoto, M., Nakajima, T., Dubovik, O., Campanelli, M., Che, H., Khatri, P., Takamura, T., and Pandithurai, G.: Development of a new data-processing method for SKYNET sky radiometer observations, *Atmos. Meas. Tech.*, 5, 2723-2737, doi:10.5194/amt-5-2723-2012, 2012.
- Harris, I, Jones, P., Osborn, T., Lister, D.: Updated high-resolution grids of monthly climatic observations—the cru ts3.10 dataset. *Int J Climatol* 34:623-642. doi:10.1002/joc.3711, 2013.
- Hatzianastassiou, N., Gkikas, A., Mihalopoulos, N., Torres, O., and Katsoulis, B. D.: Natural versus anthropogenic aerosols in the eastern Mediterranean basin derived from multiyear TOMS and MODIS satellite data, *J. Geophys. Res.*, 114, D24202, doi:10.1029/2009JD011982, 2009.
- Healy, R. M., Hellebust, S., Kourtchev, I., Allanic, A., O'Connor, I. P., Bell, J. M., Sodeau, J. R., Wenger, J. C., Healy, D. A., Sodeau, J. R., and Wenger, J. C.: Source apportionment of PM<sub>2.5</sub> in Cork Harbour, Ireland using a combination of single particle mass spectrometry and quantitative semi-continuous measurements, *Atmos. Chem. Phys.*, 10, 9593-9613. doi:10.5194/acpd-10-1035-2010, 2010.
- Holben B.N., Eck, T.F., Slutsker, I., Tanré, D., Buis, J.P., Setzer, A., Vermote, E., Reagan, J.A., Kaufman, Y.J., Nakajima, T., Lavenu, F., Jankowiak, I., and Smirnov, A.: AERONET - A federated instrument network and data archive for aerosol characterization, *Rem. Sens. Environ.*, 66, 1-16, doi:10.1016/S0034-4257(98)00031-5, 1998.
- Horvath, H., Alados Arboledas, L., Olmo, F.J., Jovanovic, O., Gangl, M., Sanchez, C., Sauerzopf, H., and Seidl, S.: Optical characteristics of the aerosol in Spain and Austria and its effect on radiative forcing, *J. Geophys. Res.*, 107, 4386, doi:10.1029/2001JD001472, 2002.
- Johnson, G., Ristovski, Z., and Morawska, L.: Application of the VH-TDMA technique to coastal ambient aerosols, *Geophys. Res. Lett.*, 31, L16105, doi:10.1029/2004GL020126, 2004.

- Kahn, R. A., Gaitley, B. J., Garay, M. J., Diner, D. J., Eck, T. F., Smirnov, A., and Holben, B. N.: Multiangle Imaging SpectroRadiometer global aerosol product assessment by comparison with the Aerosol Robotic Network, *J. Geophys. Res.*, 115, D23209, doi:10.1029/2010JD014601, 2010.
- Kalnay et al.: The NCEP/NCAR 40-year reanalysis project, *Bull. Amer. Meteor. Soc.*, 77, 437-470, 1996.
- Karol, Y., Tanré, D., Goloub, P., Ververde, C., Balois, J. Y., Blarel, L., Podvin, T., Mortier, A., and Chaikovsky, A.: Airborne sun photometer PLASMA: concept, measurements, comparison of aerosol extinction vertical profile with lidar, *Atmos. Meas. Tech.*, 6, 2383-2389, 2013.
- Kaskaoutis, D. G., Kharol, S. K., Sifakis, N., Nastos, P. T., Sharma, A. R., Badarinath, K. V. S., and Kambezidis, H. D.: Satellite monitoring of the biomass-burning aerosols during the wildfires of August 2007 in Greece: Climate implications, *Atmos. Environ.*, 45, 716–726, doi:10.1016/j.atmosenv.2010.09.043, 2011.
- Kok, J. F.: A scaling theory for the size distribution of emitted dust aerosols suggests climate models underestimate the size of the global dust cycle, *P. Natl. Acad. Sci. USA*, 108, 1016–1021, doi:10.1073/pnas.1014798108, 2011.
- Kubilay, N., Cokacar, T., and Oguz, T.: Optical properties of mineral dust outbreaks over the northeastern Mediterranean, *J. Geophys. Res.*, 108, 4666, doi:10.1029/2003JD003798, 2003.
- Kumar, D., Rocadenbosch, F., Sicard, M., Comeron, A., Muñoz, C., Lange, D., Tomás, S., and Gregorio, E.: Six-channel polychromator design and implementation for the UPC elastic/Raman LIDAR, in: *SPIE Remote Sens., Int. Soc. Opt. Photon., Prague, Czech Republic, 81820W–81820W*, 2011.
- Lelieveld, J., Berresheim, H., Borrmann, S., Crutzen, P. J., Dentener, F. J., Fischer, H., Feichter, J., Flatau, P. J., Heland, J., Holzinger, R., Korrmann, R., Lawrence, M. G., Levin, Z., Markowicz, K. M., Mihalopoulos, N., Minikin, A., Ramanathan, V., de Reus, M., Roelofs, G. J., Scheeren, H. A., Sciare, J., Schlager, H., Schultz, M., Siegmund, P., Steil, B., Stephanou, E. G., Stier, P., Traub, M., Warneke, C., Williams, J., Ziereis, H.: Global air pollution crossroads over the Mediterranean, *Science*, 298, 794–799, doi:10.1126/science.1075457, 2002.
- Léon, J.F., Augustin, P., Mallet, M., Bourrienne, T., Pont, V., Dulac, F., Fourmentin, M., and Lambert, D.: Aerosol vertical distribution, optical properties, and transport over Corsica (western Mediterranean), *Atmos. Chem. Phys. Discuss.*, 15, 9507-9540, 2015.
- Lionello, P., Malanotte-Rizzoli, P., Boscolo, R., Alpert, P., Artale, V., Li, L., Luterbacher, J., May, W., Trigo, R., Tsimplis, M., Ulbrich, U., and Xoplaki, E.: The Mediterranean climate: An overview of the main characteristics and issues, in *The Mediterranean Climate Variability*, P. Lionello, P. Malanotte-Rizzoli and R. Boscolo Eds., *Developments in Earth and Environmental Sciences*, 4, Elsevier, 1-26, 2006.
- Liu, Y., Kahn, R. A., Chaloulakou, A., and Koutrakis, P.: Analysis of the impact of the forest fires in August 2007 on air quality of Athens using multi-sensor aerosol remote sensing data, meteorology and surface observations, *Atmospheric Environment*, 43, 3310–3318, 2009.
- Lyamani, H., Valenzuela, A., Perez-Ramirez, D., Toledano, C., Granados-Muñoz, M.J., Olmo, F.J., Alados-Arboledas, L.: Aerosol properties over the western Mediterranean basin: Temporal and spatial variability, *Atmos. Chem. and Phys.*, 15 (5), 2473-2486, 2015.
- Mailler, S., Menut, L., Di Sarra, A.G., Becagli, S., Di Iorio, T., Formenti, P., Bessagnet, B., Briant, R., Gómez-Amo, J.L., Mallet, M., Rea, G., Siour, G., Sferlazzo, D.M., Traversi, R., Udisti, R., and Turquety, S.: On the radiative impact of aerosols on photolysis rates: comparison of simulations and observations in the Lampedusa island during the ChArMEx/ADRIMED campaign, *Atmos. Chem. Phys. Discuss.*, 15, 7585-7643, doi:10.5194/acpd-15-7585-2015, 2015.
- Mallet, M., Roger, J.C., Despiau, S., Dubovik, O., and Putaud, J.P.: Microphysical and optical properties of aerosol particles in urban zone during ESCOMPTE, *Atmos. Res.*, 69, 73-97, doi:10.1016/j.atmosres.2003.07.001, 2003.
- Mallet, M., Roger, J.C., Despiau, S., Putaud, J.P., and Dubovik, O.: A study of the mixing state of black carbon in urban zone, *J. Geophys. Res.*, 109, D04202, doi:10.1029/2003JD003940, 2004.
- Mallet, M., Van Dingenen, R., Roger, J. C., Despiau, S., and Cachier, H.: In situ airborne measurements of aerosol optical properties during photochemical pollution events. *J. Geophys. Res.*, 110, D03205, doi:10.1029/2004JD005139, 2005.
- Mallet, M., Pont, V., Lioussé, C., Roger, J.C., and Dubuisson, P.: Simulation of aerosol radiative properties with the ORISAM-RAD model during a pollution event (ESCOMPTE 2001), *Atmos. Environ.*, 40, 7696–7705, doi:10.1016/j.atmosenv.2006.08.031, 2006.
- Mallet, M., Gomes, L., Solmon, F., Sellegri, K., Pont, V., Roger, J.C., Missamou, T., and Piazzola, J.: Calculations of key optical properties over the main anthropogenic aerosols over the Western French coastal Mediterranean Sea, *Atmos. Res.*, Vol. 101, doi:10.1016/j.atmosres.2011.03.008, 396-411, 2011.
- Mallet, M., Dubovik, O., Nabat, P., Dulac, F., Kahn, R., Sciare, J., Paronis, D., and Léon, J.F.: Absorption

- properties of Mediterranean aerosols obtained from multi-year ground-based remote sensing observations, *Atmos. Chem. Phys.*, 13, 9195-9210, 2013.
- Markowicz, K. M., Flatau, P. J., Ramana, M. V., Crutzen, P. J., and Ramanathan, V.: Absorbing Mediterranean aerosols lead to a large reduction in the solar radiation at the surface, *Geophys. Res. Lett.*, 29, 1968, doi:10.1029/2002GL015767, 2002.
- Mariotti, A., Zeng, N., Yoon, J., Artale, V., Navarra, A., Alpert, P., and Li, L.Z.X.: Mediterranean water cycle changes: transition to drier 21st century conditions in observations and CMIP3 simulations, *Environ. Res. Lett.*, 3, 044001, doi:10.1088/1748-9326/3/4/044001, 2008.
- Mariotti A., Pan, Y., Zeng, N., and Alessandri, A.: Long-term climate change in the Mediterranean region in the midst of decadal variability, *Clim. Dyn.*, 44, 1437-1456, doi:10.1007/s00382-015-2487-3, 2015.
- Martcorena, B. and Bergametti, G.: Modeling the atmospheric dust cycle 1. Design of a soil-derived dust production scheme, *J. Geophys. Res.*, 100, 16415–16430, 1995.
- McConnell, C. L., Formenti, P., Highwood, E. J., and Harrison, M. A. J.: Using aircraft measurements to determine the refractive index of Saharan dust during the DODO Experiments, *Atmos. Chem. Phys.*, 10, 3081–3098, doi:10.5194/acp-10-3081-2010, 2010.
- Meloni D., Di Sarra, A., DeLuisi, J., Di Iorio, T., Fiocco, G., Junkermann, W., and Pace, G.: Tropospheric aerosols in the Mediterranean: 2. Radiative effects through model simulations and measurements, *J. Geophys. Res.*, 108, 4317, doi:10.1029/2002JD002807, 2003.
- Meloni, D., Di Sarra, A. Di Iorio, T., and Fiocco, G.: Direct radiative forcing of Saharan dust in the Mediterranean from measurements at Lampedusa Island and MISR space-borne observations, *J. Geophys. Res.*, 109, D08206, doi:10.1029/2003JD003960, 2004.
- Meloni, D., Di Sarra, A., Pace, G., and Monteleone, F.: Aerosol optical properties at Lampedusa (Central Mediterranean). 2. Determination of single scattering albedo at two wavelengths for different aerosol types, *Atmos. Chem. Phys.*, 6, 715-727, 2006.
- Meloni, D., Di Sarra, A., Monteleone, F., Pace, G., Piacentini, S., and Sferlazzo, D.M.: Seasonal transport patterns of intense dust events at the Mediterranean island of Lampedusa, *Atmos. Res.*, 88, 134-148, doi:10.1016/j.atmosres.2007.10.007, 2008.
- Meloni, D., Junkermann, W., di Sarra, A., Cacciani, M., De Silvestri, L., Di Iorio, T., Estellés, V., Gómez-Amo, J.L., Pace, G., and Sferlazzo, D.M.: Altitude-resolved shortwave and longwave radiative effects of desert dust in the Mediterranean during the GAMARF campaign: indications of a net daily cooling in the dust layer, *J. Geophys. Res. Atmos.*, 120, doi:10.1002/2014JD022312, 2015.
- Meloni, M., di Sarra, A., Brogniez, G., Denjean, C., De Silvestri, L., Di Iorio, T., Formenti, P., Gomez-Amo, J.-L., Gröbner, J., Kouremeti, N., Mallet, M. and Pace, G.: Simulating vertically resolved SW and LW irradiances and infrared brightness temperatures measured at Lampedusa during the Charmex/ADRIMED campaign, in prep. for this special issue, 2015.
- Menut, L., Bessagnet, B., Khvorostyanov, D., Beekmann, M., Blond, N., Colette, A., Coll, I., Curci, G., Foret, G., Hodzic, A., Mailler, S., Meleux, F., Monge, J.-L., Pison, I., Siour, G., Turquety, S., Valari, M., Vautard, R., and Vivanco, M. G.: CHIMERE 2013: a model for regional atmospheric composition modelling, *Geosci. Model Dev.*, 6, 981-1028, doi: 10.5194/gmd-6-981-2013, 2013.
- Menut, L., Mailler, S., Siour, G., Bessagnet, B., Turquety, S., Rea, G., Briant, R., Mallet, M., Sciare, J., and Formenti, P.: Ozone and aerosols tropospheric concentrations variability analyzed using the ADRIMED measurements and the WRF-CHIMERE models, *Atmos. Chem. Phys. Discuss.*, 15, 3063–3125, doi: 10.5194/acpd-15-3063-20, 2015.
- Millán, M.M., Salvador, R., Mantilla, E., and Kallos, G.: Photooxidant dynamics in the Mediterranean basin in summer: Results from European research projects, *J. Geophys. Res.*, 102, 8811-8823, doi:10.1029/96JD03610, 1997.
- Moosmüller, H., Chakrabarty, R. K., and Arnott, W. P.: Aerosol light absorption and its measurement: A review, *Journal of Quantitative Spectroscopy & radiative transfer*, 100, 844-878, 2009.
- Mulcahy, J. P., O'Dowd, C. D., Jennings, S. G., and Ceburnis, D.: Significant enhancement of aerosol optical depth in marine air under high wind conditions, *Geophys. Res. Letters*, Vol. 35, L16810, doi:10.1029/2008GL034303, 2008.
- Nabat, P., Solmon, F., Mallet, M., Kok, J. F., and Somot, S.: Dust emission size distribution impact on aerosol budget and radiative forcing over the Mediterranean region: a regional climate model approach, *Atmos. Chem. Phys.*, 12, 10545-10567, doi:10.5194/acp-12-10545-2012, 2012.
- Nabat, P., Somot, S., Mallet, M., Chiapello, I., Morcrette, J. J., Solmon, F., Szopa, S., Dulac, F., Collins, W., Ghan, S., Horowitz, L. W., Lamarque, J. F., Lee, Y. H., Naik, V., Nagashima, T., Shindell, D., and Skeie, R.: A 4-D climatology (1979-2009) of the monthly tropospheric aerosol optical depth distribution over the

- Mediterranean region from a comparative evaluation and blending of remote sensing and model products, *Atmos. Meas. Tech.*, 6, 1287-1314, doi:10.5194/amt-6-1287-2013, 2013.
- Nabat, P., Somot, S., Mallet, M., Sanchez-Lorenzo, A., and Wild, M.: Contribution of anthropogenic sulfate aerosols to the changing Euro-Mediterranean climate since 1980, *Geophys. Res. Lett.*, 41, 5605-5611, doi:10.1002/2014GL060798, 2014.
- Nabat, P., Somot, S., Mallet, M., Sevault, F., Chiacchio, M., and Wild, M.: Direct and semi-direct aerosol radiative effect on the Mediterranean climate variability using a coupled regional climate system model, *Clim. Dyn.*, doi:10.1007/s00382-014-2205-6, 2015a.
- Nabat, P., Somot, S., Mallet, M., Michou, M., Sevault, F., Driouech, F., Meloni, D., Di Sarra, A., Di Biagio, C., Formenti, P., Sicard, M., Léon, J.-F., and Bouin, M.-N.: Dust aerosol radiative effects during summer 2012 simulated with a coupled regional aerosol-atmosphere-ocean model over the Mediterranean, *Atmos. Chem. Phys.*, 15, 3303-3326, doi:10.5194/acp-15-3303-2015, 2015b.
- Nicolas, J., Mallet, M., Roberts, G., Denjean, C., Formenti, P., Fresney, E., Sellegri, K., Borgniez, G., Bourriane, T., Pigué, B., Torres, B., Dubuisson, P., and Dulac, F.: Aerosol direct radiative forcing at a regional scale over the western Mediterranean in summer within the ADRIMED project: airborne observations compared to GAME simulations, *Atmos. Chem. Phys. Discuss.*, in prep. for this special issue, 2015.
- Noilhan, J. and Mahfouf, J.-F.: The ISBA land surface parameterisation scheme, *Global Planet. Change*, 13, 145-159, doi:10.1016/0921-8181(95)00043-7, 1996.
- Ortiz-Amezcuca, P., Guerrero-Rascado, J. L., Granados-Muñoz, M. J., Bravo-Aranda, J. A., Alados-Arboledas, L.: Characterization of atmospheric aerosols for a long range transport of biomass burning particles from canadian forest fires over the southern iberian peninsula in July 2013, *Optica Pura y Aplicada*, 47, 43-49, 2014.
- Otto, S., Bierwirth, E., Weinzierl, B., Kandler, K., Esselborn, M., Tesche, M., Schladitz, A., Wendisch, M., and Trautmann, T.: Solar radiative effects of a Saharan dust plume observed during SAMUM assuming spheroidal model particles, *Tellus B*, 61, 270-296, doi:10.1111/j.1600-0889.2008.00389.x, 2009.
- Pace, G., Meloni, D., and di Sarra, A.: Forest fire aerosol over the Mediterranean basin during summer 2003, *J. Geophys. Res.*, 110, D21202, doi:10.1029/2005JD005986, 2005.
- Pace, G., Di Sarra, A., Meloni, D., Piacentino, S., and Chamard, P.: Aerosol optical properties at Lampedusa (Central Mediterranean). 1. Influence of transport and identification of different aerosol types, *Atmos. Chem. Phys.*, 6, 697-713, 2006.
- Papadimas, C. D., Hatzianastassiou, N., Matsoukas, C., Kanakidou, M., Mihalopoulos, N., and Vardavas, I.: The direct effect of aerosols on solar radiation over the broader Mediterranean basin, *Atmos. Chem. Phys.*, 12, 7165-7185, doi:10.5194/acp-12-7165-2012, 2012.
- Papayannis, A., Balis, D., Amiridis, V., Chourdakis, G., Tsaknakis, G., Zerefos, C., Castanho, A.D.A., Nickovic, S., Kazadzis, S., and Grabowski, J.: Measurements of Saharan dust aerosols over the Eastern Mediterranean using elastic backscatter-Raman lidar, spectrophotometric and satellite observations in the frame of the EARLINET project, *Atmos. Chem. Phys.*, 5, 2065-2079, 2005.
- Papayannis, A., Amiridis, V., Mona, L., Tsaknakis, G., Balis, D., Bösenberg, J., Chaikovski, A., De Tomasi, F., Grigorov, I., Mattis, I., Mitev, V., Müller, D., Nickovic, S., Pérez, C., Pietruczuk, A., Pisani, G., Ravetta, F., Rizi, V., Sicard, M., Trickl, T., Wiegner, M., Gerding, M., Mamouri, R. E., D'Amico, G., and Pappalardo, G.: Systematic lidar observations of Saharan dust over Europe in the frame of EARLINET (2000-2002), *J. Geophys. Res.*, 113, D10204, doi:10.1029/2007JD009028, 2008.
- Pappalardo, G., Amodeo, A., Mona, L., Pandolfi, M., Pergola, N., and Cuomo, V.: Raman lidar observations of aerosol emitted during the 2002 Etna eruption, *Geophys. Res. Lett.*, 31, L05120, doi:10.1029/2003GL019073, 2004.
- Pappalardo, G., Amodeo, A., Apituley, A., Comeron, A., Freudenthaler, V., Linné, H., Ansmann, A., Bösenberg, J., D'Amico, G., Mattis, I., Mona, L., Wandinger, U., Amiridis, V., Alados-Arboledas, L., Nicolae, D., and Wiegner, M.: EARLINET: towards an advanced sustainable European aerosol lidar network, *Atmos. Meas. Tech.*, 7, 2389-2409, doi:10.5194/amt-7-2389-2014, 2014.
- Péré, J.C., Mallet, M., Pont, V., and Bessagnet, B.: Impact of aerosol direct radiative forcing on the radiative budget, surface heat fluxes, and atmospheric dynamics during the heat wave of summer 2013 over western Europe: A modelling study, *J. Geophys. Res.*, 116, D23119, doi:10.1029/2011JD016240, 2011.
- Pérez, C., Sicard, M., Jorba, O., Comerón, A., and Baldasano, J.M.: Summertime re-circulations of air pollutants over the north-eastern Iberian coast observed from systematic EARLINET lidar measurements in Barcelona, *Atmos. Environ.*, 38, 3983-4000, 2004.
- Pérez, C., Nickovic, S., Baldasano, J.M., Sicard, M., Rocadenbosch, F., Cachorro, V.E.: A long Saharan dust event

- over the western Mediterranean: Lidar, sun photometer observations, and regional dust modeling. *J. Geophys. Res.*, 111, D15214, doi:10.1029/2005JD006579, 2006.
- Petzold, A., Onasch, T., Kebedian, P., and Freedman, A.: Intercomparison of a Cavity Attenuated Phase Shift-based extinction monitor (CAPS PMex) with an integrating nephelometer Climate and a filter-based absorption monitor, *Atmos. Meas. Tech.*, 6, 1141–1151, 2013.
- Piazzola, J., Tedeschi, G., and Demoisson, A.: A model for a transport of sea-spray Aerosols in the coastal zone, *Boundary Layer Meteorol.*, 155:329-350, 2015.
- Ramanathan, V., et al.: Indian Ocean experiment: An integrated analysis of the climate forcing and effects of the great Indo-Asian haze, *J. Geophys. Res.*, 106, 28371–28398, doi:10.1029/2001JD900133, 2001.
- Ravetta, F., Ancellet, G., Colette, A., and Schlager, H.: Long-range transport and tropospheric ozone variability in the western Mediterranean region during the Intercontinental Transport of Ozone and Precursors (ITOP-2004) campaign, *J. of Geophys. Res.*, 112, doi:10.1029/2006JD007724, 2007.
- Rea, G., Turquety, S., Menut, L., Briant, R., Mailler, S., and Siour, G.: Source contributions to 2012 summertime aerosols in the Euro-Mediterranean region, *Atmos. Chem. Phys. Discuss.*, 15, 8191–824, doi:10.5194/acpd-15-8191-20, 2015.
- Renard, J.-B., et al.: LOAC: a small aerosol optical counter/sizer for ground-based and balloon measurements of the size distribution and nature of atmospheric particles – Part 1: Principle of measurements and instrument evaluation, *Atmos. Meas. Tech. Discuss.*, 8, 1203-1259, doi:10.5194/amtd-8-1203-2015, 2015a.
- Renard, J.-B., et al.: LOAC: a small aerosol optical counter/sizer for ground-based and balloon measurements of the size distribution and nature of atmospheric particles – Part 2: First results from balloon and unmanned aerial vehicle flights, *Atmos. Meas. Tech. Discuss.*, 8, 1261-1299, doi:10.5194/amtd-8-1261-2015, 2015b.
- Roger, J.C., Mallet, M., Dubuisson, P., Cachier, H., Vermote, E., Dubovik, O., and Despiiau, S.: A synergetic approach for estimating the local direct aerosol forcing: application to an urban zone during the Experience sur Site pour Contraindre les Modèles de Pollution et de Transport d’Emission (ESCOMPTE) experiment, *J. Geophys. Res.*, 111, D13208, doi:10.1029/2005JD006361, 2006.
- Royer, P., Raut, J.-C., Ajello, G., Berthier, S., and Chazette, P.: Synergy between CALIOP and MODIS instruments for aerosol monitoring: application to the Po Valley, *Atmos. Meas. Tech.*, 3, 893-907, doi:10.5194/amt-3-893-2010, 2010.
- Ryder, C. L., Highwood, E. J., Rosenberg, P. D., Trembath, J., Brooke, J. K., Bart, M., Dean, A., Crosier, J., Dorsey, J., Brindley, H., Banks, J., Marsham, J. H., McQuaid, J. B., Sodemann, H., and Washington, R.: Optical properties of Saharan dust aerosol and contribution from the coarse mode as measured during the Fennec 2011 aircraft campaign, *Atmos. Chem. Phys.*, 13, 303-325, doi:10.5194/acp-13-303-2013, 2013.
- Saha, A., Mallet, M., Roger, J.C., Dubuisson, P., Piazzola, J., and Despiiau, S.: One year measurements of aerosol optical properties over an urban coastal site: Effect on local direct radiative forcing, *Atmos. Res.*, 90, 195-202, doi:10.1016/j.atmosres.2008.02.003, 2008.
- Sanchez-Gomez, E., Somot, S., and Mariotti, A.: Future changes in the Mediterranean water budget projected by an ensemble of regional climate models, *Geophys. Res. Lett.*, 36, L21401, doi:10.1029/2009GL040120, 2009.
- Salameh, T., Drobinski, P., Menut, L., Bessagnet, B., Flamant, C., Hodzic, A., and Vautard, R.: Aerosol distribution over the western Mediterranean basin during a Tramontane/Mistral event, *Ann. Geophys.*, 25, 2271-2291, 2007.
- Santese, M., Perrone, M.R., Zakey, A.S., De Tomasi, F., and Giorgi, F.: Modeling of Saharan dust outbreaks over the Mediterranean by RegCM3: case studies, *Atmos. Chem. Phys.*, 10, 133–156, doi:10.5194/acp-10-133-2010, 2010.
- Sassen, K.: Lidar backscatter depolarization technique for cloud and aerosol research, in *Light Scattering by Nonspherical Particles: Theory, Measurements, and Applications*, edited by Mishchenko, M., Hovenier, J.W., and Travis, L.D., Academic Press, 393-417, 1999.
- Schepanski, K., Tegen, I., Laurent, B., Heinold, B., and Macke, A.: A new Saharan dust source activation frequency map derived from MSG-SEVIRI IR-channels, *Geophys. Res. Lett.*, 34, 18803, doi:10.1029/2007GL030168, 2007.
- Sciare, J., Cachier, H., Oikonomou, K., Ausset, P., Sarda-Estève, R., and Mihalopoulos, N.: Characterization of carbonaceous aerosols during the MINOS campaign in Crete, July–August 2001: a multi-analytical approach, *Atmos. Chem. Phys.*, 3, 1743-1757, doi:10.5194/acp-3-1743-2003, 2003.
- Sciare, J., Oikonomou, K., Favez, O., Liakakou, E., Markaki, Z., Cachier, H., and Mihalopoulos, N.: Long-term measurements of carbonaceous aerosols in the Eastern Mediterranean: evidence of long-range transport of biomass burning, *Atmos. Chem. Phys.*, 8, 5551–5563, doi:10.5194/acp-8-5551-2008, 2008.
- Schicker, I., Radanovics, S., and Seibert, P.: Origin and transport of Mediterranean moisture and air *Atmos.*



- Chem. Phys., 10, 5089–5105, doi:10.5194/acp-10-5089-2010, 2010.
- Schroeder, W., Csiszar, I., Giglio, L., and Schmidt, C. C.: On the use of fire radiative power, area, and temperature estimates to characterize biomass burning via moderate to coarse spatial resolution remote sensing data in the Brazilian Amazon, *J. Geophys. Res.*, 115, D21121, doi:10.1029/2009JD013769, 2010.
- Sellegrì, K., Rose, C., Culot, A., Sauvage, S., Roberts, G., Marchand, N., Pey, J., Sciare, J., Bourriane, T., Mallet, M., and Dulac, F.: Spatial extent, occurrence and precursors of nucleation events over the western Mediterranean basin, in prep. for publication in this special issue, 2015.
- Sellitto, P., di Sarra, A., Corradini, S., Boichu, M., Herbin, H., Dubuisson, P., Sèze, G., Meloni, D., Monteleone, F., Merucci, L., Rusaleem, J., Salerno, G., Briole, P., and Legras, B.: Synergistic use of Lagrangian dispersion modelling, satellite- and ground-based remote sensing measurements for the investigation of volcanic plumes: the Mount Etna eruption of 25-27 October 2013, *Atmos. Chem. Phys. Disc.*, submitted to this special issue, 2015.
- Sicard, M., Rocadenbosch, F., Reba, M. N. M., Comerón, A., Tomás, S., García-Vázquez, D., Batet, O., Barrios, R., Kumar, D., and Baldasano, J. M.: Seasonal variability of aerosol optical properties observed by means of a Raman lidar at an EARLINET site over Northeastern Spain, *Atmos. Chem. Phys.*, 11, doi:10.5194/acp-11-175-2011, 2011.
- Sicard, M., Bertolín, S., Mallet, M., Dubuisson, P., and Comerón, A.: Estimation of mineral dust long-wave radiative forcing: sensitivity study to particle properties and application to real cases in the region of Barcelona, *Atmos. Chem. Phys.*, 14, 9213–9231, doi:10.5194/acp-14-9213-2014, 2014a.
- Sicard, M., Bertolín, S., Muñoz, C., Rodríguez, A., Rocadenbosch, F., and Comerón, A.: Separation of aerosol fine- and coarse-mode radiative properties: Effect on the mineral dust longwave, direct radiative forcing, *Geophys. Res. Lett.*, 41, doi:10.1002/2014GL060946, 2014b.
- Sicard, M., Barragan, R., Muñoz-Porcar, C., Comerón, A., Mallet, M., Dulac, F., Pelon, J., Alados-Arboledas, L., Amodeo, A., Boselli, A., Bravo-Aranda, J. A., D'Amico, G., Granados-Muñoz, M. J., Leto, Guerrero-Rascado, J. L., Madonna, F., Mona, L., Pappalardo, G., Perrone, M. R., Burlizzi, P., Rocadenbosch, F., Rodríguez-Gómez, A., Scollo, Spinelli, N., Titos, G., Wang, X., and Zanmar Sanchez, R.: Contribution of EARLINET/ACTRIS to the summer 2013 Special Observing Period of the ChArMEx project, *Óptica Pura y Aplicada*, submitted, 2015a.
- Sicard, M., Barragan, Dulac, F., Alados-Arboledas, L., and Mallet, M.: Aerosol Aerosol optical, microphysical and radiative properties at three regional background insular sites in the western Mediterranean Basin, *Atmos. Chem. Phys. Discuss.*, submitted in this special issue, 2015b.
- Solmon, F., Giorgi, F., and Liousse, C.: Aerosol modelling for regional climate studies: application to anthropogenic particles and evaluation over a European/African domain, *Tellus*, 58B, 51–72, doi:10.1111/j.1600-0889.2005.00155.x, 2006.
- Solmon, F., Mallet, M., Elguindi, N., Giorgi, F., Zakey, A., and Konaré, A.: Dust aerosol impact on regional precipitation over western Africa: mechanisms and sensitivity to absorption properties. *Geophys Res Lett* 35, L24705, doi:10.1029/2008GL035900, 2008.
- Spada, M., Jorba, O., Pérez Garcia-Pando, C., Janjic, Z., and Baldasano, J. M.: Modeling and evaluation of the global sea-salt aerosol distribution: sensitivity to emission schemes and resolution effects at coastal/orographic sites, *Atmos. Chem. Phys.*, 13, 11735-11755, doi:10.5194/acp-13-11735-2013, 2013.
- Tafuro, A.M., Barnaba, F., De Tomasi, F., Perrone, M. R., and Gobbi, G. P.: Saharan dust particle properties over the central Mediterranean, *Atmos. Res.*, 81, 67-93, 2006.
- Tafuro, A. M., Kinne, S., De Tomasi, F., and Perrone, M. R.: Annual cycle of aerosol direct radiative effect over southeast Italy and sensitivity studies, *J. Geophys. Res.*, 112, D20202, doi:10.1029/2006JD008265, 2007.
- Tanré, D., Kaufman, Y. J., Herman, M., and Mattoo, S.: Remote sensing of aerosol properties over oceans using the MODIS/EOS spectral radiances, *J. Geophys. Res.*, 102, 16971–16988, 1997.
- Tanré, D., Bréon, F. M., Deuzé, J. L., Dubovik, O., Ducos, F., Francois, P., Goloub, P., Herman, M., Lifermann, A., and Waquet, F.: Remote sensing of aerosols by using polarized, directional and spectral measurements within the A-Train: the PARASOL mission, *Atmos. Meas. Tech.*, 4, 1383–1395, doi:10.5194/amt-4-1383-2011, 2011.
- Tegen, I., Harrison, S. P., Kohfeld, K. E., and Prentice, I. C.: Impact of vegetation and preferential source areas on global dust aerosol: Results from a model study, *J. Geophys. Res.*, 107, 4576, doi:10.1029/2001JD000963, 2002.
- Thieuleux, F., Moulin, C., Bréon, F. M., Maignan, F., Poitou, J., and Tanré, D.: Remote sensing of aerosols over the oceans using MSG/SEVIRI imagery, *Ann. Geophys.*, 23, 3561–3568, doi:10.5194/angeo-23-3561-2005, 2005.
- Torres, B., Dubovik, O., Fuertes, D., Lapyonok, T., Toledano, C., Schuster, G.L., Goloub, P., Blarel, L., Barreto, A., Mallet, M., and Tanré, D.: Advanced characterization of aerosol properties from measurements of spectral optical thickness of the atmosphere, in prep. for this special issue, 2015.
- Turco, M., Llasat, M.C., Tudela, A., Castro, X., and Provenzale, A.: Decreasing fires in a Mediterranean region

- (1970-2010, NE Spain), *Nat. Hazards Earth Syst. Sci.*, 13, 649-652, doi:10.5194/nhess-13-649-2013, 2013.
- Turquety, S., Menut, L., Bessagnet, B., Anav, A., Viovy, N., Maignan, F., and Wooster, M.: APIFLAME v1.0: high-resolution fire emission model and application to the Euro-Mediterranean region, *Geosci. Model Dev.*, 7, 587-612, 2014.
- Vaishya, A., Jennings, S. G., and O'Dowd, C.: Wind-driven influences on aerosol light scattering in north-east Atlantic air, *Geophys. Res. Lett.*, 39, L05805, doi:10.1029/2011GL050556, 2012.
- Valenzuela, A., Olmo, F. J., Lyamani, H., Antón, M., Quirantes, A., Alados-Arboledas, L.: Aerosol radiative forcing during African desert dust events (2005-2010) over Southeastern Spain, *Atmos. Chem. and Phys.*, 12, 10331-10351, 2012.
- Vialard, J., et al.: Cirene: Air-sea interactions in the Seychelles-Chagos thermocline ridge region, *Bull. Am. Meteor. Soc.*, 90, 45-61, doi:10.1175/2008BAMS2499.1, 2009.
- Wang, Y., Sartelet, K. N., Bocquet, M., Chazette, P., Sicard, M., D'Amico, G., Léon, J. F., Alados-Arboledas, L., Amodeo, A., Augustin, P., Bach, J., Belegante, L., Binietoglou, V., Bush, X., Comerón, A., Delbarre, H., García-Vízcaino, D., Guerrero-Rascado, J. L., Hervo, M., Iarlori, M., Kokkalis, P., Lange, D., Molero, F., Montoux, N., Muñoz, A., Muñoz, C., Nicolae, D., Papayannis, A., Pappalardo, G., Preissler, J., Rizi, V., Rocadenbosch, F., Sellegri, K., Wagner, F., and Dulac, F.: Assimilation of lidar signals: application to aerosol forecasting in the western Mediterranean basin, *Atmos. Chem. Phys.*, 14, 12031-12053, doi:10.5194/acp-14-12031-2014, 2014.
- Waquet, F., Cornet, C., Deuzé, J.-L., Dubovik, O., Ducos, F., Goloub, P., Herman, M., Lapyonok, T., Labonnote, L.C., Riedi, J., Tanré, D., Thieuleux, F., and Vanbauce, C.: Retrieval of aerosol microphysical and optical properties above liquid clouds from POLDER/PARASOL polarization measurements, *Atmos. Meas. Tech.*, 6, 991-1016, doi:10.5194/amt-6-991, 2013.
- Wolke, R., Schroeder, W., Schroedner, R., Renner, E.: Influence of grid resolution and meteorological forcing on simulated European air quality: A sensitivity study with the modeling system COSMO-MUSCAT. *Atmos. Environ.*, 53, 110-130, 2012.
- Yue, X., Liao, H., Wang, H.J., Li, S.L., and Tang, J.P.: Role of sea surface temperature responses in simulation of the climatic effect of mineral dust aerosol, *Atmos. Chem. Phys.*, 11, 6049-6062, doi:10.5194/acp-11-6049-2011, 2011.
- Zakey, A. S., Solmon, F., and Giorgi, F.: Implementation and testing of a desert dust module in a regional climate model, *Atmos. Chem. Phys.*, 6, 4687-4704, 2006.
- Zakey, A. S., Giorgi, F., and Bi, X.: Modeling of sea salt in a regional climate model: Fluxes and radiative forcing, *J. Geophys. Res.*, 113, D14221, doi:10.1029/2007JD009209, 2008.
- Zanis, P., Ntogras, C., Zakey, A., Pytharoulis, I., and Karacostas, T.: Regional climate feedback of anthropogenic aerosols over Europe using RegCM3, *Clim. Res.*, V52, 267-278, doi:10.3354/cr01070, 2012.
- Zhu, A., Ramanathan, V., Li, F., and Kim, D.: Dust plumes over the Pacific, Indian, and Atlantic oceans: Climatology and radiative impact, *J. Geophys. Res.*, 112, D16208, doi:10.1029/2007JD008427, 2007.